Habilitation Thesis

Mechanics, Fatigue and Fracture of Materials and Structures

Anghel Vasile Cernescu, PhD

Department of Mechanics and Strength of Materials

Politehnica University Timisoara

2020

Table of Content

Abstract

This habilitation thesis represents my research activity since 2010, after receiving the title of Doctor in Engineering Sciences, until now.

This work is a collection of analytical and experimental studies where the Mechanics of Continuum, Fatigue and Fracture Mechanics concepts are applied to solve different problems. Structured in three parts, the work contains carried out researches, proposals for the academic career development, annexes and references.

In the first part are discussed researches conducted on non-metallic materials, components and structures.

The work starts with an exhaustive study on mechanical behaviour, fatigue and fracture of total dentures. The research was conducted within a postdoctoral internship funded by the European Commission, at Politehnica University of Timisoara. During this study, a series of acrylic resins used as dental prosthesis bases were tested. The study is followed by numerical and experimental analyses related to the stress and strains fields in dentures. Reverse Engineering techniques have been also used for three-dimensional modelling of real dentures. The second study is an independent research in which relationships were proposed for bending deflection of sandwich beam loaded with a concentrated force. The novelty of this study consists in taking into account the additional effect given by the concentrated force that is significant for flexible core structures. The work continues with an experimental research on fibre-reinforced composites. This study was conducted within a postdoctoral research program at Vrije University Brussels, Belgium. In this study, the damage parameters from Ladeveze's model were experimentally determined. This model can be successfully used in damage prediction of composite materials. The second part contains research on metallic materials, components and structures, and starts with an analytical study on the mechanical behaviour of a cylindrical cell core structure used in the construction of sandwich panels. The analysed structure is an own proposal, for which relationships of the equivalent elastic constants computation have been developed, using the homogenisation technique of the mechanical properties. The work also includes an experimental study on the fatigue crack propagation in a low alloy steel. The research was conducted within a postdoctoral fellowship at Aalto University, Finland. In this study, the fatigue crack growth rate was determined both in the base material and laser welded. Moreover, the residual stress effect on fatigue crack growth rate was analytically and experimentally analysed. The third study is an individual research that highlighted the *crack tip shielding* effect during the fatigue crack propagation. The work continues with an experimental study in which the first fatigue tests of the

overhead line conductors in Romania were carried out. This analysis consisted in defining a laboratory testing methodology of the electrical conductors, the actual testing and respectively the analysis of the local damage of the component wires of the conductor. The second part ends with an experimental and numerical analysis were a methodology was developed for failure analysis of a coupling of railway wagons failed by fatigue.

The third part contains proposals for career development and has three directions: scientific, professional and academic. Clear proposals and solutions are being discussed in this section.

The work ends with annexes and references and also represents a content that reflects the professional profile of the author.

Rezumat

Prezenta teză de abilitare reprezintă activitatea mea de cercetare începând cu anul 2010, după primirea titlului de doctor inginer în Științe Inginerești, și până în prezent.

Lucrarea reprezintă o colecție de studii analitice și experimentale în care conceptele Mecanicii Continuului, Oboseala și Mecanica Ruperii sunt aplicate pentru rezolvarea diferitor probleme. Structurată pe trei părți, lucrarea conține cercetări efectuate, propuneri de dezvoltare a carierei academice, respectiv anexe și referințe bibliografice.

În prima parte sunt discutate cercetări alese efectuate pe materiale ne-metalice respectiv componente și structuri.

Lucrarea începe cu un studiu exhaustiv cu privire la comportarea mecanică, oboseala și ruperea protezelor dentare totale. Cercetarea a fost derulată în cadrul unui stagiu postdoctoral finanțat de Comisia Europeană, la Universitatea Politehnica Timișoara. Pe parcursul acestui studiu au fost testate o serie de rășini acrilice utilizate ca baze în protetica dentară. Studiul este continuat cu analize numerice validate experimental privind starea de tensiune și deformație din proteze. De asemenea, au fost utilizate tehnici ale Ingineriei Inverse pentru modelarea tridimensională a protezelor reale. Al doilea studiu a reprezentat o cercetare independentă în care au fost propuse relații de calcul a săgeții la încovoiere a unei structuri sandwich solicitată cu o forță concentrată. Noutatea a constat în introducerea în relațiile de calcul a efectului suplimentar dat de forța concentrată, care pentru astfel de structuri cu miez flexibil este semnificativ. Lucrarea continuă cu o cercetare experimentală asupra materialelor compozite armate cu fibre. Studiul a fost derulat în cadrul unui program de cercetare postdoctorală efectuat la Universitatea Vrije din Bruxelles, Belgia. În cadrul acestui studiu au fost determinați experimental parametrii de degradare din modelul Ladeveze. Acest model poate fi utilizat cu succes în predicția degradării materialelor compozite solicitate cvasi-static sau la oboseală.

Partea a doua conține cercetări efectuate pe materiale metalice, componente și respectiv structuri și începe cu un studiu privind comportarea mecanică a unei structuri miez cu celule cilindrice, utilizată în construcția panourilor sandwich. Structura analizată este o propunere proprie, pentru care au fost dezvoltate relații de calcul a constantelor de elasticitate echivalentă, folosind tehnica omogenizării proprietăților mecanice. Lucrarea cuprinde, de asemenea, un studiu experimental cu privire la propagarea fisurilor de oboseală într-un oțel slab aliat. Cercetarea a fost efectuată în cadrul unui program postdoctoral derulat la Universitatea Aalto, Finlanda. În cadrul acestui studiu, s-a determinat viteza de propagare a fisurilor de oboseală atât în material de bază cât și sudat cu laser. De asemenea, efectul

tensiunii reziduale din sudură, asupra vitezei de propagare a fisurii a fost evidențiat analitic și experimental. Al treilea studiu reprezintă o cercetare individuală prin care s-a evidențiat efectul de *blocare a vârfului fisurii* (*crack tip shielding*) în decursul propagării unei fisuri de oboseală. Lucrarea continuă cu un studiu experimental în cadrul căruia au fost efectuate primele încercări de oboseală a conductoarelor liniilor electrice aeriene, din Romania. Această analiză a constat în definitivarea unei metodologii de testare în laborator a conductoarelor electrice, efectuarea propriu-zisă a testelor de oboseală și respectiv analiza mecanismelor de degradare locală a firelor din componența conductorului. Partea a doua se încheie cu o analiză experimentală și numerică în cadrul căreia a fost elaborată o metodologie de expertizare a unei cuple de legatură a vagoanelor de cale ferată ruptă prin oboseală.

Partea a treia prezintă propuneri de continuare a dezvoltării carierei academice și are în vedere trei direcții: științific, profesional și academic. Sunt discutate atât propuneri clare cât și soluții care să ducă la realizarea acestora.

Lucrarea se încheie cu anexe și referințe bibliografice și de asemenea reprezintă un conținut care reflectă profilul profesional al autorului.

1. Research on non-metallic materials

1.1. Research on acrylic dental materials and dentures

1.1.1. Mechanical behaviour of acrylic resins

Dental prostheses are physical bodies made of various materials (polymers, metallic and/or ceramic) through a succession of clinical and technical stages, in order to restore the morpho-functional part of the total or partial edentulous. The total dentures consist mainly of bases, saddles and artificial teeth, fig. 1.1.a. In the case of mandibular dentures, the base is confused with the saddles, because the edged ridges are essentially the only support area, fig. 1.1.b. The shape of the total denture base is specific to the maxilla and mandible.

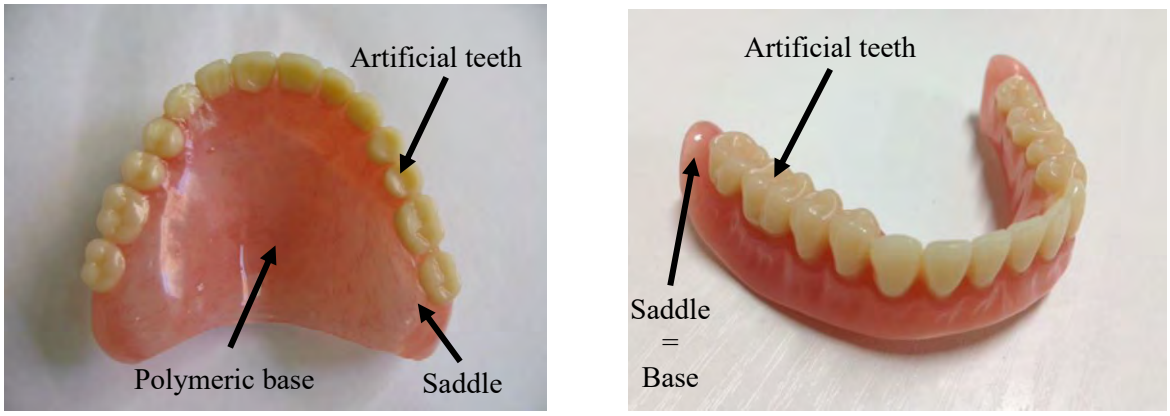

a) b)

Fig. 1.1. Total dentures: a) maxillary denture; b) mandibular denture

Generally, the bases of the total dentures are made of polymeric materials based on polymethyl methacrylate (PMMA), and respectively additional copolymers and pigment, as powder and a liquid consists of methacrylate-based monomers along with a cross-linking agent. Most commonly these materials are known as acrylic resins.

The acrylic resins have constantly diversified, improving their qualities and becoming more biocompatible and resistant. This has resulted in a range of injectable chemical or self-curing resins, heat-curing and light-curing. Chemical or self-curing resins involve a chemical activator like N,N-dimethyl-p-toluidine. In the case of heat-curing materials, heat can be generated by hot water bath, while the light-curing use visible light as energy source, [1].

The current trend in dentures technology is that the material can be sufficiently handled by the technician and respectively its polymerization and processing to become faster.

One of the important issues regarding the use of acrylic resins in dental prosthetics is their biodegradation. This can be defined as the changes on their chemical, physical and mechanical properties due to the oral environment conditions, [1]. The main factors responsible for the biodegradation of the acrylic resins are the water absorption from saliva, chewing forces and the thermal and chemical dietary changes, respectively.

In the mastication process, the fracture of these materials can occur due to a mechanical overloading, fatigue damage caused by relatively low repetitive loads, or due to impact loadings.

Repeated deflections during the functional and parafunctional phases lead to the occurrence of microcracks in the area of high stress concentration. The persistence of the loadings associated with material imperfections determines the growth and unification of the microcracks, generating macrocracks and finally failure of the bases.

One of the problems that is reflected in the high frequency of failures in the denture bases is the mechanical strength of the acrylic resins. On the other hand, considering the wide range of acrylic resins used in making dentures, a comparative experimental study on the determination of the mechanical properties is absolutely necessary.

Six acrylic resins commonly used as denture bases were in an experimental study to determine the mechanical properties for tensile and bending loadings. Sample preparation was performed according to manufacturer's recommendations, within the Laboratory of Dental Technology from ''Victor Babes'' University of Medicine and Pharmacy. Also, the tensile and bending tests were carried out at the ''Stefan Nadasan'' Strength of Materials Laboratory from Politehnica University of Timisoara, on a Zwick/Roell testing machine of 5 kN. From each material, 5 samples were tested both in tensile, fig. 1.2, and bending loadings, fig. 1.3.

Mainly, the tested materials exhibited a linear elastic behaviour with brittle fracture, their mechanical properties being presented in Table 1.1.

Fig. 1.2. Tensile testing of acrylic resins

Fig. 1.3. Three-point bending testing of acrylic resins

Table 1.1. Tensile and bending properties of six acrylic resins

Name of acrylic resin	**Material type**	**Elasticity modulus, E [MPa]**		**Ultimate strength, R_m [MPa]**		**Elongation A_t [%]**
		Tensile	**Bending**	**Tensile**	**Bending**	**Tensile**
Vertex (Vertex™ Soft, Holand)	Self-curing	1223	2400	67.73	108	4.45
Triplex (Ivoclar, Schaan, Lichtenstein)	Heat-curing	3048	2640	65.67	95	4.97
Superacryl	Heat-curing	5333	3400	64.77	105	11.96

SpofaDental, Czech Republic)						
Royaldent (Royaldent, Palatinal Foggyarto KFT, Gyongyos Batthyany, Hungary)	Heat-curing	1182.5	2300	75.34	121	8.46
Meliodent (Heraeus Kulzer, Senden, Germany)	Heat-curing	1215	3100	68.62	118	8.76
Eclipse Base Plate (Dentsply International, DeguDent GmbH, Hanau, Germany)	Light-curing	3390	3600	76.65	127	2.83
Eclipse Contour (Dentsply International, DeguDent GmbH, Hanau, Germany)	Light-curing	4255	-	44.82	-	1.12
Eclipse Setup (Dentsply International, DeguDent GmbH, Hanau, Germany)	Light-curing	3795	-	70.07	-	2.28

1.1.2. Fracture toughness of acrylic resins

Generally, the manufacturing technologies of acrylic resins can lead to dental prostheses with structural defects. These structural defects are stress concentrators that can cause cracks leading to failure of prostheses. For these reasons it is necessary to determine the strength of acrylic resins taking into account the existence of a defect.

Fracture toughness is a property characterizing the material resistance to crack extension and establishes a link between the critical stress in the material and the magnitude of the defect. The fracture toughness is expressed based on Fracture Mechanics parameters and depends on the initial crack length, the shape of the crack and specimen, respectively the loading mode.

The stress intensity factor, K, or its equivalent the elastic energy release rate, G, the J-integral, the crack-tip opening displacement (CTOD), and the crack-tip opening angle (CTOA) are the most important parameters used in Fracture Mechanics. These parameters are also defined based on three main fracture modes, fig. 1.4.

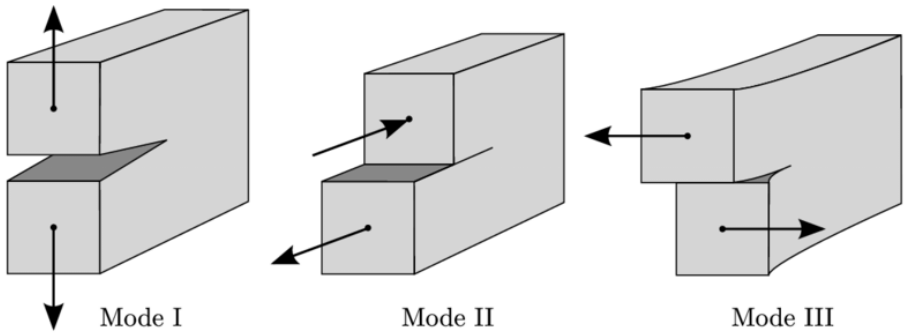

Fig. 1.4. The principal fracture modes: Normal opening fracture (Mode I), in-plane shear fracture (Mode II), out-of-plane shear fracture (Mode III).

The material deformation behaviour can be characterized as being linear elastic, nonlinear elastic, or elastic–plastic. In general, the deformation behaviour of a material determines which fracture parameter to be used for describing fracture toughness and which fracture test method to be adopted for measuring the toughness value for the material. When the material behaviour is linear elastic, the plastic zone at the crack tip can be very small compared to the specimen size and brittle fracture results, even with ductile micromechanisms predominating on the fracture surface. In this case, the critical stress intensity factor, K_{Ic}, is an appropriate fracture parameter, [2]. The recommended specimens for the plane strain fracture toughness K_{Ic} testing are the single edge notch three-point bending specimen (SENB), compact-tension specimen (CT), disk-shaped compact-tension specimen (DCT), arc-shaped tension specimen (AT) and arc-shaped bend specimen (AB). The frequently used specimens are the first two, SENB and CT. These geometries are recommended over other configurations because these have predominantly bending stress states which allow smaller specimen sizes to achieve plane strain.

In order, to determine the fracture toughness of acrylic resins, ASTM D5045 standard, [3], has been followed for two materials, Royaldent (heat-curing resin) and Eclipse (light-curing resin). Figure 1.5.a and b shows the dimensions of the CT and SENB samples prepared according to standard recommendations.

For a valid K_{Ic} it is first necessary to calculate a conditional result, K_Q, which implies loading the specimen and record the variation of force in function of the displacement of the loading point. On the force variation curve, a straight line corresponding to a 5 % compliance greater than that of the linear part of the loading curve is drawn until intersects the curve at point P_Q. If the maximum load that the specimen was able to sustain, P_{max}, is before the P_Q point, than P_{max} load is used to calculate K_Q, fig. 1.6.a. If the maximum load is placed after the intersection between the straight line and the loading curve, than the P_Q point is used to calculate K_Q, fig. 1.6.b.

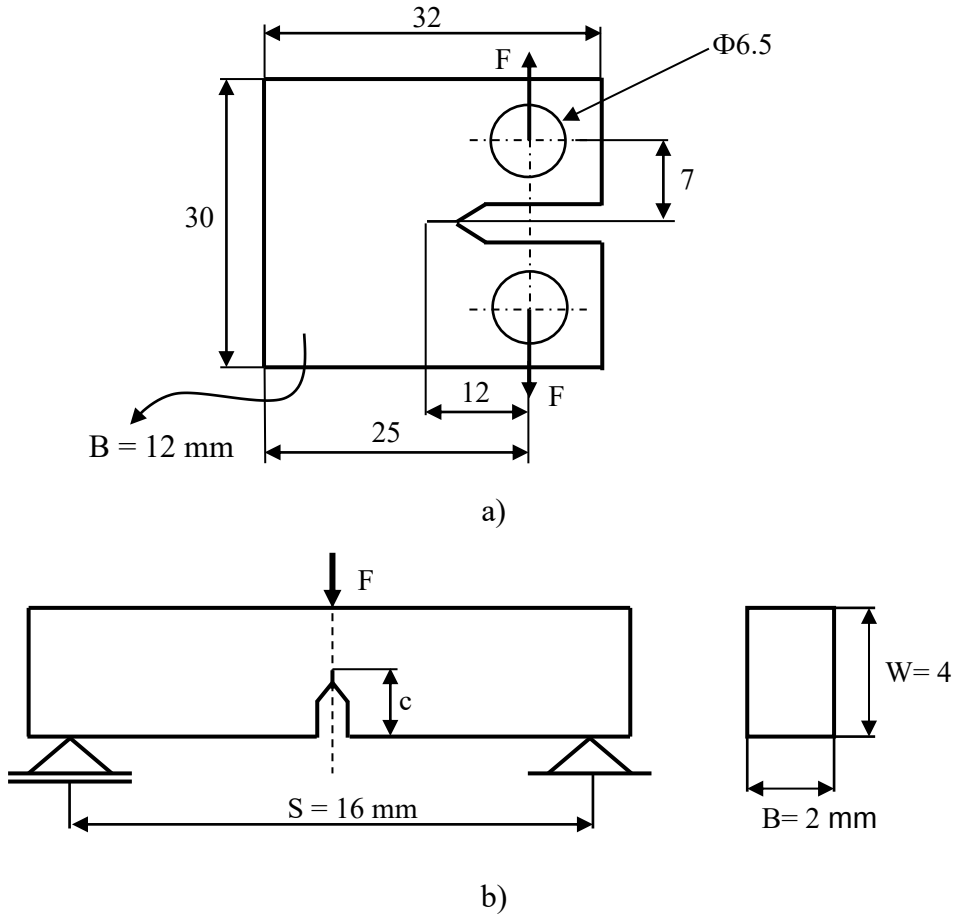

Fig. 1.5. Fracture Mechanics specimens: a) CT specimen; b) SENB specimen

The critical stress intensity factor is calculated based on the following relationships depending on the type of sample used.

- For CT sample:

$$K_Q = \frac{P_Q}{B \cdot W^{0.5}} \cdot f(x) \tag{1.1}$$

$$f(x) = \frac{(2+x)\cdot(0.886+4.64\cdot x-13.32\cdot x^2+14.72\cdot x^3-5.6\cdot x^4)}{(1-x)^{1.5}} \tag{1.2}$$

- For SENB sample:

$$K_Q = \frac{P_Q}{B \cdot W^{0.5}} \cdot f(x) \tag{1.3}$$

$$f(x) = 6 \cdot x^{0.5} \cdot \frac{[1.99 - x \cdot (1-x) \cdot (2.15 - 3.93 \cdot x + 2.7 \cdot x^2)]}{(1+2 \cdot x) \cdot (1-x)^{1.5}} \tag{1.4}$$

Once the K_Q is calculated, the validity criterion is checked based on the following relationship:

$$2.5 \cdot \left(\frac{K_Q}{\sigma_y}\right)^2 \leq B, a \; and \; (W - a) \tag{1.5}$$

where σ_y is the yield strength and a is the crack length.

If the relation (1.5) is satisfied, then $K_Q = K_{Ic}$ and represents the fracture toughness of the tested material.

Based on the procedure described above, the fracture toughness of the two acrylic resins was evaluated and the results are given in table 1.2.

Also, the Figures 1.7 and 1.8 shows the Fracture Mechanics specimens and testing rig used for fracture toughness determination.

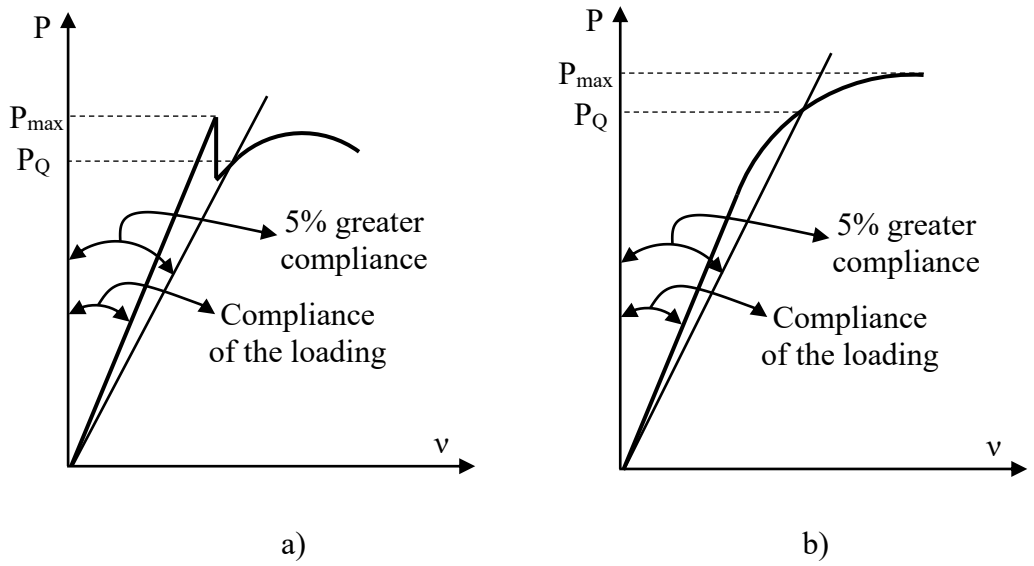

Fig. 1.6. The loading curve recorded in Fracture Mechanics test: a) the maximum load is recorded before P_Q; b) the maximum load is recorded after P_Q

For both types of specimens, the values obtained for fracture toughness are very close from one material to the other, which enhance the validity and accuracy of the testing procedure used. Also, the results confirm the linear elastic character with predominantly brittle fracture specific to most of acrylic resins, irrespective of the curing agent (heat or light). However, the fracture toughness values for the CT sample are closer to other references, [4], due to the fact

that the 12 mm thick CT sample provided better conditions for the plane strain state compared to SENB sample of 2 mm thickness.

Table 1.2. The fracture toughness of acrylic resins

Material	Type of acrylic resin	Fracture toughness, K_{Ic} [MPa√m]	
		CT	SENB
Royaldent	Heat-curing resin	1,39	2,18
Eclipse	Light-curing resin	1,34	1,98

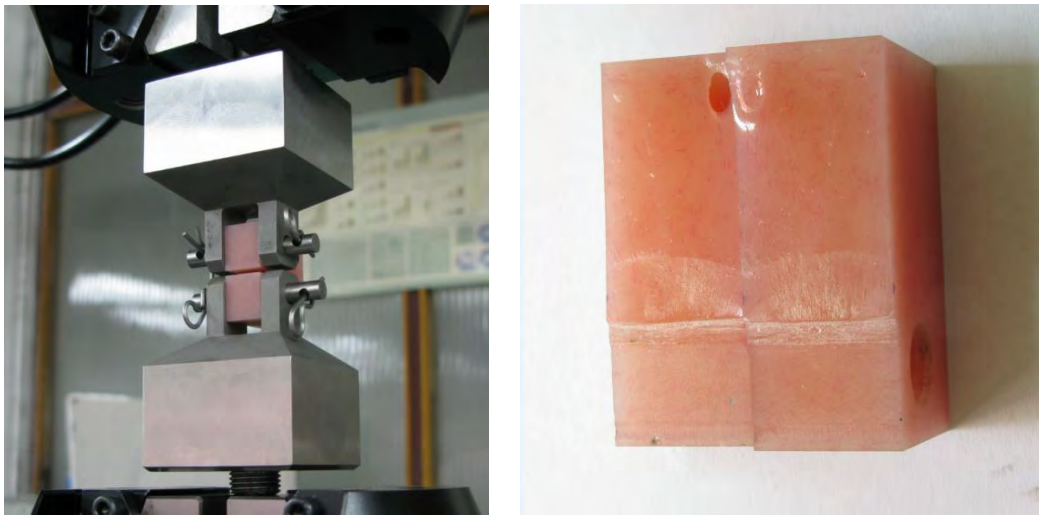

a) b)

Fig. 1.7. The CT sample from acrylic resin: a) sample mounted on the loading machine; b) the fracture surfaces after testing

Fig. 1.8. The SENB specimen from acrylic resin

1.1.3. Fatigue behaviour and fatigue crack propagation in acrylic resins

The fracture of dentures is a common clinical occurrence in prosthodontic service that is still a problem in consideration. Most fractures of the denture occur inside the mouth during function, primarily because of resin fatigue failure, [5]. Fatigue of acrylic resins originates from stress concentration areas or micro flaws, from which cracks are propagated resulting in complete failure, [6, 7]. Due to the brittle behaviour, the presence of structural micro voids and defects, these materials have a high susceptibility to fail by initiation and rapid propagation of a crack.

Although there is a wide range of commercial acrylic resins used as base for dentures, there is a lack of studies and data on fatigue behaviour. Thus, the present study focus on the evaluation of fatigue behaviour and respectively fatigue crack propagation in commercial acrylic resins commonly used in dental practice.

Fatigue tests were carried out on two acrylic resins, namely Vertex and Superacryl, using a fatigue-testing machine Walter-Bai, LFV-10-HM, of 10 kN. The fatigue tests have been performed according to ASTM D7791 standard, [8], using a frequency of 2 Hz and stress ratio, R = 0. The stress ratio applied in the fatigue tests is similar to cyclic loadings during mastication.

The results are given as log-log curves in σ_{max} – N coordinates, where σ_{max} is the maximum stress of the loading cycle and N is the number of cycles until failure, fig. 1.9.

The fatigue tests indicate a slightly lower slope for Vertex resin compared to Superacryl, which may indicate a slightly higher durability and a better fatigue behavior, respectively. However, the difference between the fatigue limits corresponding to the durability of 10^6 cycles and calculated based on the equations of the two curves, is too low to support a better fatigue behavior of one of the two analyzed resins, Table 1.3. The difference between the fatigue behavior of the two resins is more pronounced at durability under 1000 cycles, where a significant influence has the ultimate strength. Instead, over 1000 cycles the two fatigue curves intersect, indicating a similar fatigue behavior.

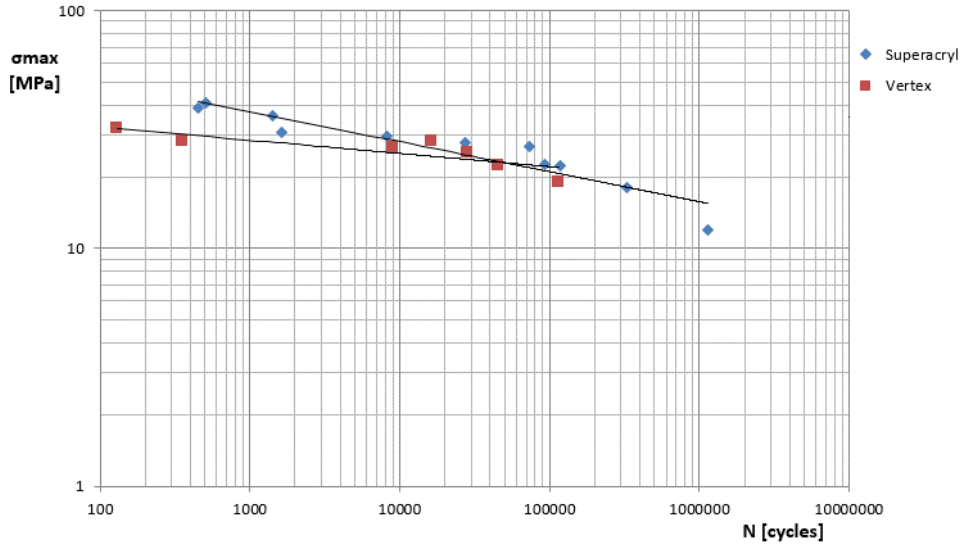

Fig. 1.9. The fatigue S-N curves for the tested acrylic resins, [5]

Table 1.3. The fatigue limits of the two acrylic resins, [5]

Materials	**Probability of failure/Confidence level [%]**	**S-N equations**	**Fatigue limits at 10^6 cycles [MPa]**
Vertex	50/50	$\sigma_{max} = 57.248 \cdot N^{-0.091}$	16.28
	90/10	$\sigma_{max} = 37.126 \cdot N^{-0.08}$	12.29
Superacryl	50/50	$\sigma_{max} = 107.01 \cdot N^{-0.147}$	14.04
	90/10	$\sigma_{max} = 69.383 \cdot N^{-0.135}$	10.74

Fatigue crack propagation tests were performed on CT specimens from acrylic resins, according to the ASTM E647 standard, [9]. The tested materials are Meliodent and Royaldent and have been prepared in accordance to the manufacturer recommendations in the form of plates with dimensions of 50 x 48 x 4 mm. The notches of the CT specimens were cut with a cutter milling for acrylic resins, driven by a SR250 T micromotor (Sirio, Italy). A 0.1 mm diamond-sawing disk was used to create a V-notch with a_0/W ratio of 0.2, fig. 1.10.

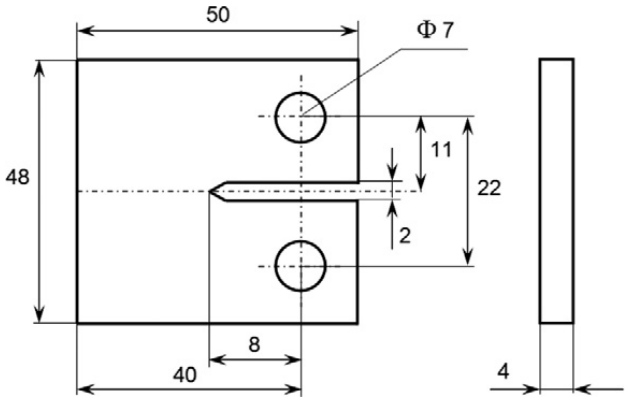

Fig. 1.10. CT specimen for fatigue crack propagation tests, [9].

Sinusoidal cyclic loading was applied at a frequency of 2 Hz and with different stress ratio, R. The crack length, a, was indirectly expressed as a function of the compliance of a specimen during fatigue loading, which was calculated by the CMOD (Crack-Mouth-Opening-Displacement) using a Fracture Mechanics extensometer, fig. 1.11. The crack length was expressed by the following equation:

$$\frac{a}{W} = C_0 + C_1 \cdot u_x + C_2 \cdot u_x^2 + C_3 \cdot u_x^3 + C_4 \cdot u_x^4 + C_5 \cdot u_x^5 \tag{1.6}$$

$$u_x = \left\{\left[\frac{E \cdot v \cdot B}{P}\right]^{0.5}\right\}^{-1} \tag{1.7}$$

where W us the width of the specimen, $C_{0\text{-}5}$ the regression constants, u_x is expressed by the compliance of the specimen during fatigue loading (v/P), the thickness of the specimen (B), and Young's modulus of the material (E).

To determine the regression constants $C_{0\text{-}5}$ an image registration system was used during the application of fatigue loading, based on a video camera, model Creative, fig. 1.11. On the samples were drawn grids (with 2 mm distance between grids) for measure the crack length, fig. 1.12. Based on the correlation between the registered images and the number of the loading cycles were determined the compliance curves, ($a/W = f(u_x)$), for Meliodent and Royaldent resins, figs. 1.13 and 1.14.

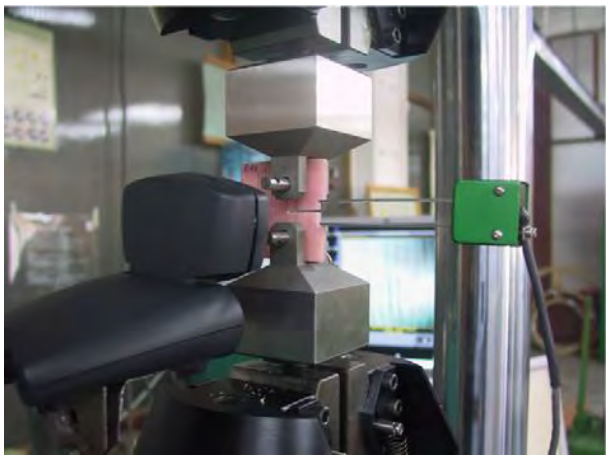

Fig. 1.11. The systems for crack length measurements, [9]

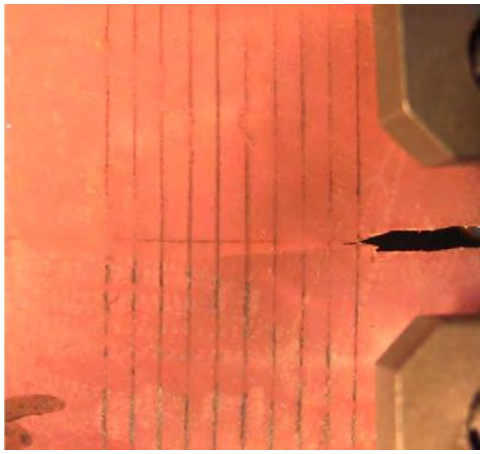

Fig. 1.12. The grids on the sample for crack length measurements, [9]

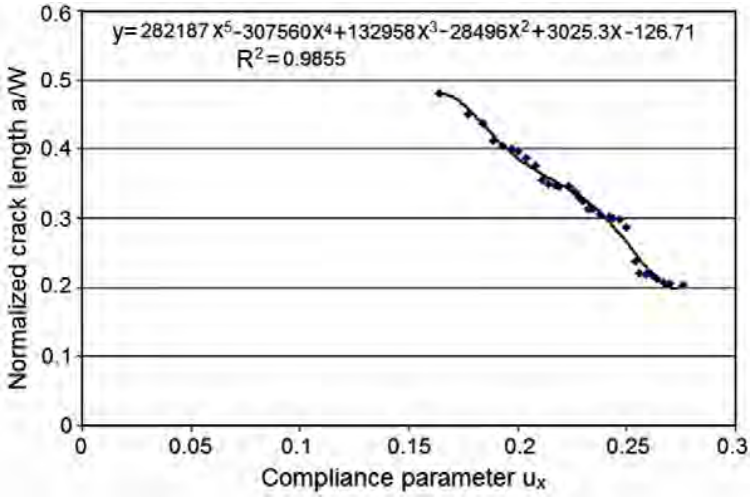

Fig. 1.13. The compliance curve for Meliodent resin, [9]

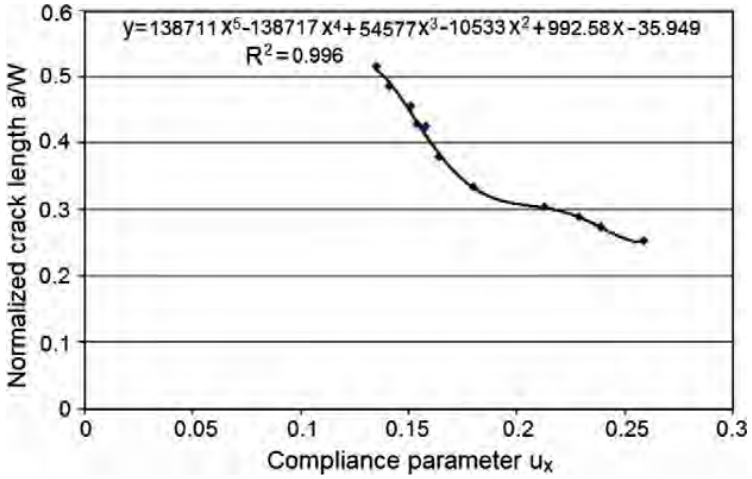

Fig. 1.14. The compliance curve for Royaldent resin, [9]

The fatigue crack growth tests were conducted for the notched specimens without the existence of a fatigue pre-cracking.

For both tested materials, the fatigue crack growth rate has been expressed in terms of crack length, a, figs. 1.15 and 1.16. In addition, the Meliodent samples were tested under variable amplitude loading with positive stress ratios continuously increasing from 0.2 to 0.7, instead the Royaldent samples have been tested with variable amplitude loading starting from negative stress ratios (-0.2) and continuously increasing to positive stress ratios up to 0.2.

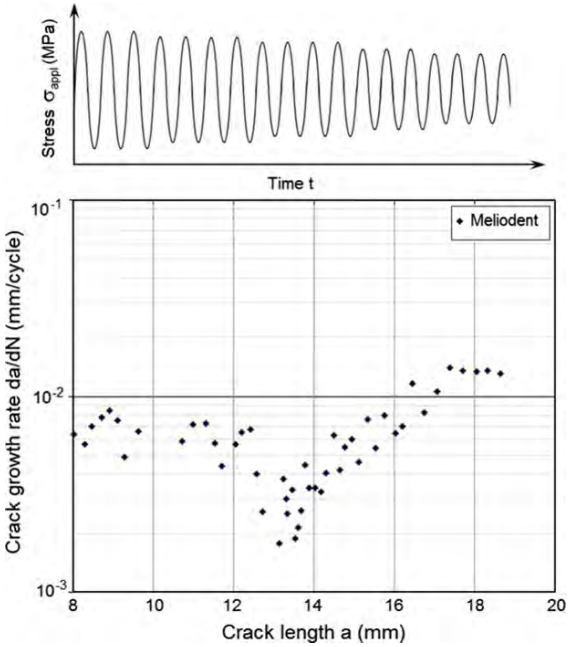

Fig. 1.15. The fatigue crack growth rate function of crack length, for Meliodent resin, [9]

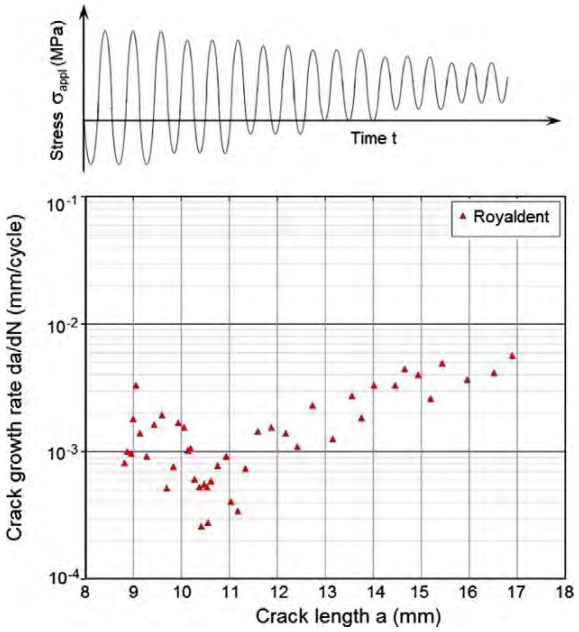

Fig. 1.16. The fatigue crack growth rate function of crack length, for Royaldent resin, [9]

The results show that near the notch, the fatigue crack growth rate decreases to a certain value then continue to grow, as the crack length and stress ratio increases. The relationship between the crack growth rate, da/dN, and the crack length may form a ‘‘V’’ shape for the crack growth from a notch. Many studies have been reported about the ‘‘anomalous’’ crack growth behaviour near the notches, [10, 11]. By testing specimens with a sharp notch under several R-ratios, Tanaka and Nakai [12], found that crack closure was the major cause of the ‘‘V’’ shaped da/dN = f(ΔK) curve for the early stage crack growth from the notch. They found that fatigue crack nucleated at the sharp notch decelerated first with the increase in crack length followed by an acceleration in crack growth rate or non-propagating crack depending on the applied load level. Also, the notch effect on the fatigue crack propagation

decreases as the crack length increases, figs. 1.15 and 1.16. When the crack is short, it is embedded totally in the notch effect field. When the crack length is about 13 mm for Meliodent and 10.5 mm for Royaldent, the crack tip is totally out of the notch effect field. For a short crack growing within the notch effect field, the closure effect is accentuated by the notch plastic field surrounding the notch tip, fig. 1.17.

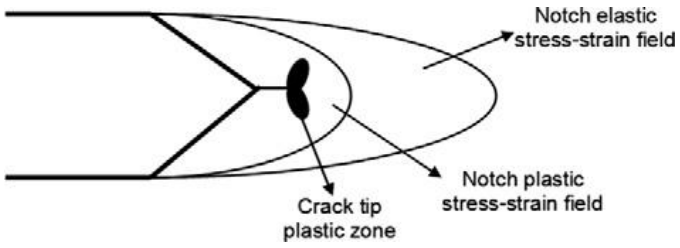

Fig. 1.17. Schematic of a fatigue crack emanating from a notch and the associated local elastic and plastic stress-strain field, [9].

1.1.4. The strength and structural integrity of complete dentures

Tooth loss affects the ability of mastication and speech of patients with a negative effect on the quality of social and personal life. To restore these functions, removable and complete dentures are often used. The selection of materials for the construction of dentures is crucial because this directly relates to the performance and life span of the appliance during service in the oral cavity. Due, to the brittle fracture behaviour and sometimes the processing technology of acrylic resins, there can be obtained complete dentures with small defects which can initiate cracks and resulting in failure of total denture before the expected life time. The longevity of the maxillary complete dentures for patients with occlusion against mandibular natural dentitions is about 21 months, whereas the average denture life time for those with occlusion against artificial mandibular teeth is of about 10 years, [13].

The relative short life time of the maxillary dentures has led researchers [14, 15] to investigate the causes of fracture by studying the stress distribution upon mastication and to find ways to improve their mechanical performance. Different methods such as electrical resistance strain gage, brittle lacquer, photoelasticity and finite element analysis have been used for investigating strain or stress distribution during deformation of dentures. The finite element method (FEM) has been used for five decades for numerical stress analysis. 2D FEM can be applied to analyse structures with 2D plane symmetry. It complements or even eliminates the use of complicated experimental methods. The advent of 3D FEM further enables researchers to perform stress analysis on complicated geometries such as complete

dentures and provides a more detailed evaluation of the complete state of stress in the structures.

The aims of this study is to investigate the stress distribution and structural integrity of a maxillary complete denture based on a proposed methodology involving FEM analysis, and the mechanical properties respectively Fracture Mechanics parameters of the material, [16].

The methodology is outlined in figure 1.18 and requires a detailed experimental analysis of the material, then based on loading and boundary conditions similar to those in the mouth the stress and strain fields in complete denture are evaluated.

Reverse engineering technology was employed to convert a real maxillary complete denture, made of light curing resin, Eclipse, into a virtual numerical model, [17]. A thin layer of green dye (Okklean, Occlusion spray, DFS, Germany) was sprayed onto the surface of the denture to increase its contrast for scanning. The denture was positioned on a rotating table of a Roland 3D scanner, model LPX-1200, and scanned with a scanning pitch of 0.1 x 0.1 mm. The scanned surfaces of the denture were then imported in Pixform Pro software (INUS Technology, Seoul, Korea), which combine the surfaces and repair any defects to create a fully closed surface network. The hollow denture was exported in initial graphics exchange specification (IGES) format and then imported in Solid Works software for conversion into a solid model, fig. 1.19.

Using the FEM software package, ABAQUS v6.9.3, [18], on the geometrical model of the complete denture a stress and strain analysis was performed. The maximum force of mastication in a patient with complete denture is between 60 and 80 N. For this loading case was considered a mastication force of 70 N distributed on palatal cusps of the upper teeth, fig. 1.20.a. The areas with distributed force are about 46.666 mm2 and the result is a normal pressure of 1.5 MPa. To fix the model, there have been applied supports on surfaces shown in fig. 1.20.b. The supports from denture channel allow a 0.2 mm displacement in vertical direction and stop the displacements in horizontal plane. Also, the supports from palatal vault allow a 0.1 mm displacement in vertical direction and stop the displacements in horizontal plane. Allowed displacements were considered to replace the deformations of the oral mucosa.

The geometrical model was meshed in tetrahedral finite elements, C3D8 (154,742 elements) and based on FEM simulation were determined the Maximum Principal Stress (Fig. 1.21.a) and Maximum Principal Strain (Fig. 1.21.b).

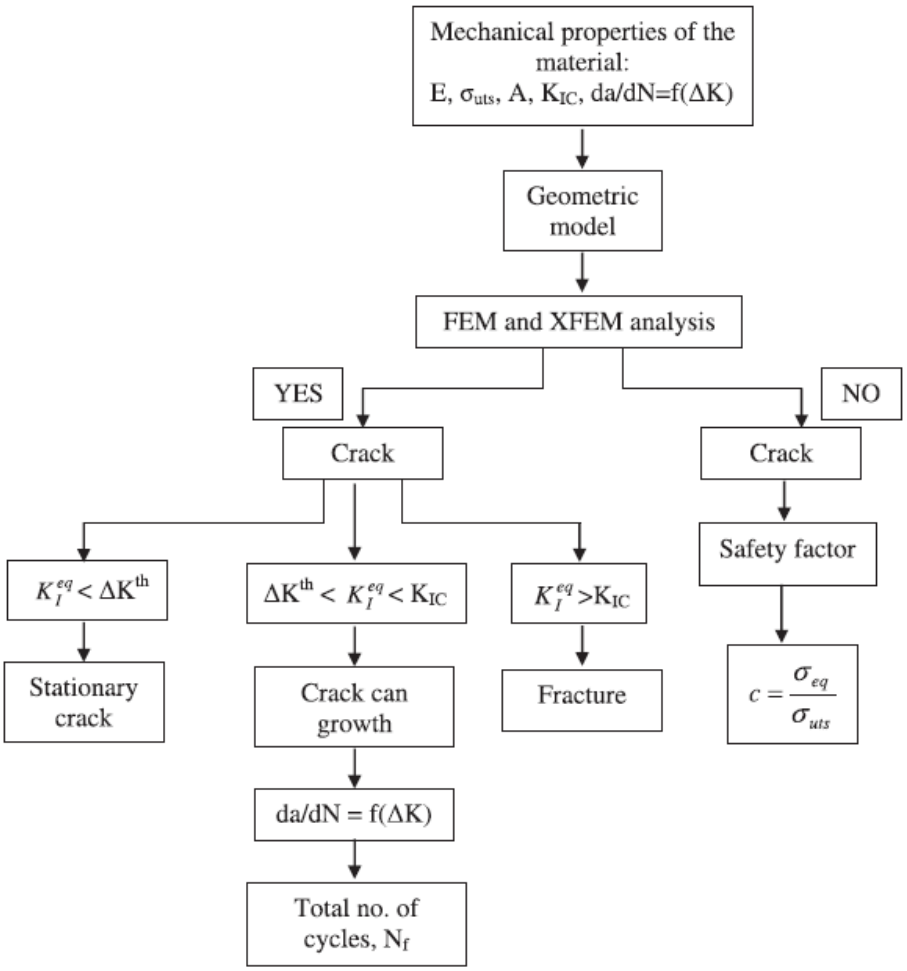

Fig. 1.18. Procedure for mechanical strength and structural integrity assessment of dental prosthesis: E – Young's modulus, σ_{uts} – ultimate tensile strength; A – total elongation, K_{Ic} – fracture toughness, da/dN – fatigue crack growth rate, ΔK – stress intensity factor range, ΔK_{th} – threshold stress intensity factor range, c – safety factor, K^{eq} – the equivalent stress intensity factor, [16].

a)

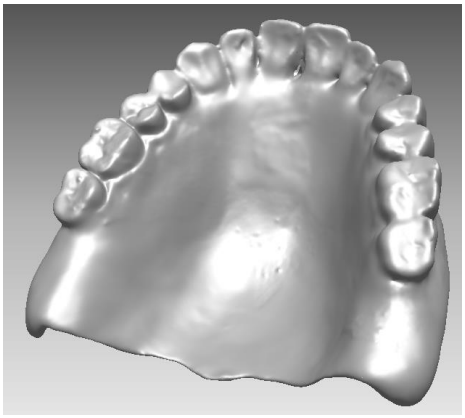

b)

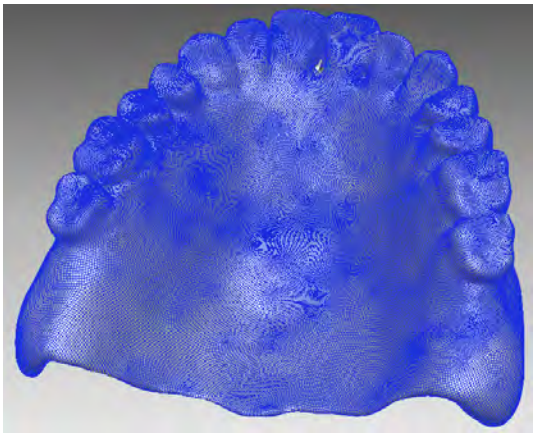

c)

Fig. 1.19. 3D modelling of complete denture: a) 3D scanning of a real denture; b) closed polygon mesh; c) NURBS surfaces network, [17].

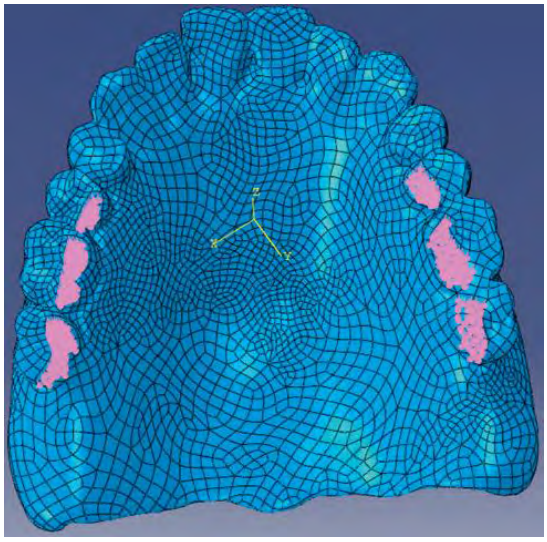

a)

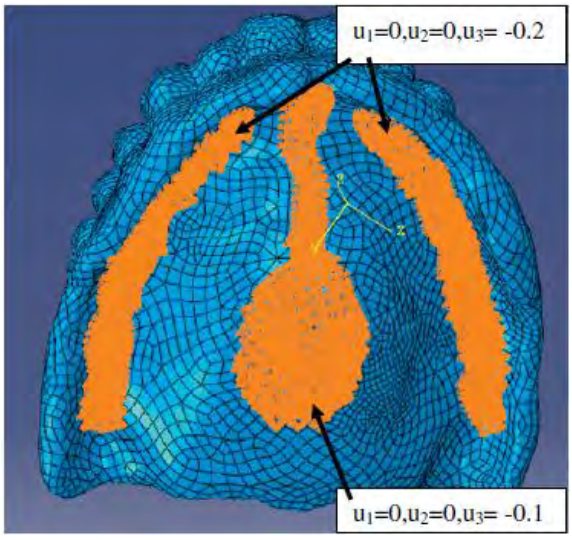

b)

Fig. 1.20. The boundary conditions on complete denture: a) normal pressure; b) displacement conditions, [16].

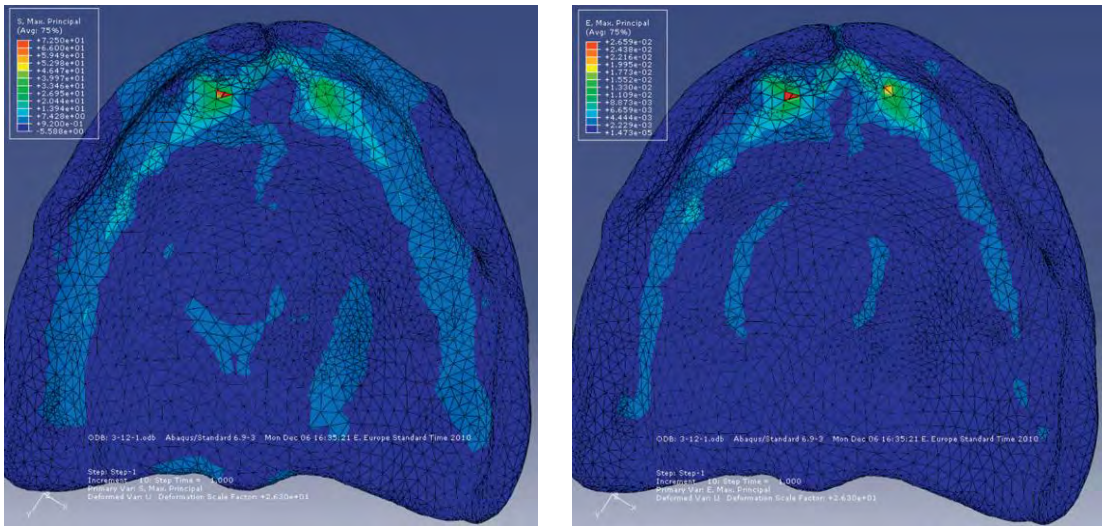

a) b)

Fig. 1.21. The stress and strain fields on complete denture: a) Maximum Principal Stress; b) Maximum Principal Strain, [16].

Using the XFEM procedure (Extended Finite Element Method), incorporated in ABAQUS, can be determined whether the applied load can initiate a crack or not, where it is initiated and respectively the stress intensity factors at the crack tip. If the applied pressure does not cause a crack initiation, a safety factor (c) is calculated as shown in Fig. 1.18. If the pressure cause a crack initiation (Fig. 1.22), then the values of stress intensity factors at the crack tip are calculated, in order to determine an equivalent stress intensity factor, K_I^{eq}, and compare it with the fracture toughness, K_{Ic}.

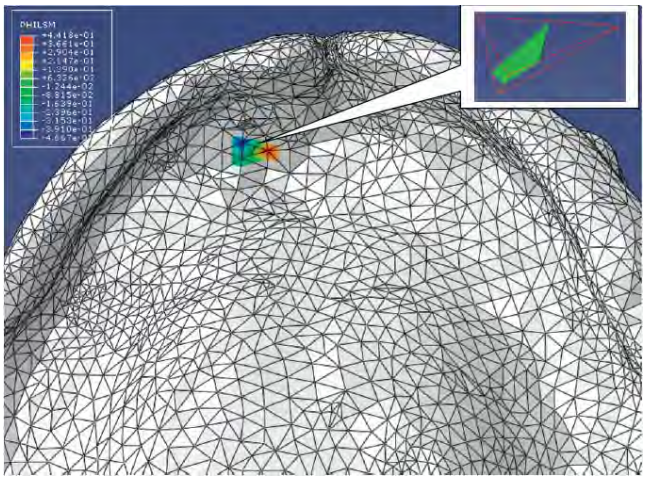

Fig. 1.22. The Heaviside function of enriched node, crack location, enriched element and crack surface, [16].

The XFEM method is based on the enrichment of the finite element with additional degrees of freedom (DOFs) that are tied to the nodes of the elements intersected by the crack, [18]. In this manner, the discontinuity is included in the numerical model without modifying the numerical discretization, as the mesh is generated without taking into account the presence of the crack. Therefore, only a single mesh is needed for any crack length and orientation. In addition, nodes surrounding the crack tip are enriched with DOFs associated with functions that reproduce the asymptotic LEFM fields. This enables the modelling of the crack discontinuity within the crack-tip element and substantially increases the accuracy in the computation of the stress intensity factors (SIFs).

The nodal displacement for crack modelling in the extended finite element method is given by the following relationship:

$$u_{XFEM}(x) = \sum_{i \in I} N_i(x) \cdot u_i + \sum_{i \in \Lambda} N_i(x) \cdot H(x) \cdot u_i + \sum_{i \in K}[N_i(x) \cdot \sum_{\alpha=1}^{4} F_\alpha(x) \cdot b_{i\alpha}] \quad (1.8)$$

$$[F_\alpha(r,\theta), \alpha = 1-4] = \left[\sqrt{r} \cdot sin\frac{\theta}{2}, \sqrt{r} \cdot cos\frac{\theta}{2}, \sqrt{r} \cdot sin\frac{\theta}{2} \cdot \sin\theta, \sqrt{r} \cdot cos\frac{\theta}{2} \cdot \sin\theta\right] \quad (1.9)$$

where Γ is the set of all nodes in the mesh, $N_i(x)$ is the nodal shape function and u_i is the standard DOF of node i. The subsets Λ and K contain the nodes enriched with Heaviside function $H(x)$ or the crack-tip functions $F_\alpha(x)$, respectively a_i, $b_{i\alpha}$ are the corresponding DOFs, and r, θ are local polar coordinates defined at the crack tip.

Once the nodal displacements obtained for the crack-tip nodes with XFEM procedure, the stress intensity factors K_I and K_{II} were evaluated. The equivalent stress intensity factor, K_I^{eq}, is also computed based on the following relationships:

$$\theta_c = 2tan^{-1}\left[\frac{1}{4}\left(\frac{K_I}{K_{II}} + sign(K_{II})\sqrt{8 + \left(\frac{K_I}{K_{II}}\right)^2}\right)\right] \quad (1.10)$$

$$K_I^{eq} = K_I \cdot cos^3\left(\frac{\theta_c}{2}\right) - \frac{3}{2} \cdot K_{II} \cdot cos\left(\frac{\theta_c}{2}\right) \cdot sin\,\theta_c \quad (1.11)$$

where θ_c is the angle of crack propagation direction.

After processing all calculations, the maximum values of stress intensity factors on the crack front were determined as K_I = 2.0121 MPa√mm, K_{II} = -10.996 MPa√mm, θ_c = 67.076° and the corresponding K_I^{eq}= 7.42 MPa√mm.

The value of equivalent stress intensity factor is less than ΔK_{th} = 14.228 MPa√mm (experimentally determined based on fatigue crack propagation tests), respectively K_{Ic} = 43.639 MPa√mm, and according to the proposed methodology it is considered that the initiated crack does not propagate and becomes a stationary crack.

In this study, the Maximum Principal Stress criterion for brittle fracture was used for evaluation the stress distribution in complete denture. Next, the fracture risk must be analysed, considering that a crack is initiated. Also, must be analysed which are the factors with highest weight in the fracture risk of the denture – the crack initiated or the Maximum Principal Stress.

The Failure Assessment Diagram (FAD) approach was used to evaluate the fracture risk of the analysed complete denture. The FAD diagram is a concept of a two failure criteria to describe the interaction between fracture and collapse. This diagram is defined in terms of two parameters:

K_r – the ratio of the applied linear elastic stress intensity factor (K_I^{eq} in this case) to the materials fracture toughness, K_{Ic};

S_r – the ratio of the applied stress to the stress to cause collapse of the cracked structure.

For the construction of FAD diagram, the following equation is used:

$$K_r = S_r \cdot \left[\frac{8}{\pi^2} \cdot lnsec\left(\frac{\pi}{2} S_r\right)\right]^{-0.5} \tag{1.12}$$

The failure analysis of complete denture is represented in the FAD diagram by point A (K_r = 0.17 and S_r = 0.945), fig. 1.23.

In the FAD diagram, the point A is in the safe area but too close to the limit of S_r, indicating a high risk of fracture and that failure is controlled by the Maximum Principal Stress. The fracture probability of the denture is very high, 94.5 % (S_r = 0.945) for this loading case.

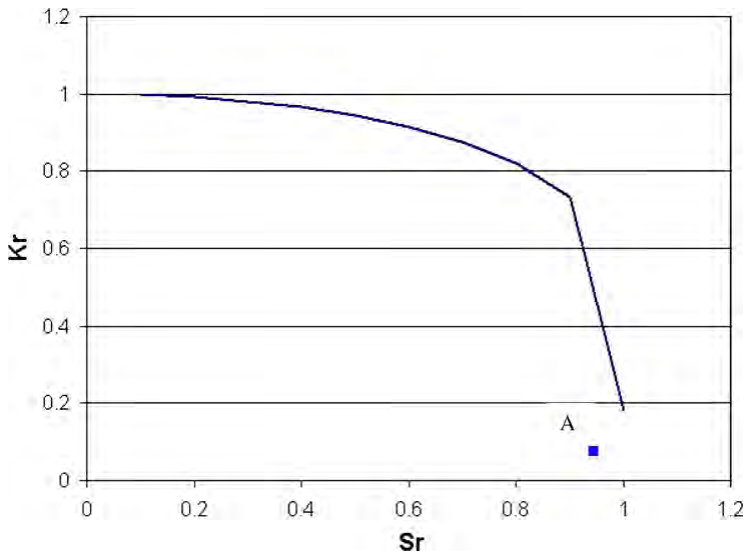

Fig. 1.23. The FAD diagram and corresponding point of the analysed complete denture, [16].

For a complete evaluation of the denture strength, an experimental study was conducted based on which real dentures were tested until complete failure. Thus, dentures made from Superacryl resin were tested in compression in two cases: compression without pre-fatigue testing and compression after 20000 fatigue cycles with R = 0. In both cases, the dentures were tested on an experimental stand developed in the laboratory and that simulated the dentures placement in the oral cavity, fig. 1.24. Also, strain gage have been used in different areas of the denture to assess their deformation, fig. 1.25. The testing device consists of a cast model from Co-Cr-Mo alloy with a profile that simulates the oral cavity. On this model, a silicon layer with a similar constitution and stiffness as oral mucosa, is placed. Also, on the model obtained, the dentures are placed, fig. 1.24.a, and then fixed in a guiding device, fig. 1.24.b. Once the whole arrangement is completed, it can be mounted on the testing machine, fig. 1.24.c.

Using such a testing stand there are ensured the placement conditions of the denture in the oral cavity. Testing was also performed on pairs of dentures, thereby providing a simulation even closer to the conditions in the oral cavity by the fact that the teeth on a denture are in direct contact with the corresponding teeth on the dentures pair.

Selection of the areas were strain gage were placed was made based on the numerical simulations and practice reports which show that most of the maxillary dentures fails in the medial area. Also, the strain gage were connected to a Wheatstone bridge Vishay based on which the denture deformation was recorded until failure.

In the case of compression with fatigue tests, the dentures were loaded in fatigue until 20000 cycles and after that a compression test was done. The number of loading cycles applied is the equivalent of one year of use of the denture. Thus, it was possible to check whether the strength and stiffness of the denture changed after about one year of use.

Table 1.4 presents results of compression tests performed on dentures.

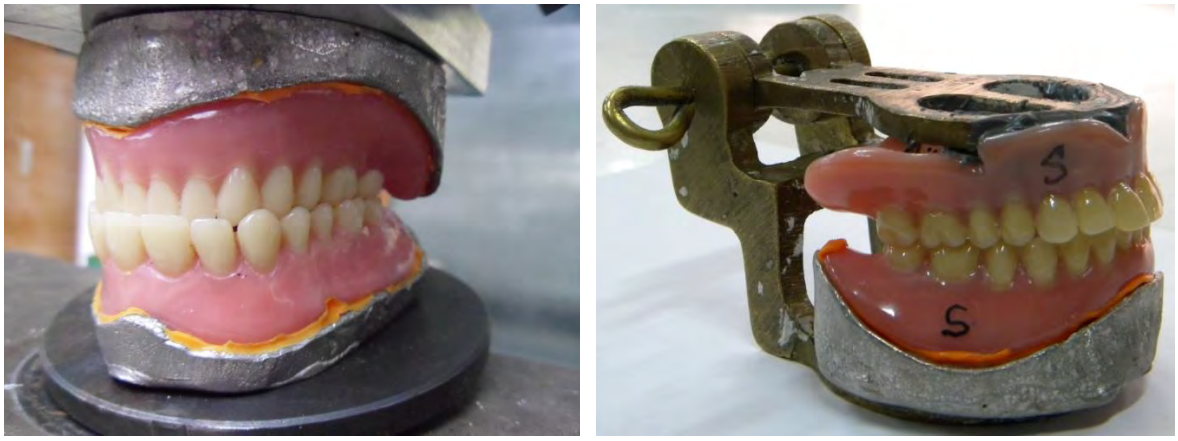

a) b)

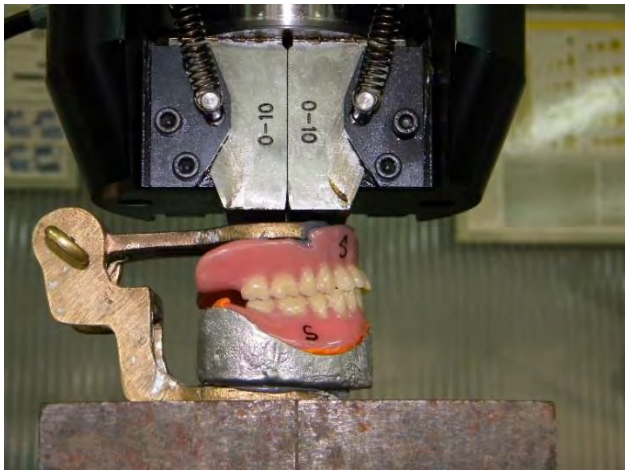

c)

Fig. 1.24. Arrangement setup for compression testing of complete dentures: a) the dentures fixed on a cast model; b) dentures arrangement fixed in a guiding device; c) the dentures arrangement placed on the testing machine

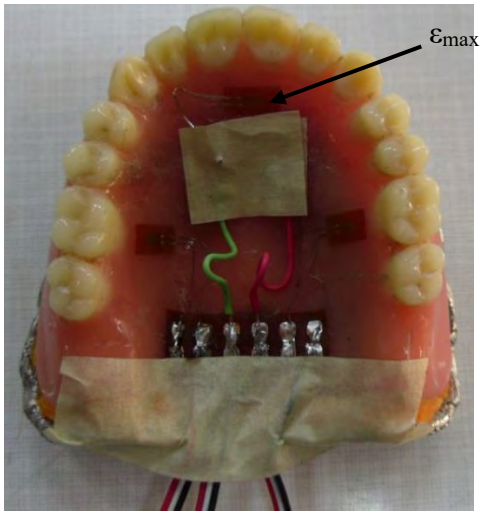

Fig. 1.25. Strain gage mounted on the denture

Table 1.4. Results of compression tests on dentures

Material	Compression tests		
	Pure compression	After 20000 cycles	
		F_{max} = 800 N; R = 0;	F_{max} = 1500; R = 0
Superacryl	F_r = 2968,5 N ε_{max} = 5984 μm/m	F_r = 4745.7 N ε_{max} = 10114 μm/m	F_r = 4149.3 N ε_{max} = 6432 μm/m

The results indicate a tendency to stiffen the denture due to fatigue loading. This observation needs special attention.

Instead, the maximum deformation recorded after 20000 cycles is influenced by the silicone layer on which the denture is placed. This can degrades under fatigue loading. At the same time, damage of the silicone layer signals the bone remodelling process that occurs in the oral cavity during the use of denture. Also, due to fatigue loading, a pronounced wear of the teeth in the contact areas has been observed.

In all the tests performed, the failure occurred on the median line of the dentures, due to a crack that started between the incisive teeth (high stress concentration area), fig. 1.26.

Fig. 1.26. Failed dentures

1.2. Bending of sandwich beams loaded by a concentrated force

Through numerous industrial applications, sandwich structures proved to be the most effective elements of strength, stiffness and strain energy absorption. A sandwich structure consists of two thin and stiff face sheets connected by a thick, light and low-modulus core using different joining techniques, fig. 1.27. In most of the cases, the faces carry in-plane and out-of-plane loadings, while the core resists to transverse shear loads.

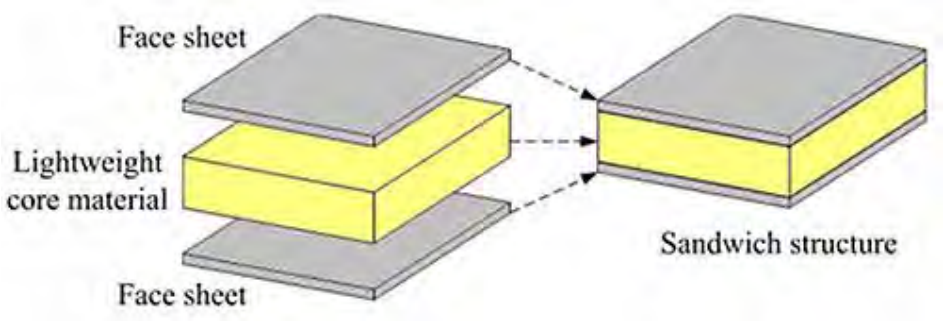

Fig. 1.27. Sandwich structure

The core material has a great importance for mechanical behaviour of the whole structure and is required to meet the following properties: low density in order to add as little as possible to the total weight; Young's modulus perpendicular to the face sheet should be fairly high to prevent excessive deformation in the thickness direction and therefore decrease in flexural stiffness. The core is mainly subjected to transverse shear stresses. The shear strains contribute to global deformation and thus the core must be chosen such that it would not fail under the applied out-of-plane loads and having a shear modulus high enough to give the required stiffness, [19]. The core materials have been fashioned in various forms and developed for a range of applications: foam or solid cores, honeycomb cores, web and truss cores.

In general, the mechanical behaviour of sandwich structures is evaluated experimentally on samples taken from the structure, according to the standard rules.

The bending stiffness is one of the properties that characterize the mechanical behaviour of the sandwich structure. This is given by the slope of the variation curve between the applied force and the vertical displacement of the point of application of force. This vertical displacement is often associated with the vertical deflection of the sandwich structure. In this regard, based on the Timoshenko beam theory, Allen [20] proposed the following relation for the total deflection, δ, at the mid-section of a sandwich beam loaded in 3-point bending:

$$\delta = \frac{F \cdot l^3}{48 \cdot EI_{eq}} + \frac{F \cdot l}{4 \cdot GA_{eq}} \tag{1.13}$$

where EI_{eq} is the equivalent bending stiffness of the sandwich beam and GA_{eq} is the equivalent shear stiffness of the sandwich beam and l is the span length.

The Equation (1.13) was generally accepted and assumes that in the loading plane the vertical deflection of the neutral axis is the same as the vertical displacement of the point of application of force. In reality there are very few cases in which this condition is valid. In the

case of bending of sandwich beams with flexible cores (e.g. foam, cork) and thin faces, the variation curve of the applied force and vertical deflection can be easily affected by the occurrence of some local effects such as indentation or core damage.

In this study the local effect given by the applied force on the bending deflection of sandwich beams was analyzed based on proposed equation related to bending moment, [21]. The local effect of the applied concentrated force is considered as the solution given by Timoshenko for these problems [22]. The bending deflection, considering local effects, have been determined using the first and Reddy's third-order shear deformation theory, [23] adapted for beams in bending.

1.2.1. Sandwich beam loaded by a concentrated force

According to elasticity theory of Timoshenko, near the point of application of concentrated force, a serious local perturbation in stress distribution should be expected and the problem must be considered for analysis. To find the solution of this problem, it is considered a concentrated vertical force P applied on a horizontal straight boundary AB of an infinitely large plate, Fig. 1.28.a. The distribution of the load along the thickness of the plate is uniform as indicated in Fig. 1.28.b. The thickness of the plate is taken as unity. Around the point of application of force P, the stress has a simple radial distribution. Any point A at a distance r from the point of application of the load is subjected to a simple compression in the radial direction and the radial stress is given by:

$$\sigma_r = -\frac{2P}{\pi} \cdot \frac{\cos\theta}{r} \tag{1.14}$$

$$r = d \cdot \cos\theta \tag{1.15}$$

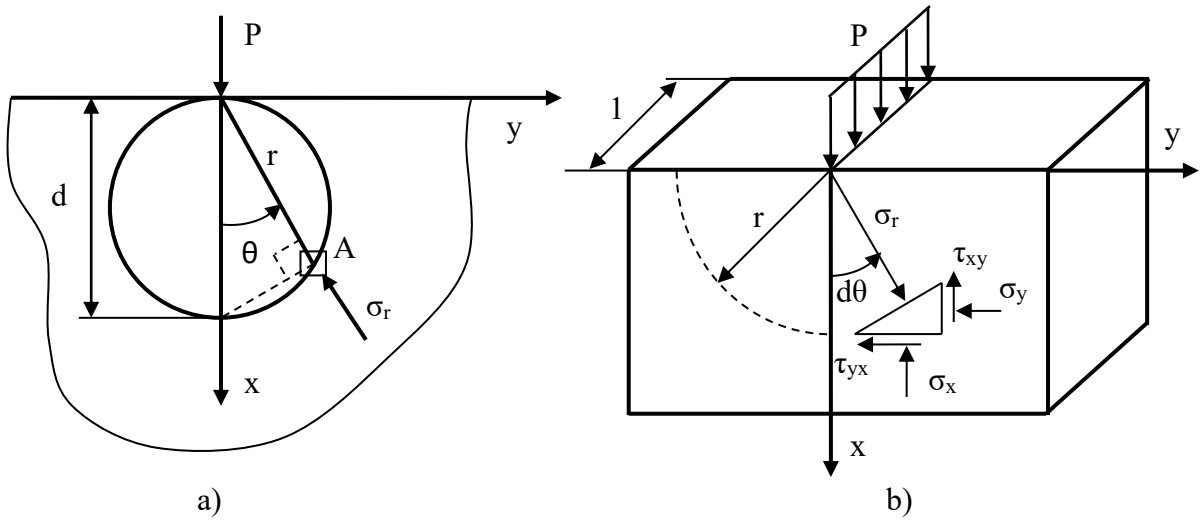

Fig. 1.28. The concentrated force at a point of a straight boundary, [21]

The tangential stress σ_θ and the shearing stress $\tau_{r\theta}$ are zero. Also, the boundary conditions are satisfied because σ_θ and $\tau_{r\theta}$ are zero along the straight edge of the plate, which is free from external forces except at the point of application of the load. Here σ_r becomes infinite. The resultant of the forces acting on a cylindrical surface of radius r (Fig. 1.28.b) must balance P. This is obtained by summing the vertical components $\sigma_r \cdot r \cdot d\theta$ acting on each element $r \cdot d\theta$ of the surface:

$$2\int_0^{\frac{\pi}{2}} \sigma_r \cos\theta \cdot r\, d\theta = -\frac{4P}{\pi} \cdot \int_0^{\frac{\pi}{2}} cos^2\,\theta\, d\theta = -P \tag{1.16}$$

In the case of a simply supported sandwich beam loaded in three-point bending by a concentrated force P applied at the midspan (Fig. 1.29.a), the total stress along the section AB, can be found by the superposition of the bending stress distribution and the stress created by the line load, given by Eq. (1.14) for a semi-infinite plate.

The radial pressure distribution created by the applied load over quadrant *ab* of the cylindrical surface *abc* at point A (Fig. 1.29.b) produce a horizontal and vertical force given by the relations (1.17) and (1.18), applied to A (Fig. 1.29.c).

$$\int_0^{\frac{\pi}{2}} (\sigma_r \sin\theta) \cdot r\, d\theta = \int_0^{\frac{\pi}{2}} \frac{2P}{\pi} \sin\theta \cdot \cos\theta\, d\theta = \frac{P}{\pi} \tag{1.17}$$

$$\int_{-\frac{\pi}{2}}^{\frac{\pi}{2}} (\sigma_r \sin\theta) \cdot r\, d\theta = \int_{-\frac{\pi}{2}}^{\frac{\pi}{2}} \frac{2P}{\pi}\, cos^2\,\theta\, d\theta = P \tag{1.18}$$

Thus, the bending moment about the point O is:

$$M_0 = \frac{Pl}{4} - \frac{P}{\pi} c \tag{1.19}$$

In these circumstances, the law of the bending moment variation for the entire beam is written in the following form:

$$M_{xx} = \left(\frac{P}{2} - \frac{2Pc}{\pi L}\right) \cdot x \tag{1.20}$$

For x = 0 in fig. 1.30, it results the bending moment M_1 = 0 and for x = L/2 results the bending moment M_o. The relation (1.20) is valid for the entire beam if the external applied force to the beam is equivalent to $P - \frac{4 \cdot P \cdot c}{\pi L}$. This means that when a concentrated force P is applied on a beam in three-point bending, its effect on the beam is equivalent to one given by a load equal to $P - \frac{4 \cdot P \cdot c}{\pi L}$.

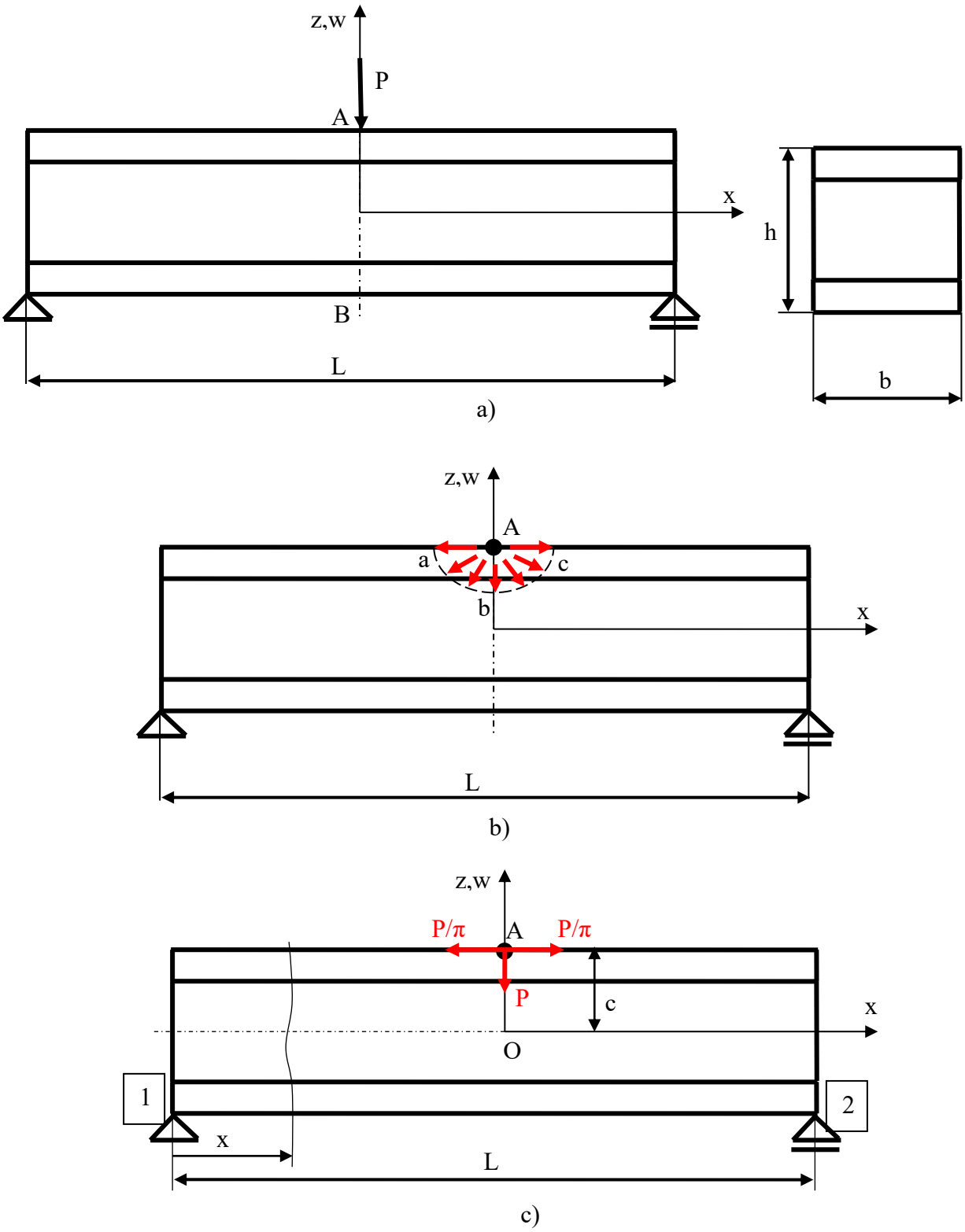

Fig. 1.29. The concentrated force applied on a sandwich beam: a) the loading scheme of three point bending; b) the radial pressure distribution created by the applied load; c) the horizontal and vertical forces resulted from radial pressure distribution, [21].

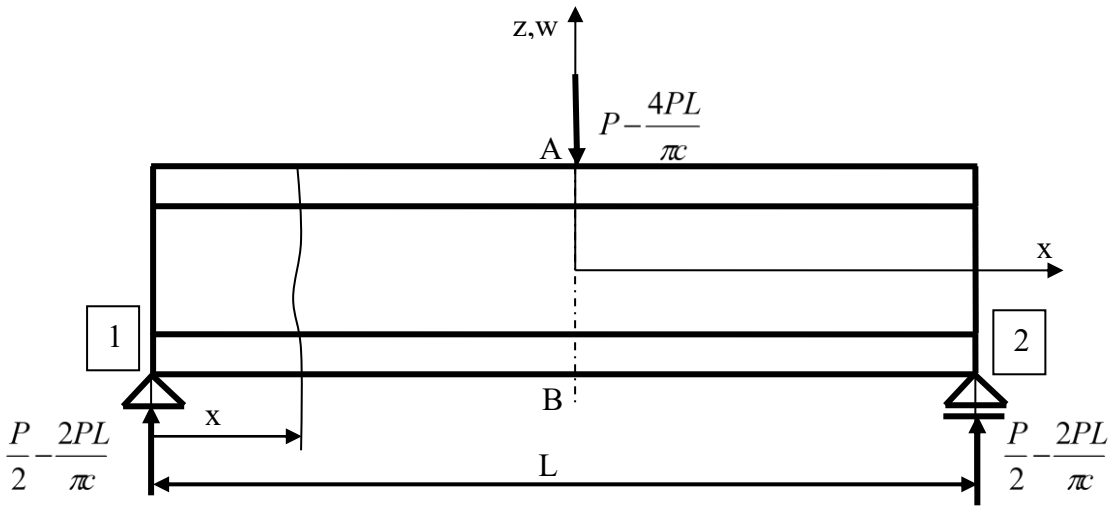

Fig. 1.30. The equivalent loading of the sandwich beam in three point bending, [21]

1.2.2. Bending deflection of sandwich beam by first-order shear deformation theory (FSDT)

The displacement field from a beam in bending, according to first-order shear deformation theory, is of the form, [24]:

$$u(x,z) = u_0(x) + z \cdot \varphi_x(x) \tag{1.21}$$

$$w(x,z) = w_0(x) \tag{1.22}$$

where φ_x denotes the rotation of the cross section about y-axis (normal on the x and z axes), u_0 and w_0 are the displacements of a point on the plane $z = 0$.

The linear strains associated with the displacement field are as follows:

$$\varepsilon_{xx} = \frac{\partial u_0}{\partial x} + z \cdot \frac{\partial \varphi_x}{\partial x} \tag{1.23}$$

$$\gamma_{xz} = \varphi_x + \frac{\partial w_0}{\partial x} \tag{1.24}$$

In the absence of in-plane forces ($u_0 = 0$), the constitutive equations of sandwich beam (similar to symmetric laminates) are given by:

$$\begin{Bmatrix} M_{xx} \\ M_{yy} \\ M_{xy} \end{Bmatrix} = \begin{bmatrix} D_{11} & D_{12} & D_{16} \\ D_{21} & D_{22} & D_{26} \\ D_{16} & D_{26} & D_{16} \end{bmatrix} \begin{Bmatrix} \frac{\partial \varphi_x}{\partial x} \\ \frac{\partial \varphi_y}{\partial y} \\ \frac{\partial \varphi_x}{\partial x} + \frac{\partial \varphi_y}{\partial y} \end{Bmatrix} \tag{1.25}$$

$$\begin{Bmatrix} Q_y \\ Q_x \end{Bmatrix} = K \begin{bmatrix} A_{44} & A_{45} \\ A_{45} & A_{55} \end{bmatrix} \begin{Bmatrix} \frac{\partial w_0}{\partial y} + \varphi_y \\ \frac{\partial w_0}{\partial x} + \varphi_x \end{Bmatrix} \tag{1.26}$$

The inverse form of relationships (1.25) and (1.26) can be written as:

$$\begin{Bmatrix} \frac{\partial \varphi_x}{\partial x} \\ \frac{\partial \varphi_y}{\partial y} \\ \frac{\partial \varphi_x}{\partial x} + \frac{\partial \varphi_y}{\partial y} \end{Bmatrix} = \begin{bmatrix} D_{11}^* & D_{12}^* & D_{16}^* \\ D_{12}^* & D_{22}^* & D_{26}^* \\ D_{16}^* & D_{26}^* & D_{66}^* \end{bmatrix} \begin{Bmatrix} M_{xx} \\ M_{yy} \\ M_{xy} \end{Bmatrix} \tag{1.27}$$

$$\begin{Bmatrix} \frac{\partial w_0}{\partial y} + \varphi_y \\ \frac{\partial w_0}{\partial x} + \varphi_x \end{Bmatrix} = \frac{1}{K} \begin{bmatrix} A_{44}^* & A_{45}^* \\ A_{45}^* & A_{55}^* \end{bmatrix} \begin{Bmatrix} Q_y \\ Q_x \end{Bmatrix} \tag{1.28}$$

where K is the shear correction coefficient, D_{ij}^* (i, j = 1, 2, 6) are the elements of the inverse of [D] matrix and A_{ij}^* (i, j = 4, 5) are the elements of the inverse of [A] matrix:

$$A_{44}^* = \frac{A_{55}}{A}\,;\; A_{55}^* = \frac{A_{44}}{A}\,;\; A_{45}^* = -\frac{A_{45}}{A}$$
$$A = A_{44}A_{55} - A_{45}A_{45} \tag{1.29}$$
$$A_{ij} = \sum_{k=1}^{N} \bar{Q}_{ij}^{(k)} (z_{k+1} - z_k)$$

$\bar{Q}_{ij}^{(k)}$ are the layer stifnesses and k is the number of layers.

Considering that $M_{yy} = M_{xy} = Q_y = \varphi_y = 0$, from the relationships (1.27) and (1.29) result:

$$\frac{\partial \varphi_x}{\partial x} = D_{11}^* M_{xx} \tag{1.30}$$

$$\frac{\partial w_0}{\partial x} + \varphi_x = \frac{A_{55}^*}{K} Q_x \tag{1.31}$$

or

$$E_{xx}^b I_{yy} \frac{\partial \varphi_x}{\partial x} = M(x) \tag{1.32}$$

$$KG_{xz}^b bh \left(\frac{\partial w_0}{\partial x} + \varphi_x \right) = Q(x) \tag{1.33}$$

where $(x) = b \cdot M_{xx}$, M_{xx} is given by equation (1.20); $Q(x) = b \cdot Q_x$; $E_{xx}^b = \frac{12}{D_{11}^* h^3}$;

$I_{yy} = \frac{bh^3}{12}$; $G_{xz}^b = \frac{1}{A_{55}^* h}$; $D_{11}^* = (D_{22}D_{66} - D_{26}D_{26})/D^*$; $D^* = D_{11}D_1 + D_{12}D_2 + D_{16}D_3$;

$D_1 = D_{22}D_{66} - D_{26}D_{26}$; $D_2 = D_{16}D_{26} - D_{12}D_{66}$; $D_3 = D_{12}D_{26} - D_{22}D_{16}$;

$D_{ij} = \frac{1}{3}\sum_{k=1}^{N} \bar{Q}_{ij}^{(k)} (z_{k+1}^3 - z_k^3)$.

By integrating the relationships (1.32) and (1.33) with respect to x and applying the boundary conditions, results the relationship of the bending deflection:

$$w(x) = \frac{b}{2E_{xx}^b I_{yy}} \left(\frac{P}{2} - \frac{2Pc}{\pi L} \right) \left[\frac{L^2}{4} x - \frac{x^3}{3} \right] + \frac{1}{KG_{xz}^b h} \left(\frac{P}{2} - \frac{2Pc}{\pi L} \right) x \tag{1.34}$$

1.2.3. Bending deflection of sandwich beam by Reddy third-order shear deformation theory (TSDT)

According to Reddy third-order shear deformation theory [23, 24], the displacement field of a beam loaded in three-point bending is given by the following relations:

$$u(x,z) = u_0(x) + z\varphi_x(x) - \frac{4}{3h^2}z^3\left(\varphi_x + \frac{\partial w_0}{\partial x}\right) \tag{1.35}$$

$$w(x,z) = w_0(x) \tag{1.36}$$

The nonlinear strains and strain-displacement relationships are as follows:

$$\begin{Bmatrix}\varepsilon_{xx}\\ \varepsilon_{yy}\\ \gamma_{xy}\end{Bmatrix} = \begin{Bmatrix}\varepsilon_{xx}^{(0)}\\ \varepsilon_{yy}^{(0)}\\ \gamma_{xy}^{(0)}\end{Bmatrix} + z\begin{Bmatrix}\varepsilon_{xx}^{(1)}\\ \varepsilon_{yy}^{(1)}\\ \gamma_{xy}^{(1)}\end{Bmatrix} + z^3\begin{Bmatrix}\varepsilon_{xx}^{(3)}\\ \varepsilon_{yy}^{(3)}\\ \gamma_{xy}^{(3)}\end{Bmatrix} \tag{1.37}$$

$$\begin{Bmatrix}\gamma_{yz}\\ \gamma_{xz}\end{Bmatrix} = \begin{Bmatrix}\gamma_{yz}^{(0)}\\ \gamma_{xz}^{(0)}\end{Bmatrix} + z^2\begin{Bmatrix}\gamma_{yz}^{(2)}\\ \gamma_{xz}^{(2)}\end{Bmatrix}$$

where:

$$\begin{Bmatrix}\varepsilon_{xx}^{(0)}\\ \varepsilon_{yy}^{(0)}\\ \gamma_{xy}^{(0)}\end{Bmatrix} = \begin{Bmatrix}\frac{\partial u_0}{\partial x} + \frac{1}{2}\left(\frac{\partial w_0}{\partial x}\right)^2\\ \frac{\partial v_0}{\partial y} + \frac{1}{2}\left(\frac{\partial w_0}{\partial y}\right)^2\\ \frac{\partial u_0}{\partial y} + \frac{\partial v_0}{\partial x} + \frac{\partial w_0}{\partial x}\cdot\frac{\partial w_0}{\partial y}\end{Bmatrix}$$

$$\begin{Bmatrix}\varepsilon_{xx}^{(1)}\\ \varepsilon_{yy}^{(1)}\\ \gamma_{xy}^{(1)}\end{Bmatrix} = \begin{Bmatrix}\frac{\partial \varphi_x}{\partial x}\\ \frac{\partial \varphi_y}{\partial y}\\ \frac{\partial \varphi_x}{\partial y} + \frac{\partial \varphi_y}{\partial x}\end{Bmatrix}; \begin{Bmatrix}\gamma_{yz}^{(0)}\\ \gamma_{xz}^{(0)}\end{Bmatrix} = \begin{Bmatrix}\varphi_y + \frac{\partial w_0}{\partial y}\\ \varphi_x + \frac{\partial w_0}{\partial x}\end{Bmatrix} \tag{1.38}$$

$$\begin{Bmatrix}\varepsilon_{xx}^{(3)}\\ \varepsilon_{yy}^{(3)}\\ \gamma_{xy}^{(3)}\end{Bmatrix} = -c_1\begin{Bmatrix}\frac{\partial \varphi_x}{\partial x} + \frac{\partial^2 w_0}{\partial x^2}\\ \frac{\partial \varphi_y}{\partial y} + \frac{\partial^2 w_0}{\partial y^2}\\ \frac{\partial \varphi_x}{\partial y} + \frac{\partial \varphi_y}{\partial x} + 2\frac{\partial^2 w_0}{\partial x \partial y}\end{Bmatrix}; c_1 = \frac{4}{3h^2}; c_2 = 3c_1.$$

Moreover, based on this theory the constitutive equations of stress resultants and strains, in the absence of in-plane forces, are given by:

$$\begin{Bmatrix}M_{xx}\\ M_{yy}\\ M_{xy}\end{Bmatrix} = [D]\begin{Bmatrix}\varepsilon_{xx}^{(1)}\\ \varepsilon_{yy}^{(1)}\\ \gamma_{xy}^{(1)}\end{Bmatrix} + [F]\begin{Bmatrix}\varepsilon_{xx}^{(3)}\\ \varepsilon_{yy}^{(3)}\\ \gamma_{xy}^{(3)}\end{Bmatrix} \tag{1.39.a}$$

$$D_{ij} = \frac{1}{3}\sum_{k=1}^{N}\bar{Q}_{ij}^{(k)}\left(z_{k+1}^3 - z_k^3\right); F_{ij} = \frac{1}{5}\sum_{k=1}^{N}\bar{Q}_{k+1}^{(k)}\left(z_{k+1}^5 - z_k^5\right); i,j = 1, 2, 6.$$

$$\begin{Bmatrix} Q_{yz} \\ Q_{xz} \end{Bmatrix} = [A] \begin{Bmatrix} \gamma_{yz}^{(0)} \\ \gamma_{xz}^{(0)} \end{Bmatrix} + [D] \begin{Bmatrix} \gamma_{yz}^{(2)} \\ \gamma_{xz}^{(2)} \end{Bmatrix} \quad (1.39.b)$$

$$A_{ij} = \sum_{k=1}^{N} \bar{Q}_{ij}^{(k)} (z_{k+1} - z_k) \; ; \; D_{ij} = \frac{1}{3} \sum_{k=1}^{N} \bar{Q}_{ij}^{(k)} (z_{k+1}^3 - z_k^3) \; ; \; i,j = 4, 5.$$

In the relationships (1.39.a and b) the parameters A_{ij}, D_{ij} and F_{ij} are the stiffness's matrix given in terms of the layer stiffnesses, $\bar{Q}_{ij}^{(k)}$, and the layer coordinates z_{k+1} and z_k.

In the relationship (1.39.a) the matrices [D] and [F] are of the order 3x3 instead in the relationship (1.39.b) the matrices [A] and [D] are of the order 2x2.

Assuming that $M_{yy} = M_{xy} = Q_{yz} = \phi_y = 0$, from the relationships (1.39.a and b) result:

$$M_{xx} = D_{11} \frac{\partial \varphi_x}{\partial x} - c_1 F_{11} \left(\frac{\partial \varphi_x}{\partial x} + \frac{\partial^2 w_0}{\partial x^2} \right) \quad (1.40)$$

$$Q_{xz} = A_{55} \left(\varphi_x + \frac{\partial w_0}{\partial x} \right) - c_2 D_{55} \left(\varphi_x + \frac{\partial w_0}{\partial x} \right) = (A_{55} - c_2 D_{55}) \left(\varphi_x + \frac{\partial w_0}{\partial x} \right) \quad (1.41)$$

Considering the bending moment from the equation (1.20) and the shear force as $Q_{xz} = \frac{P}{2} - \frac{2Pc}{\pi L}$, the relationships (1.40) and (1.41) become:

$$\left(\frac{P}{2} - \frac{2Pc}{\pi L} \right) x = D_{11} \frac{\partial \varphi_x}{\partial x} - c_1 F_{11} \left(\frac{\partial \varphi_x}{\partial x} + \frac{\partial^2 w_0}{\partial x^2} \right) \quad (1.41)$$

$$\frac{P}{2} - \frac{2Pc}{\pi L} = (A_{55} - c_2 D_{55}) \left(\varphi_x + \frac{\partial w_0}{\partial x} \right) \quad (1.42)$$

By integrating the relationship (1.41) with respect to x result:

$$\varphi_x(x) = \frac{1}{D_{11} - c_1 F_{11}} \left(\frac{P}{2} - \frac{2Pc}{\pi L} \right) \frac{x^2}{2} + \frac{c_1 F_{11}}{D_{11} - c_1 F_{11}} \cdot \frac{\partial w_0}{\partial x} + C_1 \quad (1.43)$$

where C_1 is integration constant.

Equation (1.43) is replaced in the relationship (1.42) resulting in:

$$\left(\frac{P}{2} - \frac{2Pc}{\pi L} \right) - \frac{A_{55} - c_2 D_{55}}{D_{11} - c_1 F_{11}} \left(\frac{P}{2} - \frac{2Pc}{\pi L} \right) \frac{x^2}{2} - (A_{55} - c_2 D_{55}) \cdot C_1 = S \cdot \frac{\partial w_0}{\partial x} \quad (1.44)$$

where $= \frac{(A_{55} - c_2 D_{55}) c_1 F_{11} + (D_{11} - c_1 F_{11}) \cdot (A_{55} - c_2 D_{55})}{D_{11} - c_1 F_{11}}$.

By integrating the relationship (1.44) with respect x results:

$$w_0(x) = \frac{1}{S} \left(\frac{P}{2} - \frac{2Pc}{\pi L} \right) x - \frac{1}{S} \cdot \frac{A_{55} - c_2 D_{55}}{D_{11} - c_1 F_{11}} \left(\frac{P}{2} - \frac{2Pc}{\pi L} \right) \cdot \frac{x^3}{3} - \frac{A_{55} - c_2 D_{55}}{S} \cdot C_1 \cdot x + C_2 \quad (1.45)$$

From bending theory are also known the boundary conditions as w_0 (0) = 0 and w_0 (L) = 0, which applied for equation (1.45) give the integration constants as:

$$C_1 = \left(\frac{1}{A_{55} - c_2 D_{55}} - \frac{L^2}{3(D_{11} - c_1 F_{11})} \right) \left(\frac{P}{2} - \frac{2Pc}{\pi L} \right) \quad (1.46.a)$$

$$C_2 = 0 \quad (1.46.b)$$

Considering the integration constants in the equation (1.45) results the bending deflection of sandwich beam according to TSDT and respectively considering the local effect given by the concentrated load through the parameter $c \in \left[-\frac{h}{2};\frac{h}{2}\right]$:

$$w(x) = \frac{1}{S}\left(\frac{P}{2} - \frac{2Pc}{\pi L}\right)\cdot x - \frac{1}{S}\cdot\frac{A_{55} - c_2 D_{55}}{D_{11} - c_1 F_{11}}\left(\frac{P}{2} - \frac{2Pc}{\pi L}\right)\cdot\frac{x^3}{3} - \\ -\frac{A_{55}-c_2 D_{55}}{S}\cdot\left(\frac{1}{A_{55}-c_2 D_{55}} - \frac{L^2}{3(D_{11}-c_1 F_{11})}\right)\left(\frac{P}{2} - \frac{2Pc}{\pi L}\right)\cdot x \qquad (1.47)$$

1.2.4. Numerical analysis of bending deflection of a sandwich beam loaded in three-point bending

For the numerical analysis of bending deflection it is considered a sandwich beam composed of aluminum faces with 1 mm thickness and polyurethane foam core with thickness of 5 mm. The total width of sandwich beam is 10 mm. The sandwich beam is loaded in three-point bending with span length of 122 mm. The numerical analysis is based on FEM simulation on a geometrical model of the sandwich beam and it was carried out with Abaqus CAE v6.10 software. The numerical model has been meshed in 54780 finite elements of C3D8 type with a total of 61456 nodes, and to define the materials of sandwich beam there have been used the mechanical properties from Table 1.5. In order, to determine the bending deflection a 2 mm vertical displacement on the loading support was imposed, fig. 1.31. The vertical reaction from the loading support and respectively the vertical displacement of the nodes corresponding to three values of the parameter c (the extreme point of the top face, the point from the middle of the section and respectively the extreme point of the bottom face) were followed during FEM analysis.

Table 1.5. Mechanical properties of the sandwich beam components

Material	**Young's modulus [MPa]**	**Poisson's ratio**
Aluminum	70000	0.3
Foam (ρ = 100 kg/m^3, ρ - density)	26.06 – 32.69	0.284

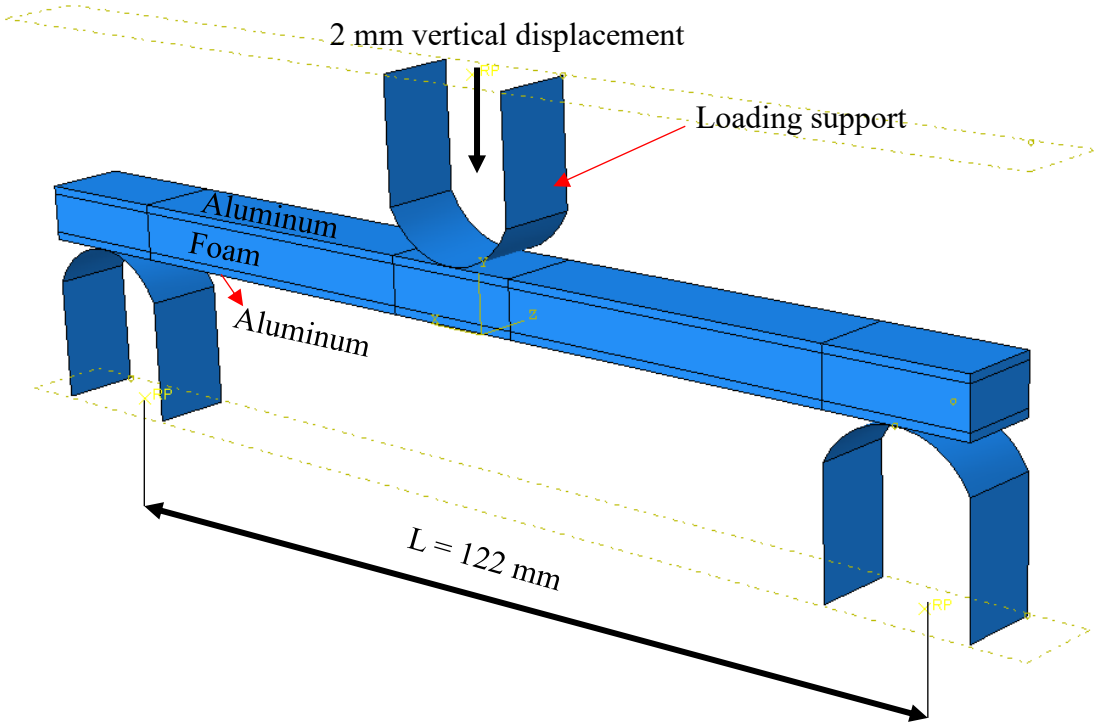

Fig. 1.31. The numerical model of sandwich beam loaded in three-point bending, [21]

1.2.5. Experimental analysis of bending deflection of a sandwich beam loaded in three-point bending

The experimental analysis of bending deflection was conducted on a sandwich beam composed of steel faces with 0.5 mm and polyurethane foam core with density of 40 kg/m^3 and a thickness of 26 mm. The beam width was 48.3 mm. The sandwich beam was loaded in three points bending with span length of 200 mm. The bending tests were performed on a tensile testing machine model Zwick/Roell of 5 kN. For the determination of bending deflection, a video camera placed in front of the testing machine was used, fig. 1.32, which recorded the deformation of the beam during the bending test.

By using the SigmaScan Pro v5 software [25], images were taken at different loading forces and after their calibration; the vertical displacement of different points in the cross section from mid span was measured. Images corresponding to different applied forces were compared with an image taken before loading the sample, fig. 1.33.a. Thus, the bending deflection was determined for different points in the middle section.

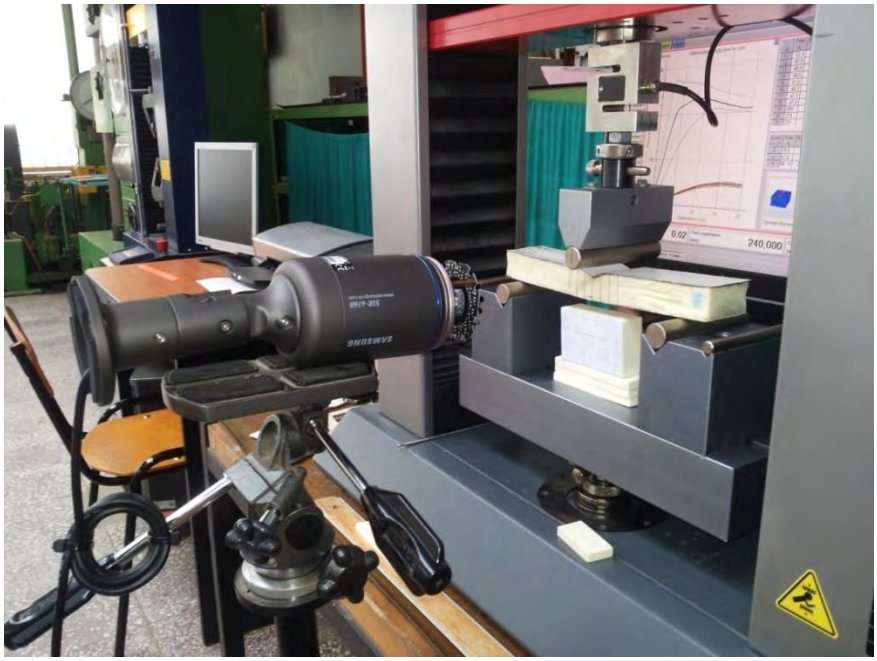

Fig. 1.32. The three-point bending tests of sandwich beam, [21]

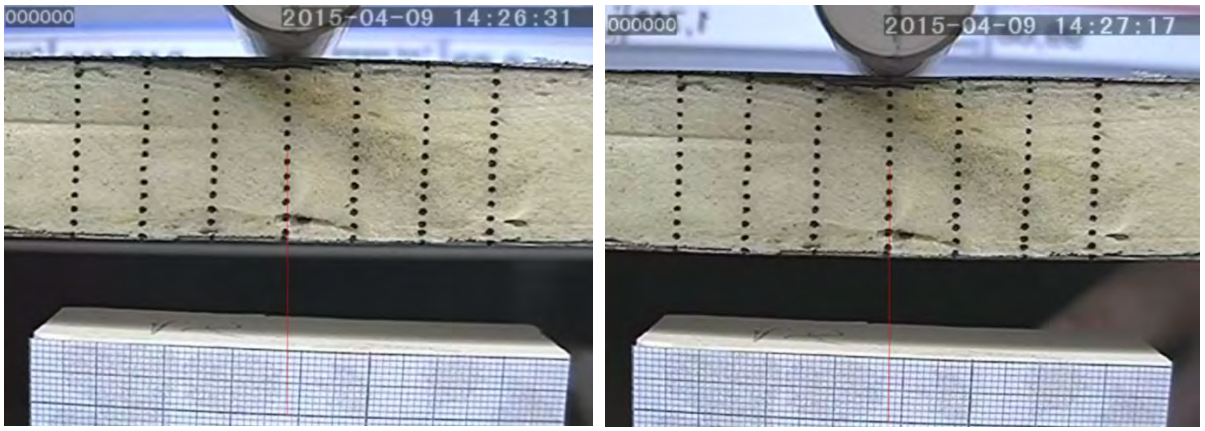

a) b)

Fig. 1.33. Images analyzed with SigmaScan Pro v5: a) before applying the force; b) beam loaded with 99.08 N, [21].

The numerical and experimental results related to bending deflection of sandwich beam loaded in three-point bending were compared with analytical results obtained by applying the relations (1.34) and (1.47). In the case of FEM analysis it was used higher density foam as core which confers a better stiffness of the sandwich beam. Thus, in this case the bending behavior of sandwich beam can be well predicted by the relationship (1.34), based on the first order shear deformation theory. Table 1.6 shows the numerical and analytical bending deflection determined for the model in Figure 1.31.

Table 1.6. The bending deflection of sandwich beam model from Figure 41

Sandwich beam	**Applied force, F = 14.63 N**				
	Bending deflection w [mm]				
		FSDT classic	**FSDT_corr Relationship (1.34)**	**TSDT_corr Relationship (1.47)**	**FEM**
Aluminum + Foam (ρ = 100 kg/m^3)	c = -3.5	-	0.461	1.231	0.498
	c = 0	0.445	0.445	1.188	0.493
	c = 3.5	-	0.428	1.145	0.489

The values for parameter *c* were chosen to determine the bending deflection on the extreme point of the top face (*c* = -3.5), the point from the middle of section (*c* = 0) and respectively in the extreme point of the bottom face (*c* = 3.5), fig. 1.34.

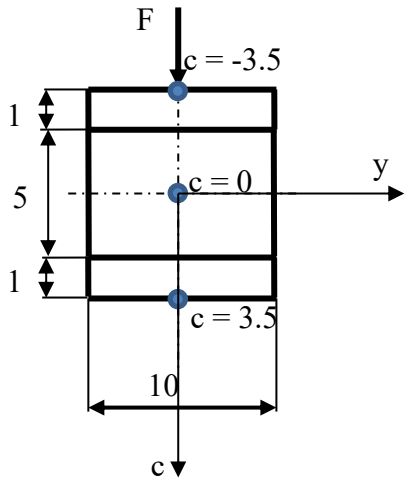

Fig. 1.34. The middle cross section of the sandwich beam with aluminum faces and foam core, [21]

In the case of sandwich beam with steel faces and low density foam core a better prediction of the bending deflection was observed based on the relationship (1.47), according to the third order shear deformation theory. Thus, in Table 1.7 are correlated the analytical values of bending deflection with experimental ones for sandwich beam loaded in three-point bending.

For analytical computations it was considered an elasticity modulus for low density foam of 20.1 MPa [26, 27] and a Poisson's ratio of 0.28.

In accordance with the cross-sectional dimensions, the values of parameter *c* were chosen to determine the bending deflection in the extreme point of the top face, in the mid-section and respectively in the extreme point of the bottom face, fig. 1.35.

The results showed a higher influence of the core flexibility (due to foam density) compared to face sheet, on the bending deflection of the sandwich beam.

Table 1.7. The bending deflection of sandwich beam with steel faces and low density foam core

Sandwich beam	**Applied force, F = 99.08 N**				
	Bending deflection w [mm]				
		FSDT classic	**FSDT_corr Relationship (1.34)**	**TSDT_corr Relationship (1.47)**	**Experimental**
Steel + Foam ($\rho = 40$ kg/m^3)	c = -13.5	-	0.565	1.327	1.566
	c = 0	0.52	0.52	1.222	1.193
	c = 13.5	-	0.476	1.117	1.118

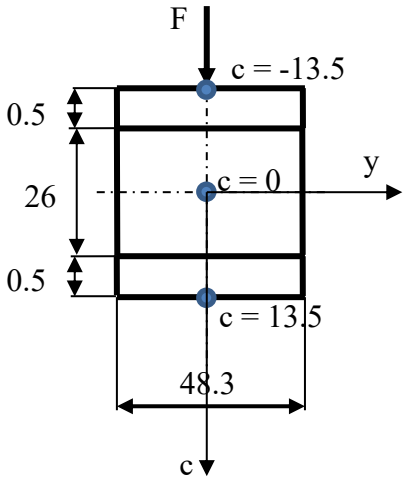

Fig. 1.35. The middle cross section of the sandwich beam with steel faces and low density foam core, [21]

The proposed relationships for determining the bending deflection are developed based on the principles and assumptions of classical bending theories, except that allow the evaluation of bending deflection at any point on the cross section. This has been possible by introducing the Timoshenko's hypothesis in the bending theories. According to this hypothesis, the concentrated force in a point can be equated with a radially distributed pressure around the point of application. Also, this hypothesis represents the local effect of the concentrated force being more visible in sandwich beams with flexible cores.

The bending deflection of sandwich beams was analyzed based on a correction to the first and third order shear deformation theories. The correction consists in the equivalence of applied concentrated force with a force that takes into account the local effect given by the applied load $P \equiv P - \frac{4Pc}{\pi L}$. This equivalence is based on assumption that a concentrated applied force P produces an effect on the material equal to $P - \frac{4Pc}{\pi L}$. Thus, the bending deflection of two sandwich configurations loaded in three-point bending was evaluated in terms of analytical, numerical and experimental approach. The results revealed that the proposed relationships are applicable for determining the vertical displacement of different points on the same cross-section. Also, it was noted that, for sandwich beams with low density foam core the TSDT has a better accuracy for determining the bending deflection.

It is obvious that the bending deflection differs on the cross section and the variation is higher as the core flexibility is greater. This shows the necessity of using these relations for a correct assessment of bending behavior of sandwich beams.

1.3. Research on fiber reinforced composites

Composite materials have become a class of materials indispensable for a range of industrial areas such as automotive, transportation, aeronautics, civil constructions, offshore applications, etc. The favourable strength or stiffness/weight ratio of composite materials make them a good choice in different engineering applications. One of the known vehicle manufacturers invests nearly 10 million pounds per year in the acquisition of carbon fibre reinforced polymers (CFRP) for electric and hybrid vehicles, and this is not the only example, [28]. The aircraft structures are made up of 50 to 70 percent composite materials, [29]. In the wind power energy, the production of wind turbine blades was expected to increase in 2017 to 6.21 million metric tons of structures with a budget of nearly $34 billion. Of this total, the CFRP components represent about 19% of the blade market's value, [30]. The widespread

use of composite materials is possible on the one hand due to the technological development but on the other hand it is due to the advanced research on the design and analysis of their mechanical behaviour.

One of the key points in the development of composite materials were the models proposed by Voigt [31, 32] and Reuss [33] used to evaluate the mechanical properties of unidirectional fibre reinforced polymers (UD FRP). The Voigt model is also known as the *rule of mixture* or the iso-strain model and is used to evaluate the Young's modulus of UD composite, along the fibre direction, E_{11}, and the Poisson's ratio, ν_{12}. The Reuss model is also known as the *inverse rule of mixture* or the iso-stress model, and is used to evaluate the transverse Young's modulus of UD composite, E_{22}, and the in-plane shear modulus, G_{12}. The two reference models are developed based on hypotheses such as no voids can exist in the fibres or matrix or between them and the bonds between the fibres and the matrix are perfect.

In reality, these two assumptions can be easily violated and therefore the results evaluated based on these models are significantly different from the experiments. Given these facts, several models have been proposed to improve the predictions of elastic properties of UD composites. Halpin and Tsai, [34], derived the Hill's generalized model into a simpler analytical form suitable for a wide variety of reinforcement geometries. Chamis [35], also, based on the mechanical principles applied in micromechanics of composites proposed equations for transverse elasticity modulus and in-plane shear modulus. Instead, the rule of mixture is considered for longitudinal elasticity modulus and Poisson's ratio. Another category of models is based on the variational energy principles of the elasticity theory. In these models, equations are developed to estimate the elastic properties of a UD composite by considering a representative volume element (RVE) which contains a particle with different geometry, embedded in the matrix, [36, 37]. However, the models listed are not straightforward to use, they involve a number of geometric and fiber layout parameters which are not easy to quantify. In addition to elastic properties, the micromechanics theory of composite materials also deals with the estimation of the ultimate strength. In this sense, perhaps one of the most known equations is proposed by Kelly and Davies, [38, 39]. In this equation it is considered that the fibres have equal strength and respectively they are more brittle and cannot elongate as much as the matrix:

$$\sigma_c = \sigma_f \cdot V_f + (\sigma_m)_{\varepsilon_{f,m}} \cdot V_m \tag{1.48}$$

where σ_f is the ultimate strength of the fibers, $(\sigma_m)_{\varepsilon_{f,m}}$ is the matrix strength at the failure strain of the fibres and V_f, V_m are the fibres and matrix volume fractions.

In the inverse situation where the matrix is more brittle than the fibres, the ultimate strength of the composite is given by the rule of mixture:

$$\sigma_c = \sigma_f \cdot V_f + \sigma_m \cdot V_m \tag{1.49}$$

where σ_m is the ultimate strength of the matrix.

Karam, [40], and Lee and Hwang, [41], proposed a modification of the rule of mixture based on the effective fibre volume fraction to estimate the ultimate tensile strength of unidirectional fibre reinforced composites.

Besides the elasticity modulus and ultimate strength, equally important is the mechanical behaviour of the material up to the failure point. The stress-strain curve and respectively the ultimate strain, can give significant information on the material's ability to absorb strain energy. Most of fibre reinforced composite materials exhibit non-linear stress-strain behaviour in all of the principal directions. Hashin et all, [42], performed a non-linear analysis of fibre reinforced composite laminates based on the non-linear characteristics of unidirectional lamina. The analysis used a Ramberg-Osgood representation of the lamina's transverse and shear stress-strain curves in conjunction with deformation theory. Jones and Morgan, [43], have extended the Jones-Nelson strain energy based nonlinear mechanical property model in order to treat all nonlinearities of fibre reinforced composites. Nahas, [44], after a review of the existing methods for analysis of the response of laminated fibre reinforced composites formed by laminae exhibiting non-linear behaviour, proposed a new method. Considering that all lamina stress-strain curves are allowed to have non-linearity, the method uses an iterative procedure based on the secant modulus concept to predict the non-linear behaviour of the laminate. Recently, Sabik, [45], proposed the so-called first and second laws stress-strain relations to determine the non-linear in-plane shear response of composites. The composite layer is treated as a homogenized medium and the material is assumed to be non-linear elastic with degradation. A well-known model for mechanical behaviour prediction of composite materials is the Ladeveze's model, [46]. Based on continuum damage mechanics theory, Ladeveze and Le Dantec propose a model which incorporates the main internal damage modes of a laminate composite: matrix microcracking, fibre/matrix debonding and fibre fracture.

All of the above mentioned studies involve curve-fitting parameters which require an experimental data set.

This research study describes an experimental methodology for identifying the parameters of the Ladeveze's model.

According to this model, the damage of an elementary ply is described by the following equation:

$$E_D = \frac{1}{2}\left[\frac{\sigma_{11}^2}{E_1^0(1-d_{11})} - \frac{2\nu_{11}^0}{E_1^0}\sigma_{11}\sigma_{22} + \frac{\langle\sigma_{22}\rangle_+^2}{E_2^0(1-d_{22})} + \frac{\langle\sigma_{22}\rangle_-^2}{E_2^0} + \frac{\sigma_{12}^2}{2G_{12}^0(1-d_{12})}\right] \quad (1.50)$$

where E_D is the damaged-material strain energy, d_{ij} are scalar-damage variables which are constant through the ply thickness, E_i^0 and G_{ij}^0 are the initial Young's modulus and shear modulus, σ_{ij} are the stress components, ν_{ij} is the Poisson's ratio.

Increasing the d_{ij} parameters will result in a decrease of the elasticity modulus giving the following strain-stress relationship of a damaged ply:

$$\begin{Bmatrix}\varepsilon_{11}\\ \varepsilon_{22}\\ \gamma_{12}\end{Bmatrix} = \begin{bmatrix}\frac{1}{E_1^0(1-d_{11})} & -\frac{\nu_{12}}{E_1^0} & 0\\ -\frac{\nu_{12}}{E_1^0} & \frac{1}{E_2^0(1-d_{22})} & 0\\ 0 & 0 & \frac{1}{G_{12}^0(1-d_{12})}\end{bmatrix}\begin{Bmatrix}\sigma_{11}\\ \sigma_{22}\\ \sigma_{12}\end{Bmatrix} \quad (1.51)$$

By deriving the strain energy with respect to d_{ij} will result the thermodynamics forces Y_{ij} that drive the damage accumulation within the ply. Thus:

$$Y_{11} = \frac{\sigma_{11}^2}{2(1-d_{11})^2E_1^0}\,;\; Y_{22} = \frac{\langle\sigma_{22}\rangle_+^2}{2(1-d_{22})^2E_2^0}\,;\; Y_{12} = \frac{\sigma_{12}^2}{2(1-d_{12})^2G_{12}^0} \quad (1.52)$$

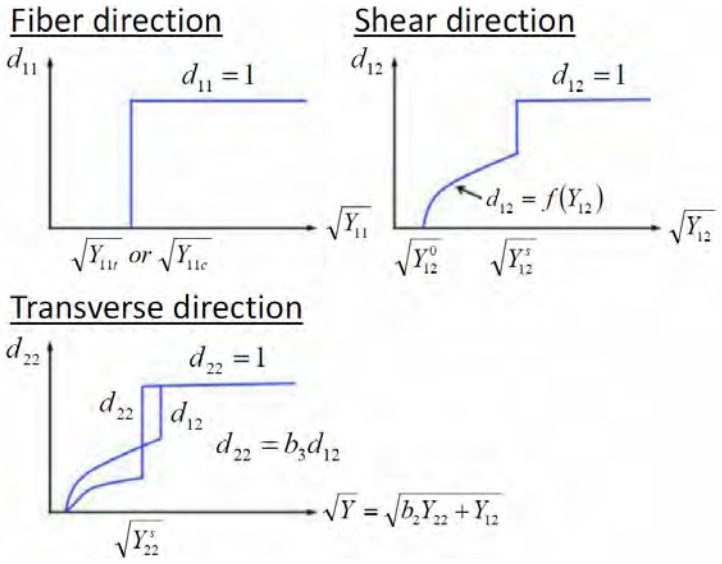

Fig. 1.36. The relationships between damage parameters and thermodynamic forces, [47]

Figure 1.36 shows the relationship between the damage parameters, d_{ij}, and the thermodynamic forces, Y_{ij}, of fibre-reinforced composites. The damage parameter d_{11} reflects the brittle nature of fibre-dominated fractures in the fibre direction. This parameter is 0 in the initial stage and becomes 1 as soon as the fibres breaks. The transverse and shear damages

exhibit progressive evolution; d_{22} and d_{12} are represented as a linear equation, polynomial form or other expressions of the thermodynamic forces. In general, transverse and shear stresses induce matrix damages and fibre/matrix interfacial damages, which results in transverse and shear modulus reduction. Thus, the transverse and shear components of thermodynamic force and damage parameters should be coupled, [47]. The coupling effect is defined by the following relationships:

$$Y = b_2 Y_{22} + Y_{12} \tag{1.53}$$

$$d_{22} = b_3 d_{12} \tag{1.54}$$

where Y is an equivalent thermodynamic force.

Ladeveze and Le Dantec proposed to use $[0/90]_S$, $[45/-45]_S$ and $[67.5/-67.5]_S$ laminates to identify the elastic, non-linear and damage parameters. In addition, tensile, compression and cyclic tests on UD FRC needs to be completed, in order to determine the mechanical properties. The overall longitudinal stress, σ_L, and respectively the longitudinal and transverse strains, ε_L and ε_T, are obtained from the monotonic and cyclic tensile tests, fig. 1.37.

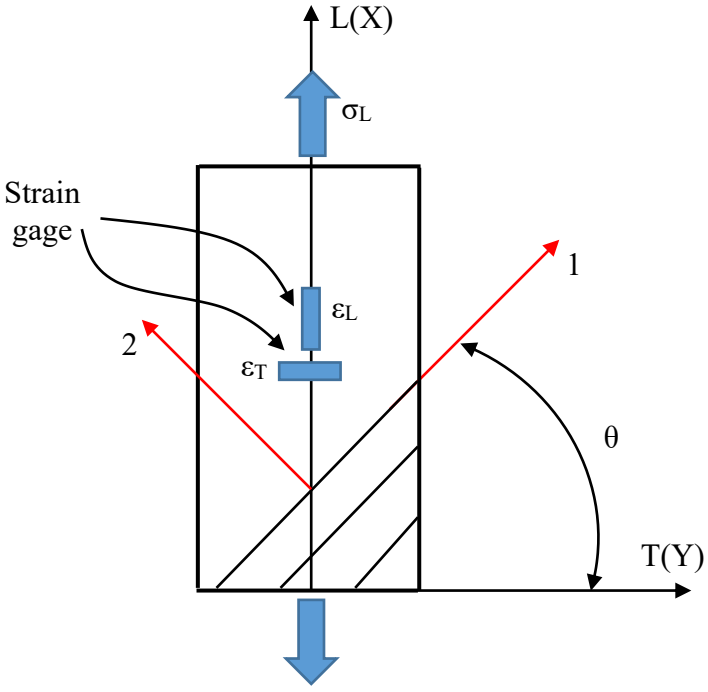

Fig. 1.37. The global stress and strains from tensile loading of an FRC laminate

However, the damage parameters are defined based on the local stresses and therefore the global to local transformation equations must be considered.

The in-plane constitutive equation of an undamaged unidirectional ply is given by:

$$\begin{Bmatrix}\sigma_{11}\\ \sigma_{22}\\ \sigma_{12}\end{Bmatrix}=\begin{bmatrix}Q_{11} & Q_{12} & 0\\ Q_{12} & Q_{22} & 0\\ 0 & 0 & Q_{66}\end{bmatrix}\begin{Bmatrix}\varepsilon_{11}\\ \varepsilon_{22}\\ \gamma_{12}\end{Bmatrix} \tag{1.55}$$

In the case of $[0/90]_S$ laminate in tension, the local stress and strain of 0 – degree ply can be expressed in terms of global stress and strain by:

$$\sigma_{11}=\frac{2Q_{11}(Q_{11}+Q_{22})-4Q_{12}^2}{(Q_{11}+Q_{22})^2-4Q_{12}^2}\cdot\sigma_L \quad ; \quad \varepsilon_{11}=\varepsilon_L \tag{1.56}$$

For the angle-ply laminates, $[\theta/-\theta]_S$, under uniaxial tensile loading, the local transverse and shear stresses/strains in each ply are calculated by:

$$\sigma_{22}=\frac{\bar{Q}_{YY}(Q_{12}cos^2\theta+Q_{22}sin^2\theta)-\bar{Q}_{XY}(Q_{12}sin^2\theta+Q_{22}cos^2\theta)}{\bar{Q}_{XX}\bar{Q}_{YY}-\bar{Q}_{XY}^2}\cdot\sigma_L \tag{1.57}$$

$$\varepsilon_{22}=\varepsilon_L sin^2\theta+\varepsilon_T cos^2\theta \tag{1.58}$$

$$\sigma_{12}=\frac{2Q_{66}(\bar{Q}_{XY}+\bar{Q}_{YY})\cos\theta\sin\theta}{\bar{Q}_{XX}\bar{Q}_{YY}-\bar{Q}_{XY}^2}\cdot\sigma_L \tag{1.59}$$

$$\gamma_{12}=2(\varepsilon_L-\varepsilon_T)\cos\theta\sin\theta \tag{1.60}$$

and

$$\bar{Q}_{XX}=Q_{11}cos^4\theta+2(Q_{12}+2Q_{66})cos^2\theta\,sin^2\theta+Q_{22}sin^4\theta \tag{1.61}$$

$$\bar{Q}_{XY}=(Q_{11}+Q_{22}-4Q_{66})cos^2\theta\,sin^2\theta+Q_{12}(cos^4\theta+sin^4\theta) \tag{1.62}$$

$$\bar{Q}_{YY}=Q_{11}sin^4\theta+2(Q_{12}+2Q_{66})cos^2\theta\,sin^2\theta+Q_{22}cos^4\theta \tag{1.63}$$

$$Q_{11}+Q_{22}=\frac{2\Delta\sigma_L\varepsilon_L}{\Delta\varepsilon_L^2-\Delta\varepsilon_T^2} \tag{1.64}$$

$$Q_{12}=\frac{-\Delta\sigma_L\Delta\varepsilon_T}{\Delta\varepsilon_L^2-\Delta\varepsilon_T^2} \tag{1.65}$$

$$Q_{11}=\frac{\Delta\sigma_L\Delta\varepsilon_L-\left[(Q_{11}+Q_{22})sin^4\theta+2Q_{12}cos^2\theta sin^2\theta+4Q_{66}cos^2\theta sin^2\theta\right]\varepsilon_L^2}{[cos^4\theta-sin^4\theta]\cdot[\Delta\varepsilon_L^2+\Delta\varepsilon_T^2]}-$$
$$-\frac{\left[(Q_{11}+Q_{22})cos^4\theta+2Q_{12}cos^2\theta sin^2\theta+4Q_{66}cos^2\theta sin^2\theta\right]\varepsilon_T^2}{[cos^4\theta-sin^4\theta]\cdot[\Delta\varepsilon_L^2+\Delta\varepsilon_T^2]} \tag{1.66}$$

$$Q_{66}=G_{12} \tag{1.67}$$

where $\Delta\sigma_L$ and $\Delta\sigma_T$ correspond to a range $\Delta\varepsilon_L$ between 0.1% and 0.3%, as recommended in the ASTM D3039 standard, [48].

In the case of $[45/-45]_S$ laminate, the following equations are derived for shear stress-strain relationship:

$$\sigma_{12}=\frac{1}{2}\sigma_L \tag{1.68}$$

$$\gamma_{12}=\varepsilon_L-\varepsilon_T \tag{1.69}$$

A carbon fibre composite material with 60 % fibre volume fraction is used in this study to determine the Ladeveze's damage parameters. The material is a Pyrofil^{TM} PAN based carbon

fibre prepreg laminate with epoxy matrix. This material has very good mechanical properties and is successfully used in various applications in the automotive industry. The mechanical properties of the raw materials of this composite are given in Table 1.8.

Table 1.8. The mechanical properties of the two constituents of composite material

Materials	**Density [g/cm^3]**	**Volume fraction [-]**	**Elasticity modulus, [MPa]**	**Ultimate tensile strength, [MPa]**
Pyrofil #360 modified epoxy resin	1.2	0.4	3000	32
Pyrofil^{TM}Pan carbon fiber, 15k	1.82	0.6	240000	4900

An extensive experimental program was conducted in this study, including both monotonic tensile and compression tests and respectively cyclic tests. According to Ladeveze, the cyclic tests should not exceed 5 cycles of loading up to a certain level, unloading to zero and reloading to a higher level. The test program is detailed in Table 1.9.

For the compression tests, a specially designed fixture was used, which allows compression by shear loading, fig. 1.38. Also, in all tests for strain measurements, both mechanical extensometer and DIC system, a Correlated Solutions product, were used.

Figure 1.39 – 1.42 are the stress – strain curves for the analyzed composite material, according to the testing program. Except for the $[45/-45]_S$ configuration, both tensile and compression tests shows a predominantly linear behavior of the material up to the failure.

Conversely, the $[45/-45]_S$ configuration shows a strong non-linear character in monotonic tests, indicating a gradual matrix damage as the in-plane shear stress increases.

In addition, in the cyclic tests of the two tested configurations a stiffness reduction is observed according to the assumptions considered by Ladeveze.

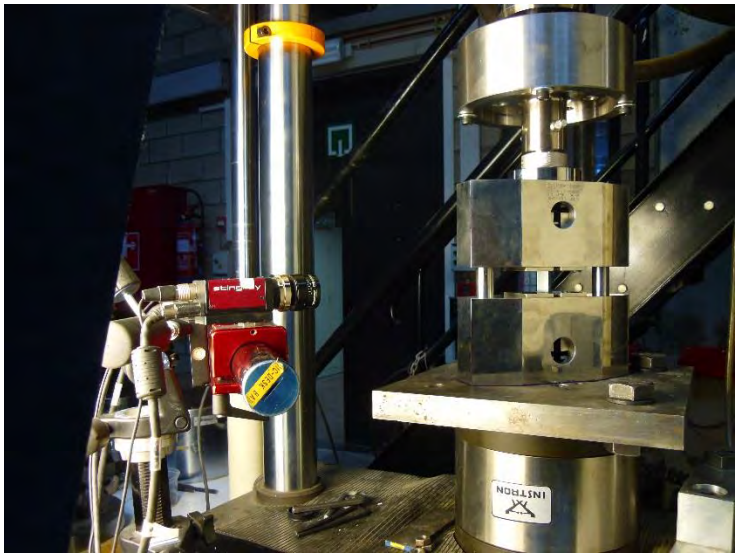

a)

b)

c)

Fig. 1.38. Compression test by shear loading: a) the loading fixture according to ASTM D3410; b) the loading scheme; c) tested specimen

Table 1.9. The test program of composite material

Tests	**Composite material configuration**			
	[0]	**[90]**	**[0/90]s**	**[45/-45]s**
Tensile ASTM D3039 ASTM D3518 8 plies laminate	Yes	Yes	Yes	Yes
Compression ASTM D3410 24 plies laminate	-	Yes	Yes	Yes
Cyclic tensile 8 plies laminate	-	Yes		Yes
Cyclic compression 24 plies laminate	-	Yes		Yes

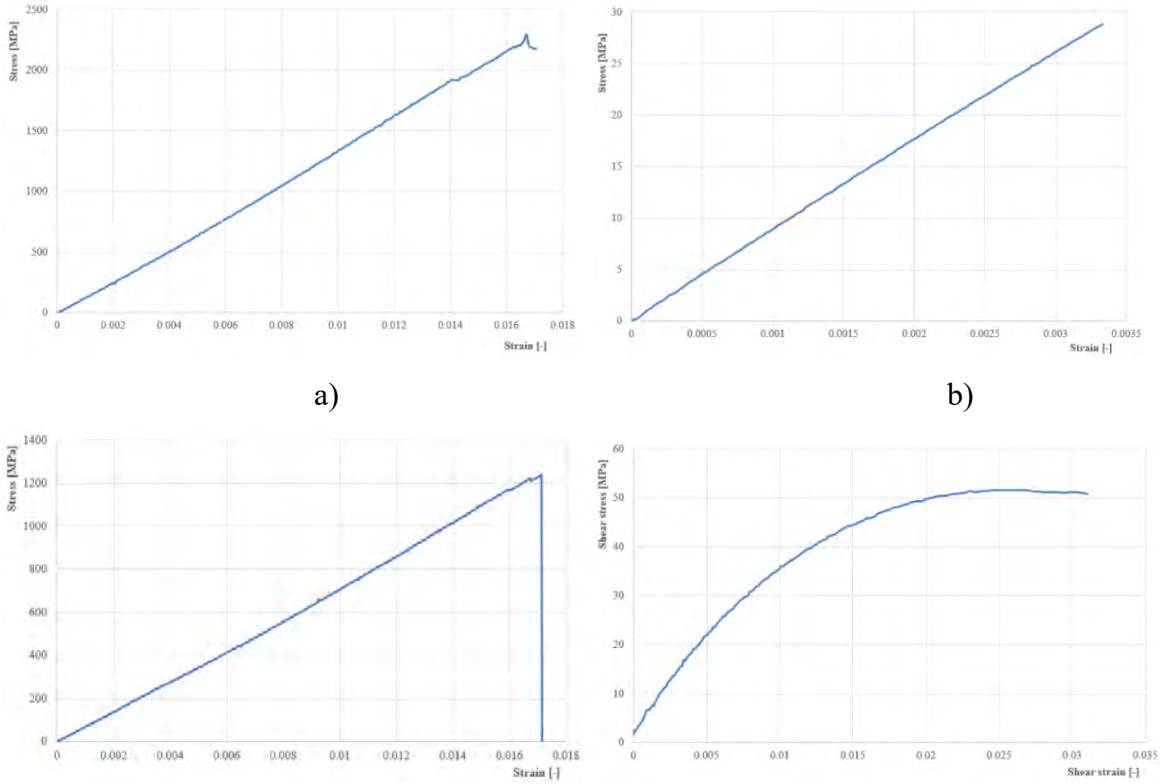

Fig. 1.39. The stress – strain curves from tensile tests: a) [0]; b) [90]; c) $[0/90]_S$; d) $[45/-45]_S$

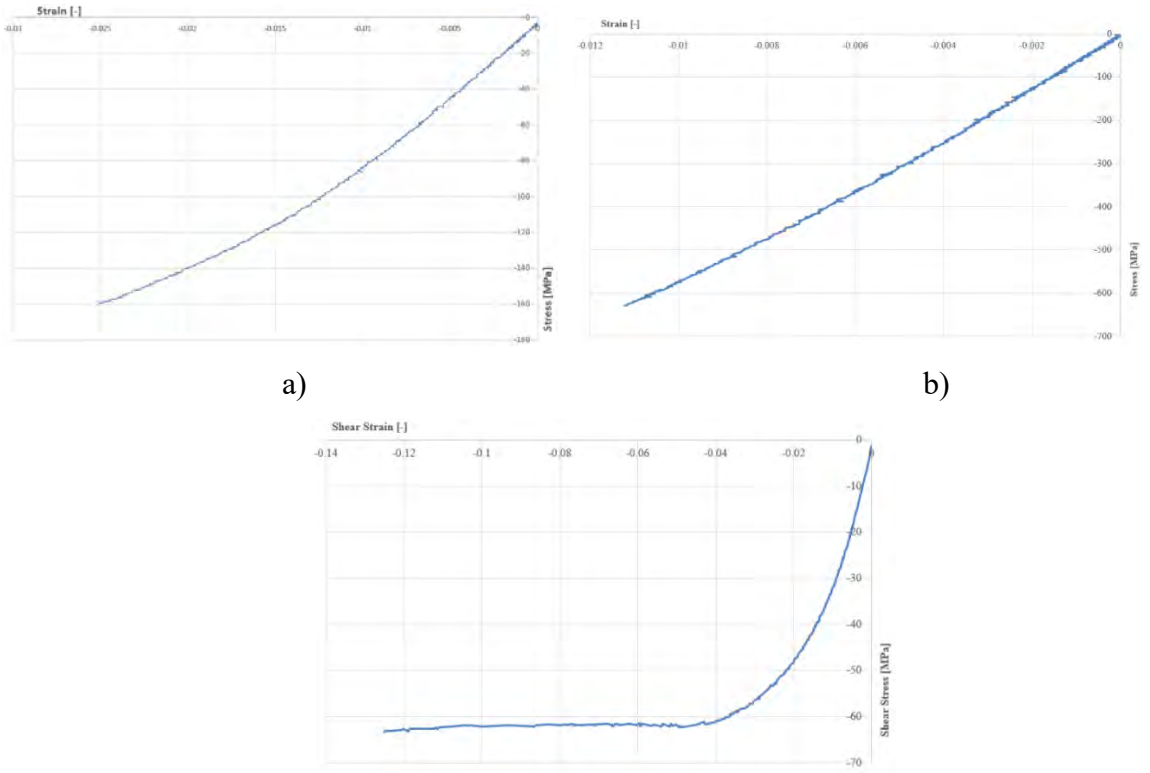

Fig. 1.40. The stress – strain curves from compression tests: a) [90]; b) $[0/90]_S$; c) $[45/-45]_S$

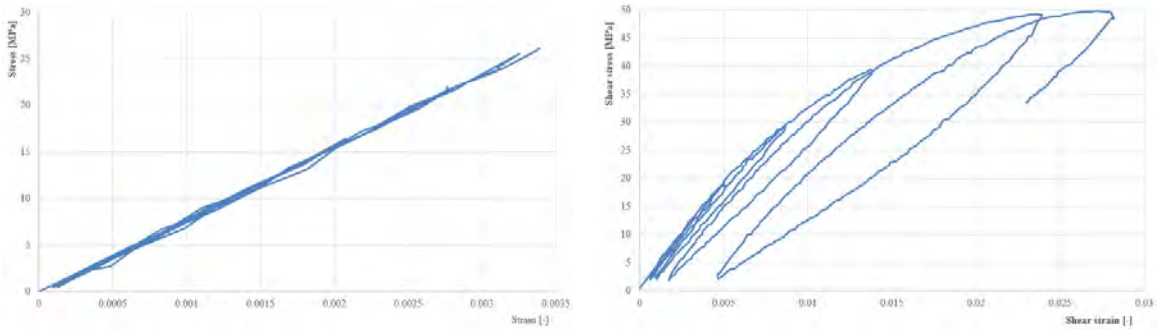

a) b)

Fig. 1.41. The stress – strain curves from cyclic tensile tests: a) [90]; b) $[45/-45]_S$

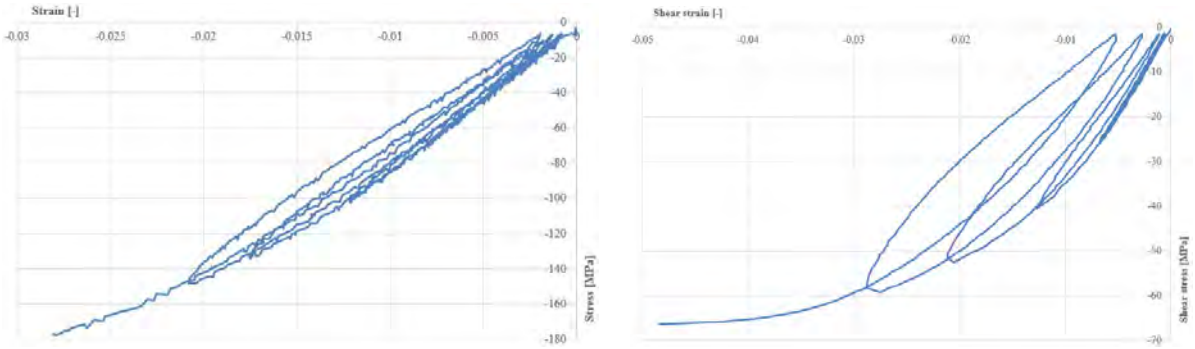

a) b)

Fig. 1.42. The stress – strain curves from cyclic compression tests: a) [90]; b) $[45/-45]_S$

Based on the stress – strain curves, the mechanical properties of the composite material, summarized in Tables 1.10 and 1.11, were determined.

Applying the relationships (1.52) for each loading level of the cyclic tests, the variation curves between the damage parameters and the thermodynamic forces were determined, figs. 1.43 and 1.44. The relationship between these parameters can be expressed by a 2-order polynomial function and highlights two limits. On the one hand, it is the threshold value of the thermodynamic force, Y^s, that is obtained by intersecting the damage evolution curve with the horizontal axis. On the other hand, it is the critical value of the thermodynamic force, Y^c, which can be defined as the maximum value of Y. The threshold and critical values of the thermodynamic forces are given in Table 1.12.

Table 1.10. The mechanical properties of analysed FRC material

Loading	**Mechanical properties**	**Composite material configuration**		
		[0]	**[90]**	**[45/-45]s**
Tensile	E_{11} [MPa]	127520	-	-
	E_{22} [MPa]	-	8680	-
	G_{12} [MPa]	-	-	4110
	$\sigma_{11,ult}$ [MPa]	2272.4	-	-
	$\sigma_{22,ult}$ [MPa]	-	30.6	-
	$\tau_{12,ult}$ [MPa]	-	-	52.2
Compression	E_{11} [MPa]	-	-	-
	E_{22} [MPa]	-	7985	-
	G_{12} [MPa]	-	-	3367
	$\sigma_{11,ult}$ [MPa]	-	-	-
	$\sigma_{22,ult}$ [MPa]	-	156	-
	$\tau_{12,ult}$ [MPa]	-	-	65.4

Table 1.11. The in-plane stiffness properties from $[0/90]_s$ tests

Loading	**Mechanical properties**	**Composite material configuration**
		[0/90]s
Tensile	Q_{11} [MPa]	70029.67
	Q_{22} [MPa]	70214.18
	Q_{12} [MPa]	-70121.9
	Q_{66} [MPa]	4110
	σ_{ult} [MPa]	1245.3
Compression	Q_{11} [MPa]	64643.99
	Q_{22} [MPa]	64961.74
	Q_{12} [MPa]	-64802.9
	Q_{66} [MPa]	3367
	σ_{ult} [MPa]	668.14

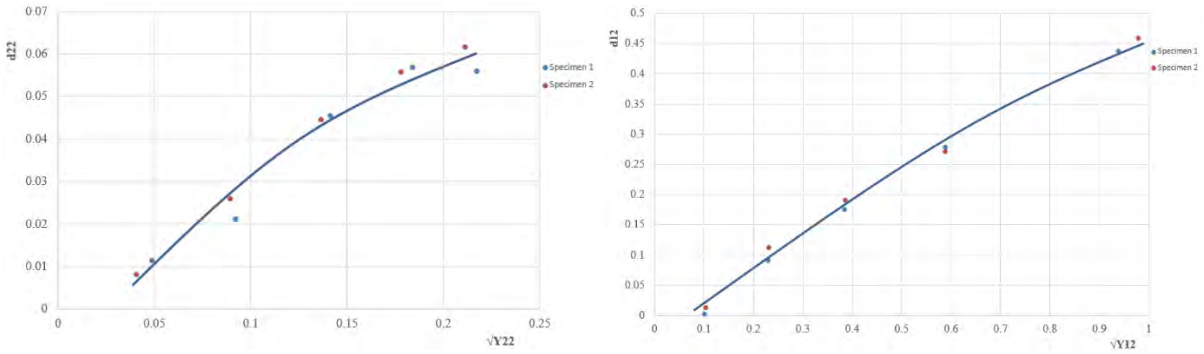

a) b)

Fig. 1.43. The damage evolution curves from cyclic tensile loading: a) [90]; b) $[45/-45]_S$

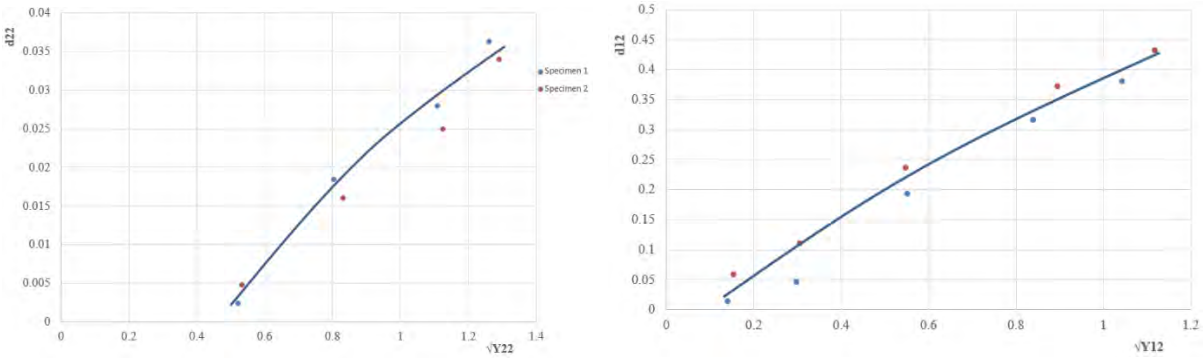

a) b)

Fig. 1.44. The damage evolution curves from cyclic compression loading: a) [90]; b) $[45/-45]_S$

For different stacking sequence, the coupling coefficients b_2 and b_3 from the equations (1.53) and (1.54) must be determined. Cyclic tests on $[45/-45]_S$ and $[67.5/-67.5]_S$ are used to identify the coupling coefficient between the thermodynamic forces. The d_{12} parameter is plotted with respect to Y for the tests on $[45/-45]_S$ and $[67.5/-67.5]_S$. b_2 is changed until the error between the two curves is minimized. The parameter b_3 is the linear coupling between d_{12} and d_{22}.

Based on the matrix microcracking and fibre/matrix debonding mechanisms, the Ladeveze model can be used for damage prediction of any unidirectional fibre laminated composite.

Table 1.12. The damage evolution parameters for the analysed FRC material

Loading	Material configuration	Parameters	Values
Cyclic tensile	[90]	Damage equation	$d_{22} = -0.8996(\sqrt{Y_{22}})^2 + 0.5399(\sqrt{Y_{22}}) - 0.0141$
		$\sqrt{Y_{22}^s}$	0.0273
		$\sqrt{Y_{22}^c}$	0.217
	$[45/-45]_S$	Damage equation	$d_{12} = -0.1331(\sqrt{Y_{12}})^2 + 0.6446(\sqrt{Y_{12}}) - 0.00496$
		$\sqrt{Y_{12}^s}$	0.372
		$\sqrt{Y_{12}^c}$	0.978
Cyclic compression	[90]	Damage equation	$d_{22} = -0.0044(\sqrt{Y_{22}})^2 + 0.0482(\sqrt{Y_{22}}) - 0.0202$
		$\sqrt{Y_{22}^s}$	0.436
		$\sqrt{Y_{22}^c}$	1.29
	$[45/-45]_S$	Damage equation	$d_{12} = -0.0725(\sqrt{Y_{12}})^2 + 0.5056(\sqrt{Y_{12}}) - 0.0478$
		$\sqrt{Y_{12}^s}$	0.0958
		$\sqrt{Y_{12}^c}$	1.118

2. Research on metallic materials and structures

2.1. Research on cylindrical cell honeycomb core structure

Sandwich structures have excellent mechanical properties, such as weight to stiffness and respectively weight to strength ratios. Therefore, the topic has been extensively studied in scientific research. In this study, a sandwich structure with cylindrical cell honeycomb core is proposed and analysed in terms of mechanical behaviour and properties, [49]. Typically, the sandwich panels are loaded by spatially varying transverse loads, and consequently the core of the panel must possess adequate compressive, shear stiffness and strength. The properties of the core are sensitive to both material choice and topology. There has been a significant activity in creation, manufacturing and testing of new topologies, starting with foam and honeycomb cores and continuing with structures as: metallic truss cores and all-metal sandwich panels.

Cellular materials offer low densities and are efficient in absorbing energy from external loading. In the past decade, major advances were made in the design of cellular materials with periodic topologies by exploiting minimum weight design, novel material fabrication processes, quasi-static and dynamic experiments, and large-scale simulations. Honeycombs usually comprise hexagonal or square cells, with the prismatic direction normal to the plane of face plates of the sandwich panel. Hexagonal honeycombs are routinely employed as the cores for lightweight sandwich panels and as energy absorbers; they are typically manufactured from aluminium alloys and have a relative density $\bar{\rho}$ (ratio of the density of the honeycomb treated as a homogeneous continuum to the density of the solid) of less than 3%. Experiments and simple analyses have shown that their out-of-plane elastic properties scale linearly with their relative density $\bar{\rho}$, [50]. In out-of-plane crushing, these honeycombs exhibit a stress peak followed by large stress oscillations associated with the formation of successive plastic folds within each cell. The out-of-plane shear strength is governed by cell wall buckling as discussed by Zhang and Ashby, [51]. Once the wrinkles have formed, the shear stress drops and subsequently remains approximately constant until failure occurs by the fracture of the cell walls. Square honeycomb cores having a high relative density ($\bar{\rho}$ > 0:05) are preferable over hexagonal honeycombs for high loadings such as blast and shock loads because of their high out-of-plane crushing resistance, shear resistance and in-plane

stretching strength, [52]. Circular cell honeycombs have also been studied analytically and experimentally by J. Chung and Waas, [53 – 56], for uniaxial and biaxial compressive in-plane loads. They observed an orthotropic behaviour of these structures and developed analytical solutions for the in-plane elastic properties. It was found that the elastic properties are dependent on the cell size and respectively thickness and ellipticity of the cell walls. In Ref. [57] it was shown that cell ellipticity and cell-wall-thickness variation are highly influential in affecting the macroscopic in-plane elastic properties of honeycomb. Perfectly circular cell honeycombs are transversally isotropic. The studies on these structures have been continued in Refs. [58, 59], by presenting analytical models for in-plane elastic moduli, Poisson's ratios, brittle crushing strengths and plastic yielding strengths. In all these studies, superior mechanical properties of circular cell honeycomb core structures compared to the hexagonal cell have been reported. Metallic truss cores with tetragonal topology were theoretically studied by Wicks and Hutchinson [62, 63]. This work demonstrated that such cores possess an excellent combination of compressive strength and low weight. Experimental measurements and numerical simulations were also performed on the tetragonal and triangular truss cores as well as truss-cored sandwich panels in [60, 61, 64 and 70]. Whereas these truss cores were studied thoroughly by theoretical and numerical means, the experiments are limited due to the manufacturing process.

Another category of structures in continuous development is represented by all-metall sandwich structures, which are widespread in various industrial fields, such as marine, mechanical and civil engineering industry. Analytical, numerical and empirical methods have been used to determine the stiffness properties of various metallic sandwich structures. Using the stiffness expressions from [71, 72] in Ref. [73], small deflection theory was used to obtain prediction for the deflection, stress and strain fields in all-steel sandwich panels with a spot-welded corrugated core. Concentrating the efforts on different core configurations, in Refs. [74, 75] the unit-load method was applied to derive closed form expressions for the transverse shear stiffness of sandwich panels with C and Z-type stiffeners. Based on this works, later studies have focused on the analysis and optimization of the web-core sandwich panel [77, 78]. In addition to the previous studies, this study proposes a cylindrical cell honeycomb core structure that can be considered as an alternative to the existing ones. In the first part of this study, the core structure is analysed in terms of manufacturing and the mechanical properties are analytically derived for in- and out-of-plane. The analytical derivations are validated by Finite Element analyses. In the second part of the paper the bending response of a sandwich beam is analysed using Finite Element Method.

2.1.1. The cylindrical cell honeycomb structure

2.1.1.1. Design and manufacture

The cylindrical cell honeycomb core structure is defined by four parameters: the mean radius of the cell, *R*; the mean connection radius between cells, *r*; the thickness of the wall cell, *t*, and the material modulus of elasticity, E_m. In Fig. 2.1.*a* and *b* the structure with two different stacking sequences is presented. Both variants can be achieved by the same manufacturing procedure, where a half-cell is obtained by plastic deformation process of a strip of the base material. Joining the two halves of the cells with laser welding or adhesives make the core material, Fig. 2.1.*c*. The core can be connected then to the faceplates by laser-welding or adhesion.

The relative density of such a structure is given by:

$$\frac{\rho*}{\rho_S} = \frac{2\cdot R\cdot t\cdot\left(\frac{\pi}{2}-\arcsin\left(\frac{r}{R}\right)\right)+2\cdot r\cdot t\cdot\pi}{(R^2+R\cdot t+0.25\cdot t^2)\cdot\left(\frac{\pi}{2}-\arcsin\left(\frac{r}{R}\right)\right)+(r^2+r\cdot t+0.25\cdot t^2)\cdot\pi} \tag{2.1}$$

where *R*, *r* and *t* are geometrical parameters of the core structure given in Fig. 2.1 and ρ_S is the density of the core's material.

2.1.1.2. The stiffness parameters

The effective properties of a cellular material can be described in two different scales: the macroscopic, global level and the microscopic, local level. In global level, the cell is considered as an elastic body whose dimensions are equivalent to the overall dimensions of the cell, i.e. homogenized properties are considered. The microscopic level refers to the cell itself, Fig. 2.2. The macroscopic level is related to the microscopic level, [79]. Therefore, the effective elastic module describes the macroscopic behaviour of the cellular structure and can be determined from:

$$\sigma_{ij}^* = E_{ij}^* \cdot \varepsilon_{ij}^* \tag{2.2}$$

$$\varepsilon_{ij}^* = \frac{\Delta l_{microstructure}}{l} \tag{2.3}$$

$$\Delta l_{microstructure} = f(\delta) \tag{2.4}$$

where δ is the displacement at the point of application of load, for cell loading.

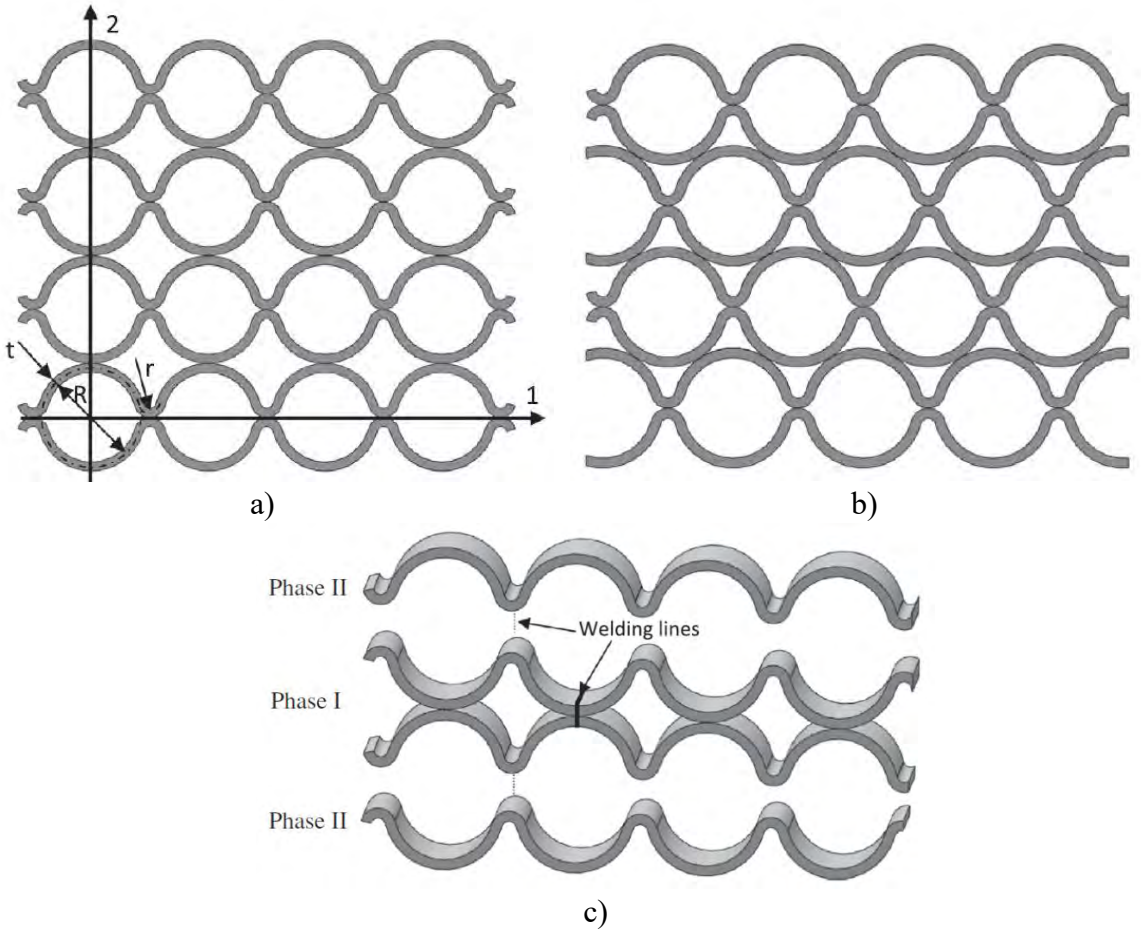

Fig. 2.1. Cylindrical cell honeycomb core structure: a) the cells are ordered arranged in two rows; b) the cells are interspersed among others (1 – longitudinal direction; 2 – in-plane transverse direction); c) the structure assembly procedure, [49].

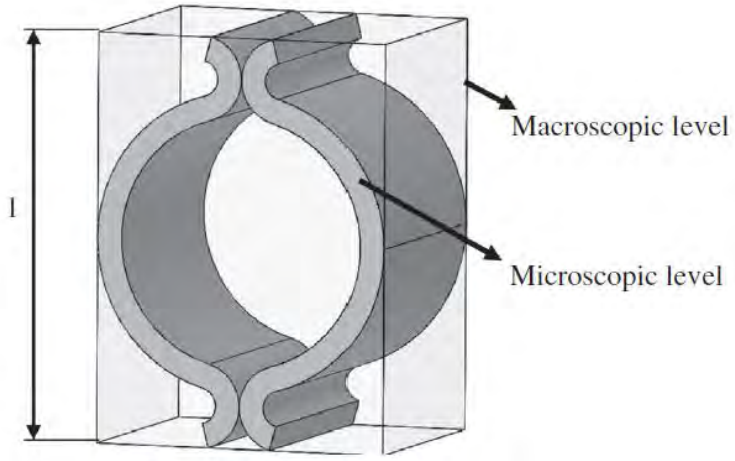

Fig. 2.2. The homogenized unit cell, [49].

The in- and out-of-plane compression and shear loads have been considered. This gives the stiffness and elasticity matrix components (K_{11}, K_{22}, K_{33}, E_1, E_2, E_3) for extension and (K_{12}, K_{21}, K_{31}, G_{12}, G_{21}, G_{31}) for shear loading.

Mohr-Maxwell's theorem is applied to unit cell. It was considered that the stiffness of a cell, characterized by the stiffness components, multiplied by the number of the cells of a structure gives the overall stiffness of the structure.

- *Compression in longitudinal direction (1)*:

Statically undetermined system from Fig. 2.3.b, was analysed to give the total displacement δ_{1tot}. Thus, we obtain:

$$F = K_{11cell} \cdot \Delta l_{microstructure} = K_{11cell} \cdot 4 \cdot \delta_{1tot} \tag{2.5}$$

$$K_{11cell} = \frac{E_m \cdot I}{4\sqrt{i^2+j^2}} = \frac{E_m \cdot w \cdot t^3}{48\sqrt{i^2+j^2}} \tag{2.6}$$

$$E_1^* = \frac{E_m \cdot t^3 \cdot (2R+4r)}{(2R+t) \cdot 48 \cdot \sqrt{i^2+j^2}} \tag{2.7}$$

where K_{11cell} is the cell stiffness in the longitudinal direction, F is the applied force, E_m is the material elasticity modulus, I is the second moment of inertia of the cell wall section, w is the height of the cell, t is the thickness of the cell wall and the i and j are coefficients; these are defined in detail in **Appendix 1**.

Thus, for a structure with n cells, the total stiffness in longitudinal direction, K_{11}, is given by the stiffness of a cell, K_{11cell}, multiplied by the number of cells:

$$K_{11} = n \cdot K_{11cell} \tag{2.8}$$

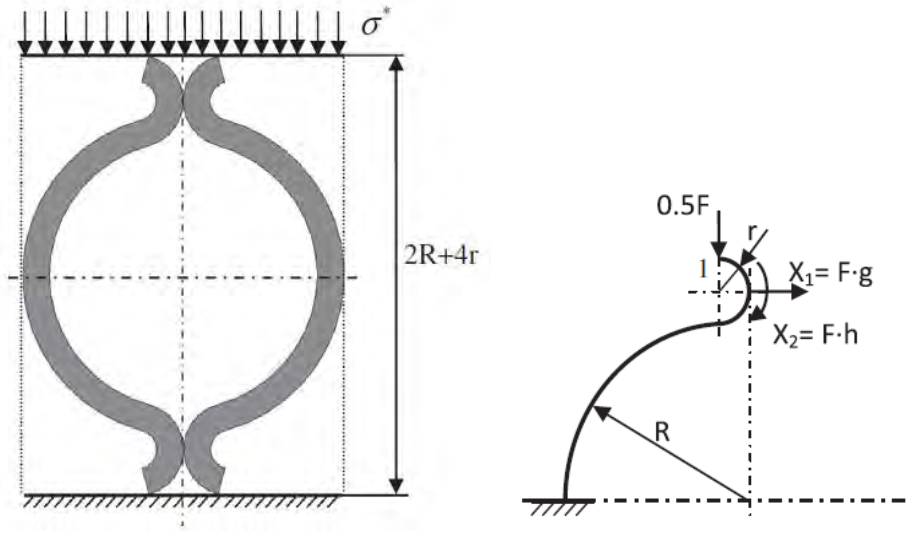

a) b)

Fig. 2.3. Compression loading of the cell: a) applied stress in the longitudinal direction; b) statically undetermined system (g and h are defined in **Appendix 1**), [49].

- *Compression in transverse direction (2) of the cell (Fig. 2.4):*

Applying the same procedure as in the first case, it follows:

$$F = K_{22cell} \cdot \Delta l_{microstructure} = K_{22cell} \cdot 4 \cdot \delta_{1tot} \tag{2.9}$$

$$K_{22cell} = \frac{E_m \cdot I}{4 \cdot i} = \frac{E_m \cdot w \cdot t^3}{48 \cdot i} \tag{2.10}$$

$$E_2^* = \frac{t^3 \cdot E_m \cdot (2R+t)}{48 \cdot i \cdot (2R+4r)} \tag{2.11}$$

In Eq. (2.10), K_{22cell} is the cell in-plane stiffness for transverse direction and i is a coefficient defined in **Appendix 1**.

For a structure with n cells, the stiffness is:

$$K_{22} = n \cdot K_{22cell} \tag{2.12}$$

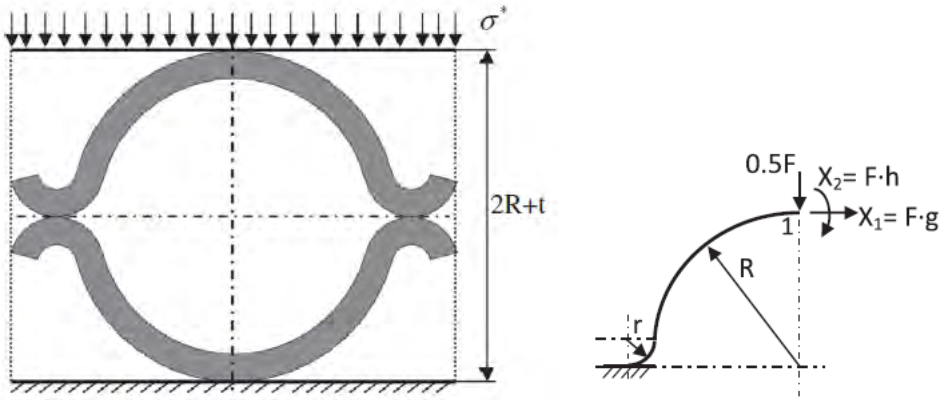

a) b)

Fig. 2.4. Compression loading of the cell: a) applied stress in the in-plane transverse direction; b) statically undetermined system (g and h are defined in **Appendix 1**), [49].

For out-of-plane compression, the cell stiffness and effective elastic modulus are given by the following equations:

$$K_{33cell} = \frac{E_m \cdot A}{w} \tag{2.13}$$

$$E_3^* = E_m \tag{2.14}$$

$$K_{33} = n \cdot K_{33cell} \tag{2.15}$$

In Eq. (2.13), A is the cross-section area of the cell wall, and w is the height of the cell.

- *Shear in the longitudinal direction (1) of the cell (Fig. 2.5):*

The shear stiffness of the cell and effective shear modulus are:

$$K_{12cell} = \frac{E_m \cdot w \cdot t^3}{24\sqrt{i^2+j^2}} \tag{2.16}$$

$$G_{12}^{*} = \frac{t^3 \cdot E_m \cdot (R+0.5t)}{24 \cdot (2R+4r) \cdot \sqrt{i^2+j^2}} \tag{2.17}$$

where *i* and *j* are defined in **Appendix 1**.

The total shear stiffness is:

$$K_{12} = n_{sc} \cdot K_{12cell} \tag{2.18}$$

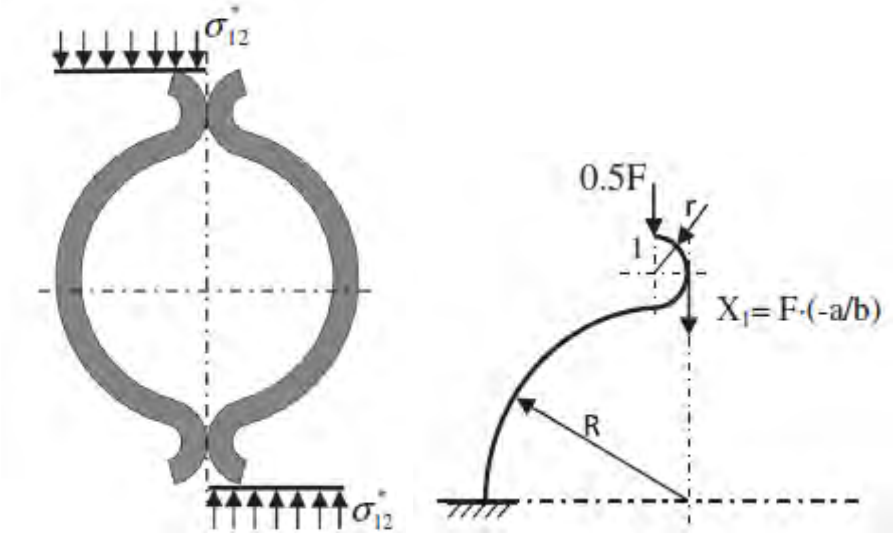

a) b)

Fig. 2.5. Shear loading of the cell: a) applied stress in the longitudinal direction; b) statically undetermined system (*a* and *b* are defined in **Appendix 1**), [49].

- *In-plane shear in the transverse direction (2) of the cell (Fig. 2.6)*:

For the second in-plane shear direction, the cell stiffness and the effective shear modulus are given by the Eqs. (2.19) and (2.20). For a core structure, the shear stiffness can be calculated using the Eq. (2.21) where n_{sc} is the number of sheared cells:

$$K_{21cell} = \frac{E_m \cdot w \cdot t^3}{24 \cdot i} \tag{2.19}$$

$$G_{12}^{*} = \frac{t^3 \cdot E_m \cdot (R+2r)}{24 \cdot i \cdot (2R+t)} \tag{2.20}$$

$$K_{21} = n_{sc} \cdot K_{21cell} \tag{2.21}$$

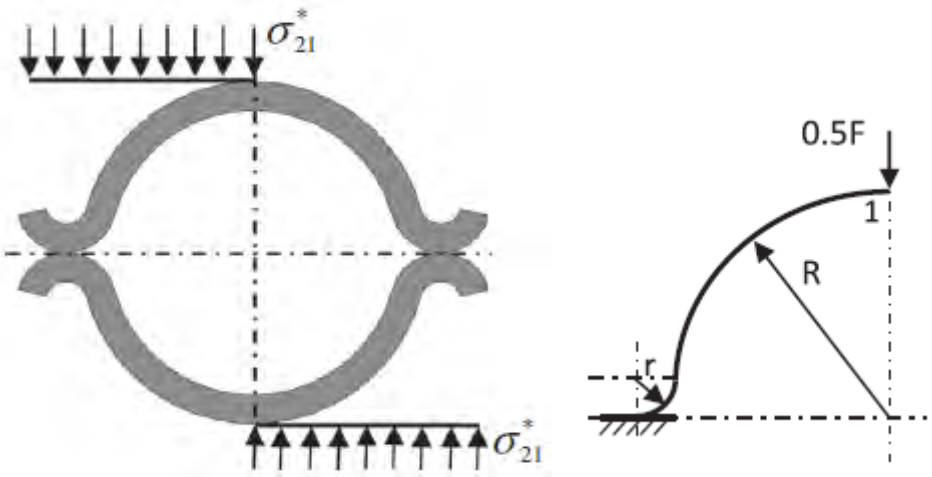

a) b)

Fig. 2.6. In-plane transverse shear loading: a) applied stress in the in-plane transverse direction; b) statically undetermined system, [49].

For the out-of-plane shear loading, the cell stiffness and effective shear modulus are given by the following equations:

$$K_{31cell} = \frac{G_m \cdot A}{2R+4r} \tag{2.22}$$

$$G_{31} = G_m \tag{2.23}$$

$$K_{31} = n_{sc} \cdot K_{31cell} \tag{2.24}$$

where G_m is the shear modulus of the cell material and A is the area of shared sections.

2.1.2. The finite element analysis

- *The cell structures*

A finite element analysis was performed in order to validate the cell stiffness and respectively to verify the analytical relations proposed in the first part of the study. Five types of cylindrical cells with different geometrical dimensions have been considered and each of them were loaded in compression and shear. The FE analysis was performed with ABAQUS v.6-11; Figs. 2.7 and 2.8 presents two analysis models. The loading has been introduced by two rigid surfaces. For each case, one rigid surface was fixed and on the other a displacement was imposed in the loading direction. The analysis was carried out considering geometrical non-linearity. The geometric models were meshed into quadratic tetrahedral elements of type C3D10, the total number of elements in each model being about 57159. The stiffness components were determined based on the slope of the force – displacement curve.

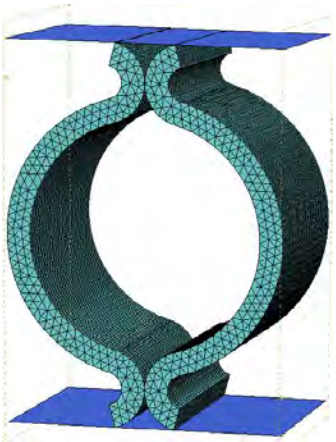

Fig. 2.7. The analysis model for compression in longitudinal direction of the cell, [49]

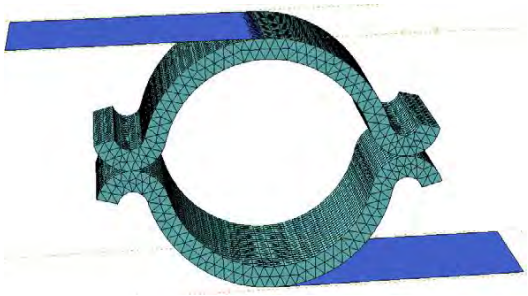

Fig. 2.8. The analysis model for compression in longitudinal direction of the cell, [49]

- *The FEM analysis of the sandwich beam with cylindrical cell honeycomb core*

For this analysis, a sandwich beam with cylindrical cells core was modelled. The core structure consisted of 36 cells with the following dimensions: thickness t = 1 mm, mean radius R = 5.5 mm, the mean connection radius r = 1.23 mm and the modulus of elasticity E_m = 210,000 MPa. The faceplates had the same material as the core. The beam is loaded in three-point bending, Fig. 2.9. The FEM analysis was performed with ABAQUS v.6-11 and the model was meshed into quadratic tetrahedral elements of type C3D10.

The simulation was run for two span lengths. It is known that reducing the span length has a direct effect on the stress state, changing the ratio of shear and bending induced effects. For both cases, the beam was simply supported and a displacement on the loading support was applied, being evaluated the stress state, Figs. 2.10 and 2.11.

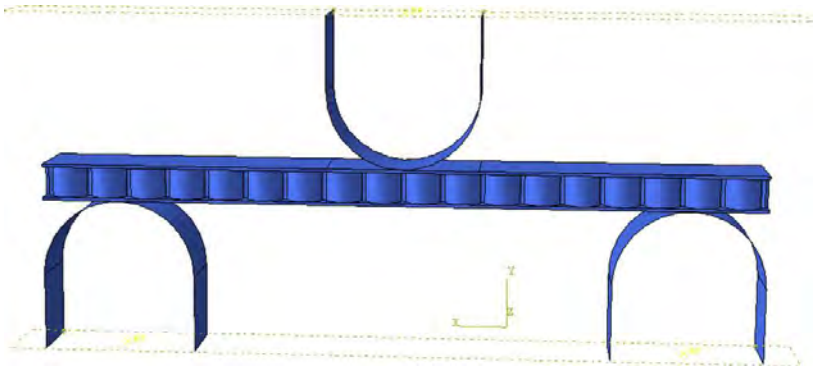

Fig. 2.9. The analysis model of sandwich beam with cylindrical cell core loaded in three-point bending, [49]

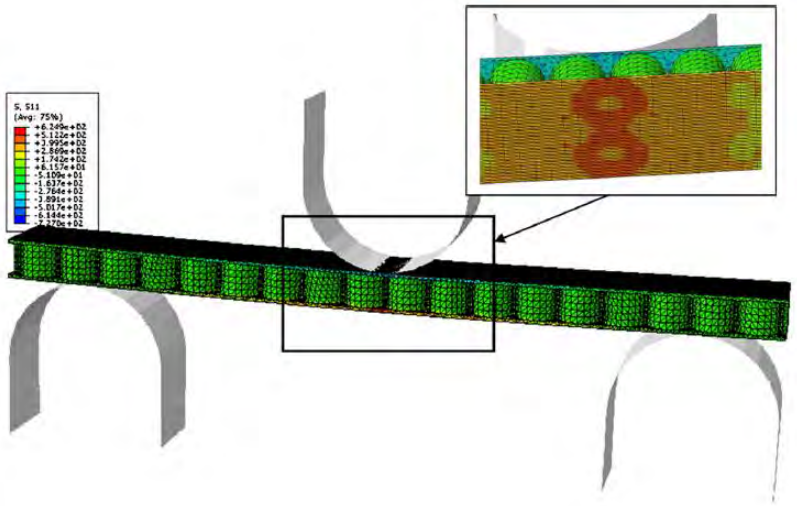

Fig. 2.10. The normal stress distribution on sandwich beam for span length of 187 mm, [49]

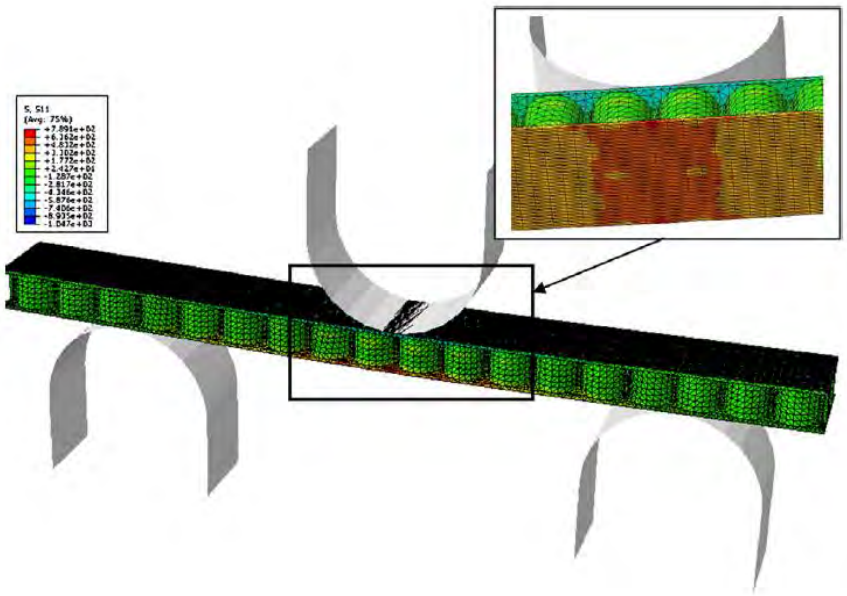

Fig. 2.11. The normal stress distribution on sandwich beam for span length of 160 mm, [49]

Figure 2.12 gives the force–displacement curves for the stiffness in longitudinal direction. Table 2.1 gives the stiffness components, while Table 2.2 gives the effective elastic modules. The analytical stiffness components are in good agreement with the results from FE analyses. Both compression and shear stiffness of the unit cell varies depending on the loading direction, indicating an orthotropic behaviour of honeycomb structures with cylindrical cells. It is also observed that for equal ratio between cell wall thickness and the mean radius (t/R) and that between mean connection radius and the mean radius (r/R), both compression and

shear stiffness and respectively the effective elastic modules in the same direction are independent of the geometrical dimensions of the cell.

The normal stress distribution in the middle cross-section of the sandwich beam is presented in Fig. 2.13, and respectively the stress distribution on the bottom face in Figs. 2.16 and 2.17. Two paths are selected to analyse the stress, one path coincides with the longitudinal plane of the beam, in which cells are connected (Direction 1) and the second coincides with the symmetry plane of the beam (Direction 2) (see Fig. 2.14). In both analysed cases with different span length, the normal stress distribution in the direction 1 (the section containing the connection line of the cells), shows secondary bending effects which are transmitted to the face plates of the structure, causing stress concentrations on the cells, see Figs. 2.15 and 2.16. These are highlighted in the shorter beam where the shear-effects is larger than in the longer beam.

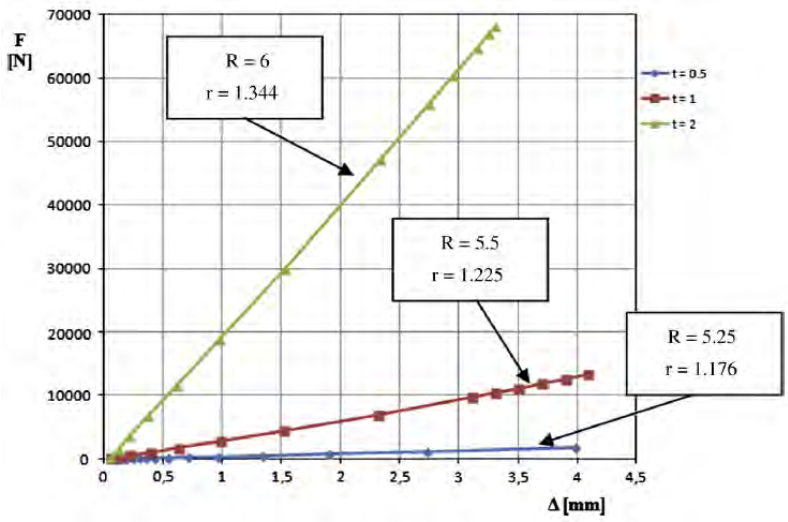

Fig. 2.12. The variation curve between load and displacement of the loading point for compression in longitudinal direction of the cells with three different wall thicknesses, [49]

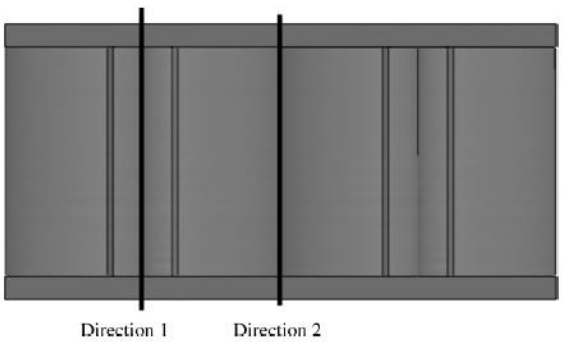

Fig. 2.13. The cross-section of sandwich beam, [49]

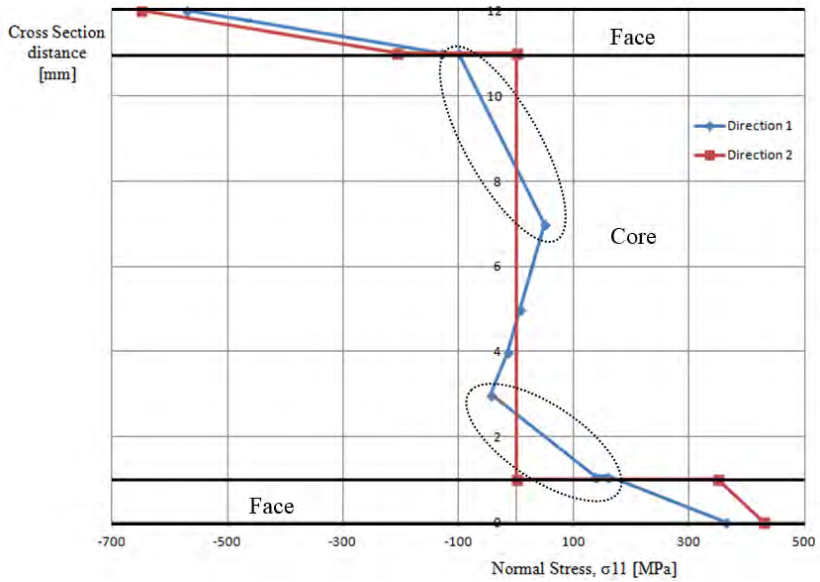

Fig. 2.14. The normal stress distribution on cross-section of the sandwich beam for span length of 187 mm, [49].

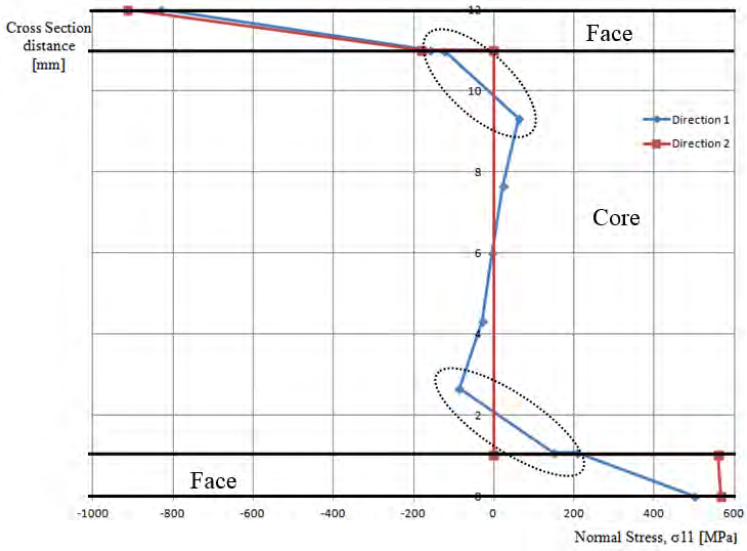

Fig. 2.15. The normal stress distribution on cross-section of the sandwich beam for span length of 160 mm, [49].

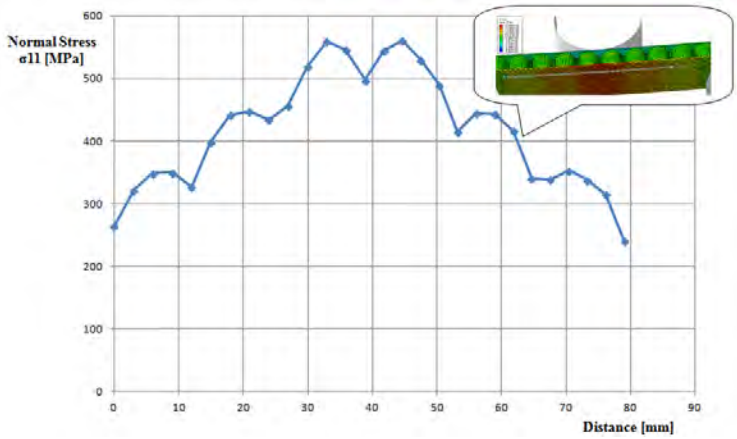

Fig. 2.16. The normal stress distribution on the bottom face, along a cells row (medallion) for span length of 160 mm, [49].

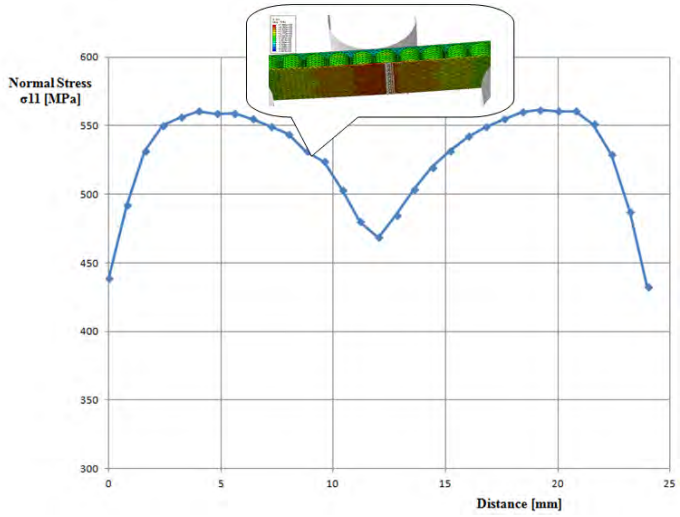

Fig. 2.17. The normal stress distribution on the extreme fiber of the bottom face, in transverse direction, for span length of 160 mm, [49]

Table 2.1. The stiffness components of the analysed structures (E_m = 210000 MPa; G_m = 80000 MPa; w = 10 mm).

Geometrical dimensions of the cell [mm]	**The method of calculation**	**Stiffness components [N/mm]**					
		K_{11cell}	**K_{22cell}**	**K_{33cell}**	**K_{12cell}**	**K_{21cell}**	**K_{31cell}**
t = 0.5 R = 5.25 r = 1.176 r/R = 0.224 t/R = 0.095	Analytical	439.96	279.62	423945.36	386.16	270.95	52617.73
	FEM	436.45	255.64	-	345.011	255.44	-
	Error [%]	-0.79	-8.57	-	-10.65	-5.72	-
t = 1	Analytical	3052.08	1942.33	887342.84	2678.63	1888.16	100628.93

R = 5.5 r = 1.225 r/R = 0.222 t/R = 0.18	FEM	3171.042	1795.23	-	2579.87	1792.69	-
	Error [%]	+3.89	-7.57	-	-3.68	-5.05	-
t = 1 R = 5 r = 1 r/R = 0.2 t/R = 0.2	Analytical	3860.72	2510.9	791681.34	3378.75	2580.74	114285.71
	FEM	3721.94	2524.12	-	3333.33	2512.69	-
	Error [%]	-3.59	+0.52	-	-1.34	-2.63	-
t = 2 R = 10 r = 2 r/R = 0.2 t/R = 0.2	Analytical	3860.72	2510.9	3166725.39	3378.75	2580.74	114285.71
	FEM	3523.55	2437.06	-	3187.57	2436.33	-
	Error [%]	-8.73	-2.94	-	-5.65	-5.59	-
t = 2 R = 6 r = 1.344 r/R = 0.224 t/R = 0.333	Analytical	18863.66	11988.79	1938035.94	16556.75	11617.33	184162.06
	FEM	20638.8	11133.49	-	15248.22	11022.42	-
	Error [%]	+9.41	-7.13	-	-7.9	-5.12	-

Table 2.2. Effective elastic modules of the analysed cells

Geometrical dimensions of the cell [mm]	**Relative density,** $\frac{\rho^*}{\rho_S}$ **[%]**	**Effective elastic modules [MPa]**					
		E_1^*	E_2^*	E_3^*	G_{12}^*	G_{21}^*	G_{31}^*
t = 0.5 R = 5.25 r = 1.176 r/R = 0.224 t/R = 0.095	0.228	60.812	20.23	E_m	13.969	18.726	G_m
t = 1 R = 5.5 r = 1.225 r/R = 0.222 t/R = 0.18	0.389	404.4	146.591	E_m	101.08	125.091	G_m
t = 1 R = 5 r = 1 r/R = 0.2 t/R = 0.2	0.412	491.365	197.285	E_m	132.737	164.229	G_m
t = 2 R = 10 r = 2 r/R = 0.2 t/R = 0.2	0.412	491.365	197.285	E_m	132.737	164.229	G_m

t = 2 R = 6 r = 1.344 r/R = 0.224 t/R = 0.333	0.591	2341.25	965.948	E_m	666.996	720.939	G_m

During this analysis, secondary bending effects due to shear were observed on the cell wall that can cause stress concentration on the faceplates of sandwich structure. The secondary bending stresses have parabolic variation over the unit cell length.

2.2. Fatigue crack growth rate in laser-stake-welded web core sandwich panels

The web-core structure is an all-metal sandwich which consists of the steel panels fabricated as two face plates stiffened by uni-directional system of web plates, fig. 2.18. The connection between the web and face plates is made by laser stake welding applied from outside of the panel. These web core sandwich structures are used in many structural applications such as ship hulls, offshore platforms, bridge decks, and industrial platforms. In these application cases the panels are exposed to variable loading that can cause fatigue damage during the service.

Fig. 2.18. Web core sandwich panel

Fatigue properties of laser-stake welded T-joints have been investigated in Refs. [80 - 82, 83]. It has been observed that the weld has two sharp crack-like notches that act as stress concentrators causing fatigue damage. Frank et al. [82] investigated the fatigue strength of laser-welded web core sandwich panels under bending loading. They based the analysis on the J-integral approach and non-fractured geometry of the stake-welded T-joints. The panel fatigue life was considered as the number of load cycles until the final separation of the face and web plates at one of the panel joints. However, they did not discuss the fatigue crack

propagation rates. Kujala et al [84] showed that in the case of fatigue shear loading of a sample cut from a corrugated core sandwich panel, the cracks initiate on the heat affected zone, develop first along the weld and then turn 45° due to the shear and propagate to the next weld. Based on the full-scale model tests of sandwich panels, Kozak [85] have shown five cracking modes that can occur during the fatigue loading, fig. 2.19. These modes depend on the type of geometry, applied loading and boundary conditions. To further complicate the analysis, when the web plates are welded to a steel plate, residual stresses are introduced into the plate. The stresses caused by external loads interact with the locked-in residual stresses, causing a detrimental effect that results in fatigue crack initiation and further propagation until entire failure of the structure. The reported investigations do not account the fatigue crack growth rates or also the influence of the residual stresses.

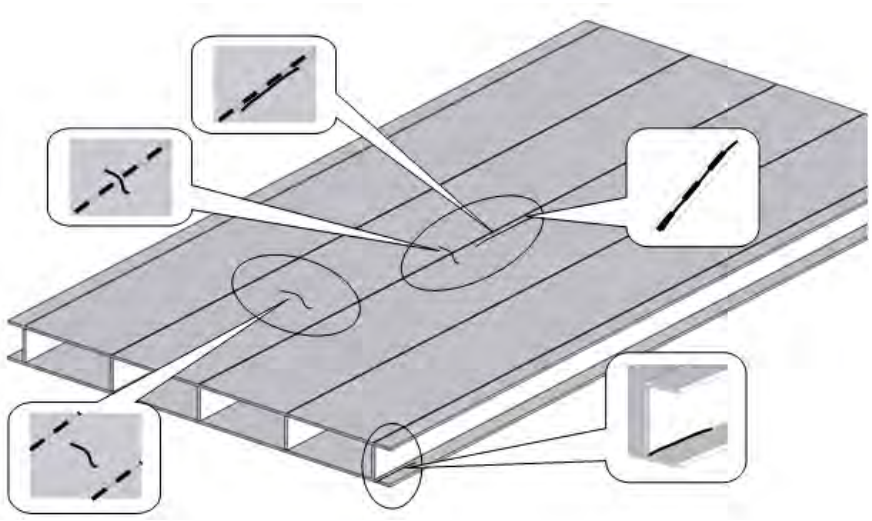

Fig. 2.19. Fatigue cracks in steel sandwich structures according to Kozak, [85]

The fatigue crack growth rate in laser-welded joints was investigated in several studies. Balasubramanian et al. [86] have studied the fatigue crack growth behavior in gas tungsten arc welding (GTAW), laser beam welding (LBW) and electron beam welding (EBW) joints of Ti-6Al-4V. They found that the welding processes significantly reduce the fatigue crack growth resistance of this alloy. Also, the LBW joints had a higher fatigue crack growth resistance compared to GTAW and EBW joints, mainly due to preferable microstructure in the weld region. Lower heat input and faster cooling rate cause formation of very fine lamellar ‘α’ phase in weld metal. The presence of fine lamellar microstructure enhanced the yield strength and ductility of the LBW joint. These improvements are the reasons for higher fatigue crack growth resistance of LBW joints. The influence of post weld

heat treatments (PWHT) on the fatigue crack propagation and mechanical properties of D6AC high strength steel plates and laser welds was analyzed by Tsay et al. [87]. The fatigue crack growth rate curves of laser welds in two different directions (i.e. normal and parallel to the welding directions) were determined on CT specimens. The results showed that PWHT has a reduction effect on fatigue crack growth rate both in the weld metal (WM) and HAZ (Heat Affected Zone) but also in the base metal. The fatigue crack growth rate of the weld metal and HAZ is lower than that of the base metal for similar stress intensity factor range, ΔK. Also, the higher the PWHT temperature causes a less decreasing of fatigue crack growth rate in the WM and HAZ. Tsay et al. in the Reference [88] found similar results, where they studied the effect of PWHT on fatigue crack growth rate in Ti-6Al-4V laser welds. These studies mainly highlight the role of the postweld heat treatment on welded joints, with direct impact on recovery of the microstructure and respectively reducing the residual welding stress state.

It has been known that residual stress has a strong impact on fatigue crack growth behavior, [89, 90]. Even if the residual stresses affect only mean stresses or stress ratios, they have significantly influence on crack initiation, propagation and closure. Lados and Apelian [91] showed that the effect of residual stress on crack growth rates is most pronounced at low ΔK levels (near-threshold region), where the applied stresses are low and, therefore, the ratios of residual stresses to applied stresses are high. Also, a significant amount of research has been developed showing the effect of residual stresses on fatigue crack growth in friction stir welded joints, [92 - 94]. Thus, Pouget and Reynolds [95] found that compressive residual stresses in the HAZ induce crack closure and are responsible for the apparent improvement of fatigue behavior when the crack approaches the weld. In the weld nugget, crack growth rates increase due to tensile residual stresses and microstructure effect.

In the following, a comprehensive study on fatigue crack growth rate in base material of the face plates, HAZ and the weld metal of laser stake welded joint from a sandwich panel is presented. The stress ratio on the fatigue crack growth rate as well as that of the residual stress in crack propagation along the longitudinal direction of the seam are highlighted in this study.

2.2.1. Material and Experimental Methods

2.2.1.1. Material

A sandwich panel with four web plates having a nominal thickness of 4 mm, height of 40 mm and the distance between them of 120 mm is considered. The faceplates had a thickness of 3

mm. The entire sandwich structure had a width of 500 mm and a length of 1000 mm, being saw-cut from large panel of 14 m x 4 m. The connection between the web and face plates was made by laser-stake-welding. The weld thickness is around 1.4 mm.

The material of the faceplate was analyzed in terms of chemical composition, microstructure and mechanical properties. The chemical composition analysis was done by Optical Emission Spectrometry method. The results indicated a low-alloy material with a very low content of carbon (C), see Table 2.3.

Table 2.3. The chemical composition of the material of face plate [wt. %]

C	Si	Mn	P	S	Cu	Al	Cr	Mo	Ni	V
≤0.11	0.009	0.072	0.01	0.006	<0.003	0.023	0.005	0.026	0.013	0.005

For microstructural analysis of the material, samples were collected and prepared according to STAS 4203-74, [96]. The microstructure was analysed both for base material as well as the welded material, see Figure 2.20. The microscopic analysis indicate a ferrite-pearlite structure in which the ferrite is the major phase and the very low volume fraction of pearlite is distributed differently in the ferrite grains. The laser welded joint is formed by the local melting of the base material followed by rapid cooling. Therefore, the weld metal microstructure is characterized by the lath martensite with encapsulated ferrite islands. Due to the very low C content of the base material, the weld metal strength and hardness are low (HV = 158 and estimated yield strength is 365 MPa), instead the ductility and toughness are high.

The mechanical properties of the base material were determined by tensile tests on flat samples according to SR EN ISO 6892-1 standard, [97]. The results indicate that the faceplates material is a low strength steel with the corresponding properties given in Table 2.4.

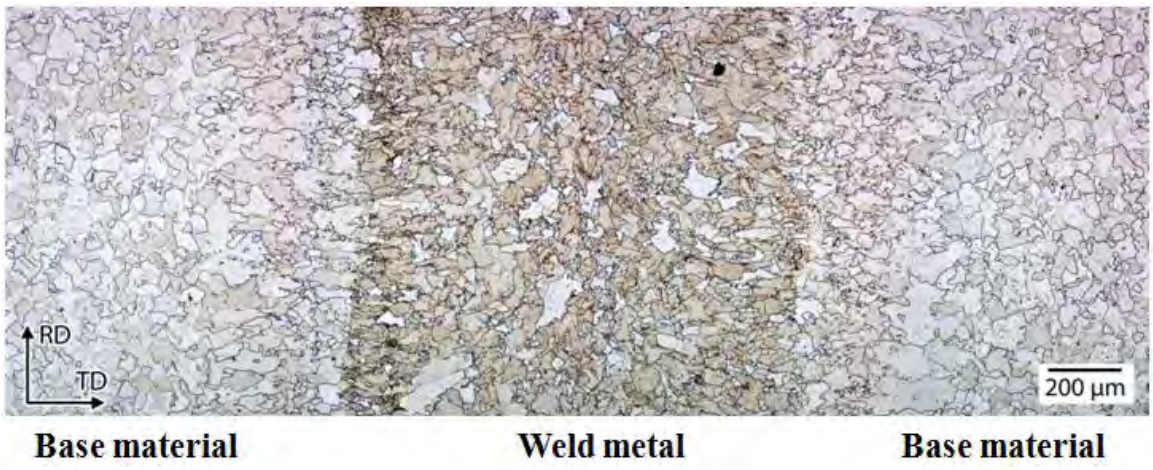

Fig. 2.20. The microstructural analysis on the top face.

Table 2.4. The mechanical properties of the faceplates.

Component	Material	Young's modulus [MPa]	Yield Strength [MPa]	Ultimate Tensile Strength [MPa]	Hardness [HV]
Faceplate	Low strength steel	191000	175	287	92

2.2.1.2. Sample preparation

Compact tension (CT) samples were taken from the base and weld materials both in parallel and transverse direction with respect to weld line, see fig. 2.21. The weld direction is parallel to the rolling direction of the base plate. The CT samples were milled and grinded to final dimensions set by ASTM 647 [19] standard; see Figure 2.22. In total 10 samples were prepared. 8 samples were used for fatigue crack growth rate tests and 2 samples (LTW-4 and LTW-5 in Figure 2.21) were used to determine the residual stress intensity factor, K_{res}.

The specimens LTW-2 and LTW-3 were used for fatigue crack growth rate determination in the welded seam; LTHAZ-2 and LTHAZ-3 were used for fatigue crack propagation in HAZ; LT-15 and LT-16 and respectively TL-10 and TL-11 were used for fatigue crack growth in the base metal.

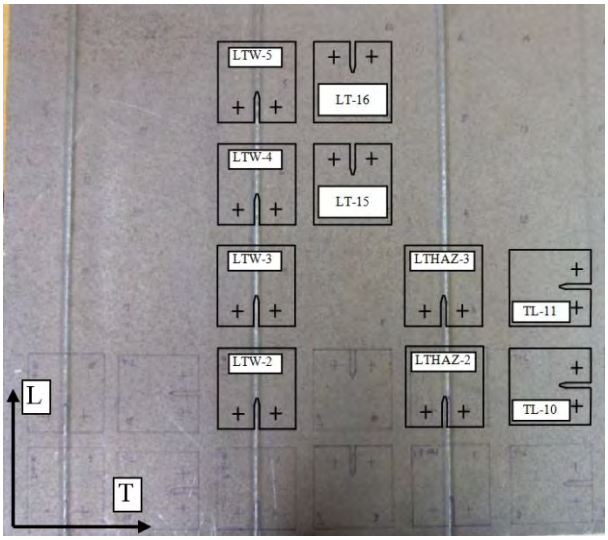

Fig. 2.21. The samples cut from the web core sandwich panel

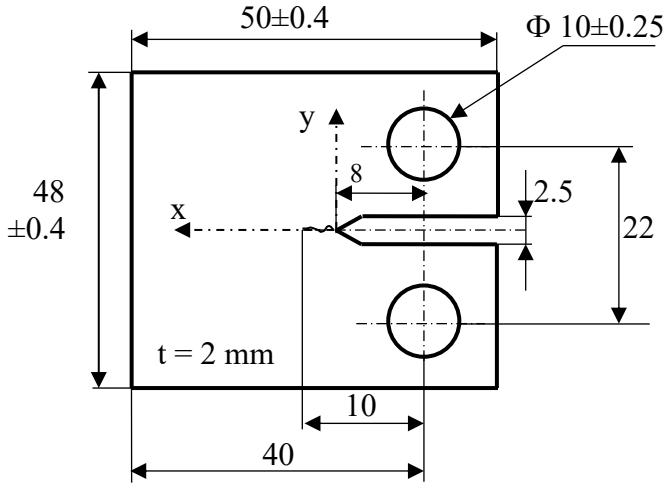

Fig. 2.22. The CT specimen according to ASTM 647 standard.

2.2.1.3. Fatigue crack growth rate tests

The fatigue crack growth rate tests were conducted on a servo hydraulic testing machine model MTS 810 of 100 kN, with a frequency of 3 Hz. The tests were carried out at room temperature and laboratory air conditions, according to ASTM E 647, [98], while the crack length was monitored by the compliance method. Prior to testing, all samples were pre-cracked at constant amplitude cyclic loading to remove the possible effect of the notch on the fatigue crack growth rate. The total length of pre-crack was 2.5 mm. The fatigue crack growth rate curve was determined for the base metal in longitudinal and transverse directions, weld metal and HAZ. A cyclic loading with sinusoidal waveform and two stress ratios, respectively 0.1 and 0.5, were considered. The tests were conducted under *K*-increasing

procedure as is described in the ASTM standard. The crack closure load, P_{cl}, and corresponding closure stress intensity factor, K_{cl} were determined using the compliance-offset technique. Based on these, the effective stress intensity factor range, ΔK_{eff}, was determined as:

$$\Delta K_{eff} = K_{max} - K_{cl} \tag{2.25}$$

2.2.1.4. Experimental estimation of the welding-induced residual stresses

The Cut Compliance Method (CCM) [99] was used to determine the average residual stress state through the thickness of the sample, in x-direction, fig. 2.22, and the corresponding residual stress intensity factor, K_{res}. This method is based on the relaxation of the residual stress by introducing a narrow cut or slit of progressively increasing length and measuring the corresponding strain changes at a suitable location by a strain gage, [99]. Different techniques have been used to introduce the slot for the cut compliance method such as straight edge saw, milling cutter and wire electric discharge machine (WEDM), [100]. Among these it was shown that the WEDM cutting has the smallest influence on strain measurements and thus on the residual stress. Thus, in this study, WEDM was used and the strain gauges were applied on the opposite side of the notch, see fig. 2.23.

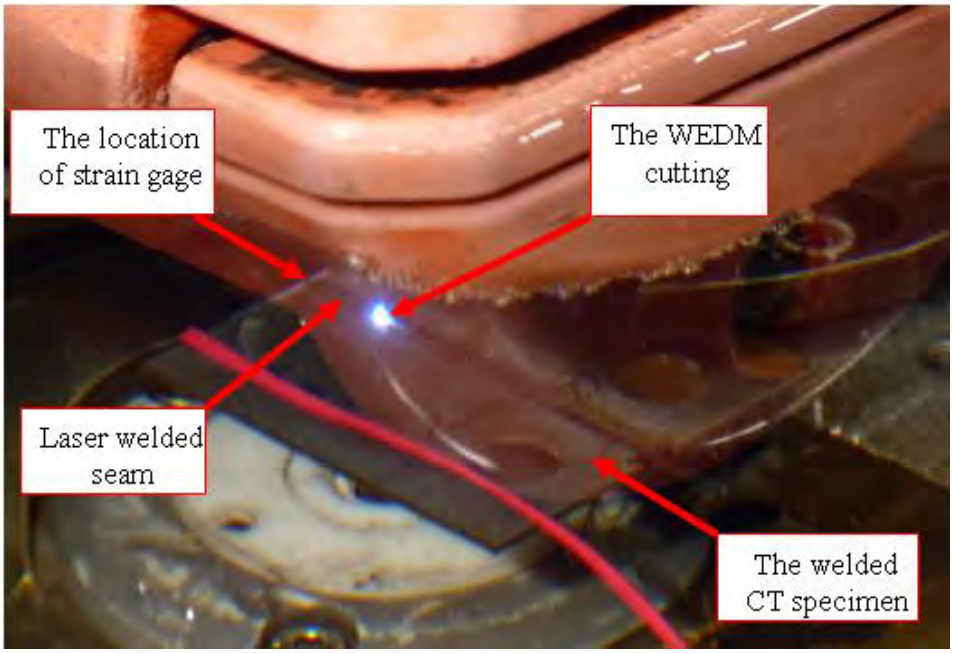

Fig. 2.23. The cutting technique used in CC method.

The slot cutting was done gradually in increments of 1 mm from the notch tip. The strain gauge signal was measured over one minute. The mean value of the strain recorded at each step was plotted against the crack length, determining the strain growth rate with increasing the crack length, dε/da. The residual stress intensity factor was defined according to Schindler, Cheng and Finnie, [99, 101] using:

$$K'_{res} = \frac{E'}{Z(a)} \cdot \frac{d\varepsilon}{da} \tag{2.26}$$

where *E' = E* (the generalized Young's modulus) for plane stress conditions. *Z(a)* is a function, that depends only on the cut depth, the geometry of the specimen and the strain measurement location. For CT specimen with strain gauge applied in the same location as the samples of this study, Schindler [102] proposed the following equation for *Z(a)*:

$$Z(a) = -\frac{2.532}{(W-a)^{1.5}} \tag{2.27}$$

The residual stress distributions were determined from the residual stress intensity factor by using a weight function solution:

$$K_{res}(a) = \int_{a_0}^{a} h(x,a) \cdot \sigma_{res}(x)dx \tag{2.28}$$

where *h(x,a)* is a weight function which depend on the geometry of the specimen. Assuming that the residual stress is constant in each of the n intervals, between each a_{n-1} and a_n, Equation (2.28) can be rewritten in the following form:

$$K_{res}(a_i) = \sum_{j=1}^{i} \sigma_{res,j} \cdot \int_{a_{i-1}}^{a_i} h(x,a_i)dx \tag{2.29}$$

Solving the Equation (2.29) for each step cut it was determined the residual stress distribution. The first values of residual stress intensity factor, K_{res}, were determined after the first cutting step (corresponding to a crack length of 9 mm).

2.2.1.5. Analytical evaluation of the residual stress effect on the fatigue crack propagation

Based on the fatigue crack growth rate data in the weld metal, an assessment of the residual stress intensity factor during crack propagation was made by applying the inverse method and closure approach [105]. The concept of crack closure and the effective stress intensity factor range cause the removal of the stress ratio effect and thus the fatigue crack growth rates in the base metal and weld metal converge to a single curve. This convergence could be affected if in the weld metal there is a residual stress state which can influence the stress ratio, *R*, of the applied load. Therefore, knowing the variation curve of the fatigue crack growth rate function

of the effective stress intensity factor range, ΔK_{eff}, for crack propagation in the base material, a calibration of the crack closure function as given by Newman can be made, [106]:

$$f = \frac{S_0}{S_{max}} = A_0 + A_1 R + A_2 R^2 + A_3 R^3 \quad \text{for } R \geq 0 \tag{2.30}$$

where S_0 is the crack opening/closure stress, S_{max} is the applied maximum stress and R is the applied stress ratio. The constants are A_0 = 0.32565, A_1 = 0.0819, A_2 = 0.8592 and A_3 = -0.26679.

Additional information on calibration of constants $A_0 - A_3$ and the application of crack closure approach for determining the residual stress intensity factor are given in **Appendix 2**.

For fatigue crack growth in the weld metal it has been determined the function:

$$U_w = \frac{\Delta K_{eff,w}}{\Delta K_{app,w}} \tag{2.31}$$

where $\Delta K_{eff,w}$ is the effective stress intensity factor range determined by compliance method in the weld metal and $\Delta K_{app,w}$ is the applied stress intensity factor range.

In the presence of residual stresses, the following equation is used:

$$U_w = \frac{1-f_{tr}}{1-R_{tr}} = \frac{1-[A_0+A_1R_{tr}+A_2R_{tr}^2+A_3R_{tr}^3]}{1-R_{tr}} \tag{2.32}$$

$$R_{tr} = \frac{K_{min}+K_{res}}{K_{max}+K_{res}} \tag{2.33}$$

where U_w is the function determined by Equation (2.31), $f_{tr}(R_{tr})$ is the closure function expressed based on the true stress ratio R_{tr}, K_{max} and K_{min} are the applied stress intensity factors, K_{res} is the residual stress intensity factor to be determined. Iteratively solving the equations (2.31) and (2.32) will conduct to the variation of residual stress intensity factor during fatigue crack propagation in the weld metal.

2.2.2. Results

2.2.2.1. Fatigue crack growth rates and stress ratio effect

Figure 2.24 shows the fatigue crack growth rate curves for the two stress ratios and crack growth rates in parallel and transverse direction for the base plate. The fatigue crack growth in heat affected zone (HAZ) was made on the longitudinal direction of the plate, see fig. 2.25. Similarly, Figure 2.26 shows the fatigue crack growth rate curves for the weld metal.

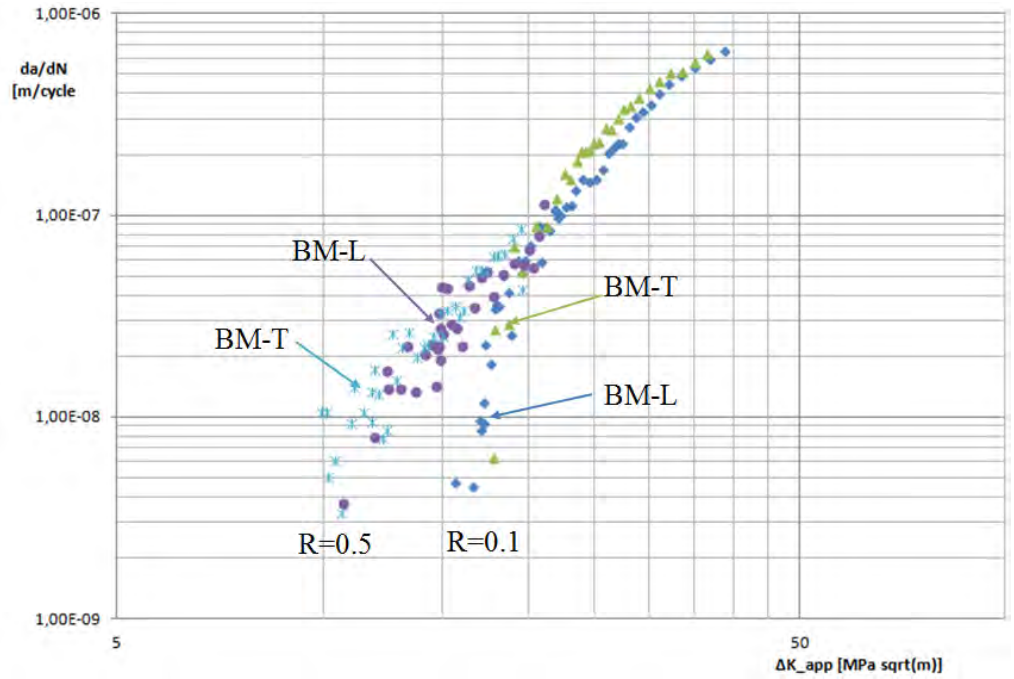

Fig. 2.24. The da/dN=f(ΔK_{app}) curves for fatigue crack growth in longitudinal and transverse direction (BM-L – Base Material–Longitudinal direction; BM-T – Base Material-Transverse direction).

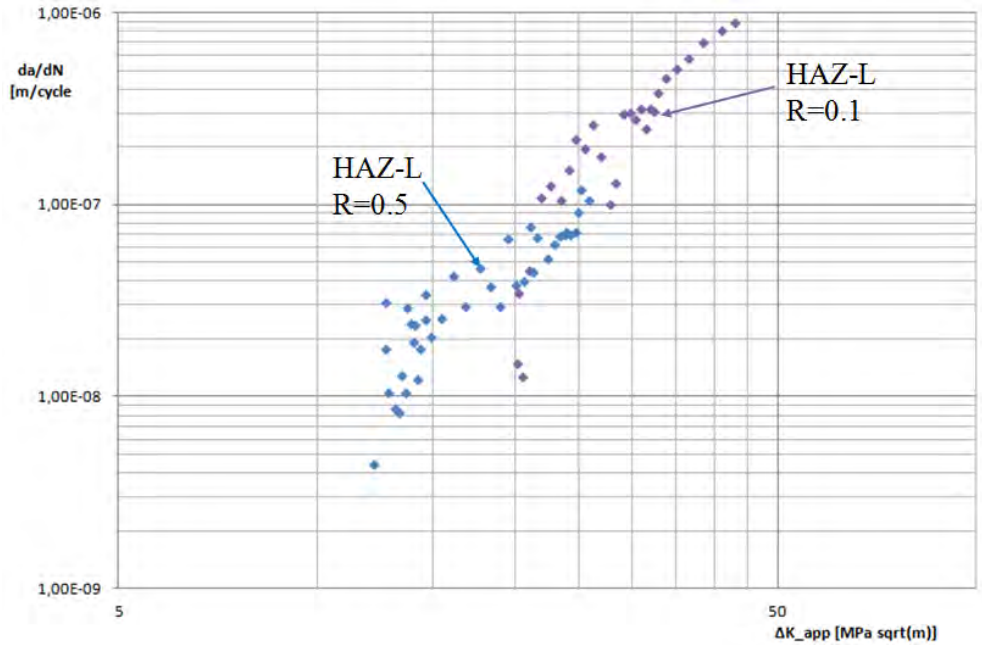

Fig. 2.25. The da/dN=f(ΔK_{app}) curves for crack propagation in HAZ (HAZ-L – Heat Affected Zone-Longitudinal direction).

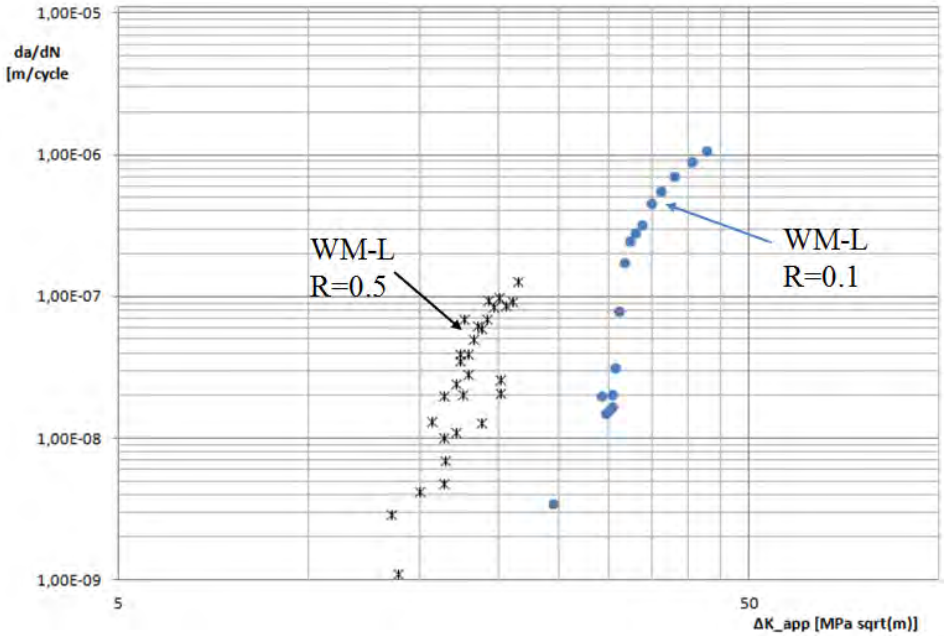

Fig. 2.26. The da/dN=f(ΔK_{app}) curves for fatigue crack propagation in the weld metal (WM-L – Weld Metal-Longitudinal direction).

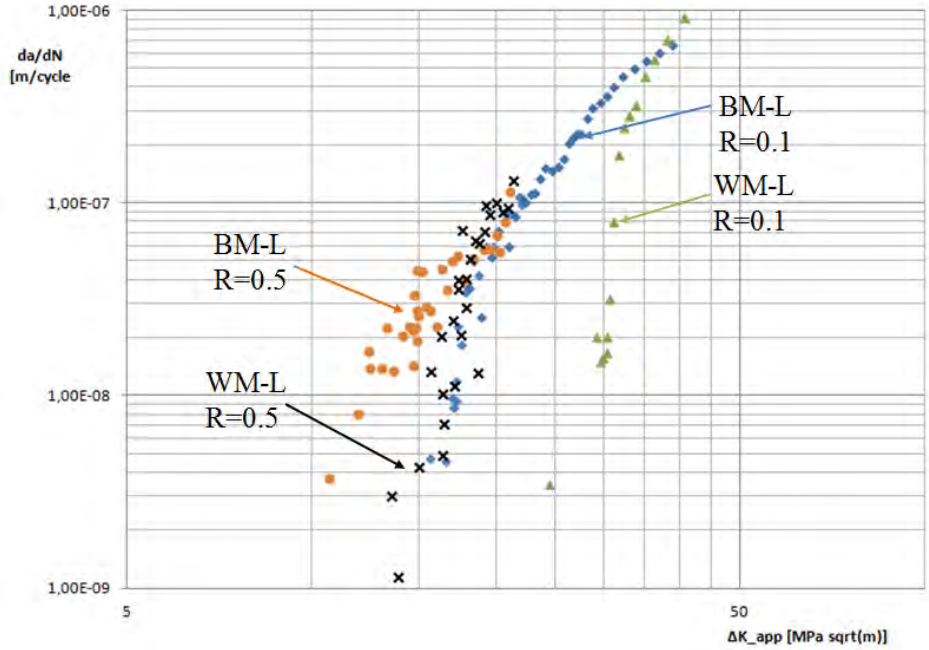

Fig. 2.27. The da/dN=f(ΔK_{app}) curves for fatigue crack propagation in weld metal and longitudinal direction of base metal.

Table 2.5. The propagation constants from Paris' equation for fatigue crack growth rate

Location of crack propagation	R-ratio	C	m	ΔK_{th} [MPa √m]
BM-L (Longitudinal)	0.1	$3 \cdot 10^{-13}$	4.11	16.12
	0.5	$4 \cdot 10^{-12}$	3.219	9.682
BM-T (Transverse)	0.1	$1 \cdot 10^{-11}$	3.109	17.55
	0.5	$3 \cdot 10^{-12}$	3.396	10.689
HAZ-L (Longitudinal)	0.1	$8 \cdot 10^{-12}$	3.095	19.712
	0.5	$4 \cdot 10^{-11}$	2.413	11.765
WM-L (Longitudinal)	0.1	$2 \cdot 10^{-15}$	5.343	29.942
	0.5	$7 \cdot 10^{-14}$	4.594	13.436

In base, HAZ and weld material, the results show a significant stress ratio effect on fatigue crack growth rate in the threshold domain of the curve, corresponding to lower values of the applied stress intensity factor range, ΔK_{app}. As the applied stress intensity factor range increase to the stable propagation domain (Paris region) and the crack length increase, the *R*-ratio effect on the fatigue crack growth rate decreases. In the stable growth domain of the curves, the crack propagation constants for the Paris' equation were defined. The results are presented in Table 2.5 and indicate an increase in the slope for crack propagation in the longitudinal direction in comparison with transverse direction of the plate. There is a decrease in fatigue crack growth rate in HAZ compared to base metal. This decrease is more evident for fatigue crack growth rate at stress ratio $R = 0.5$, see also Table 2.5. Also in the laser stake weld, an apparent improvement of the fatigue crack propagation resistance is observed, see fig. 2.27. This improvement is more obvious for stress ratio 0.1 than for 0.5.

Based on these results, the values of the threshold stress intensity factor range, ΔK_{th}, for the two stress ratios were estimated. Thus, the threshold values corresponding to fatigue crack growth rate of $1 \cdot 10^{-10}$ m/cycle are shown in Table 2.5. It can be seen clearly in these results that with increasing the stress ratio from 0.1 to 0.5, the threshold stress intensity factor range decreases in some cases almost by half.

2.2.2.2. The residual stress effect on fatigue crack growth rate

The experimental residual stress intensity factor shows distributions with high values near the notch, which decrease with increasing the crack length, fig. 2.28. The negative values of K_{res} have a tendency to close the crack due to compressive residual stresses, while the positive values keep the crack open and the tensile residual stress does not affect the stress intensity factor range, [107].

It can be observed in Figure 2.29 the distribution of residual stresses ahead of notch tip, which decreases with increasing the crack length. Also, the distribution starts with compressive residual stress, alternating along the crack increase from negative to positive values. Both residual stress and residual stress intensity factor have variable distributions with different effects on the fatigue crack growth rate.

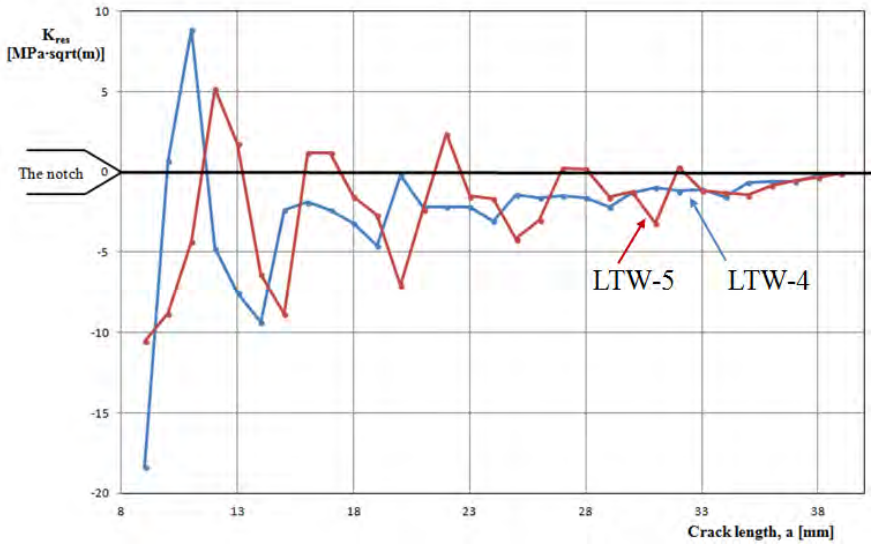

Fig. 2.28. The distributions of residual stress intensity factor: LTW-4 and LTW-5 – experimental values determined by CC method.

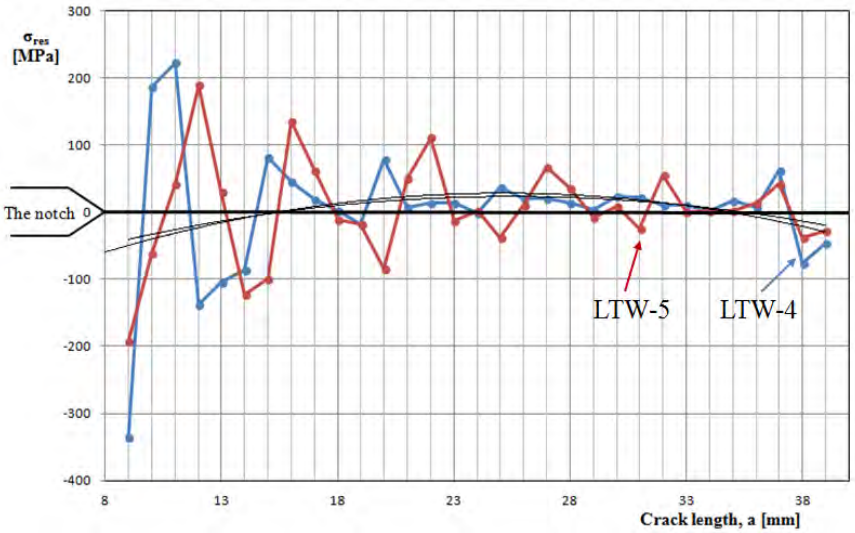

Fig. 2.29. The residual stress distribution for the two specimens tested by CC method (black lines give the average values).

Figure 2.30 shows the effect of residual stress intensity factor on the fatigue crack growth rate in the weld metal, for stress ratio 0.1.

Each value of ΔK_{eff} determined for the fatigue crack propagation in the weld metal, is affected by a certain amount of K_{res}. Therefore, by applying the procedure described in the relationships (2.31) – (2.33), the value of K_{res} affecting the fatigue crack propagation at that point and how it is affected can be determined.

In the threshold domain, the crack growth is influenced by a positive residual stress field, which maintain the crack open and thus the effective stress intensity factor range, ΔK_{eff}, is close to that applied for the weld metal. As the crack length increases and the fatigue crack growth rate reaches the transition domain of the curve, the effect of positive K_{res} decreases and the crack tip enter a field dominated by the negative residual stresses. These stresses cause crack closure and thus ΔK_{eff} corresponding to the welded metal decreases. In the stable propagation domain of the fatigue crack growth rate curve, continues to increase the influence of negative residual stress intensity factor and thus ΔK_{eff} corresponding to the weld metal decreases until the level of ΔK_{eff} corresponding to the base metal.

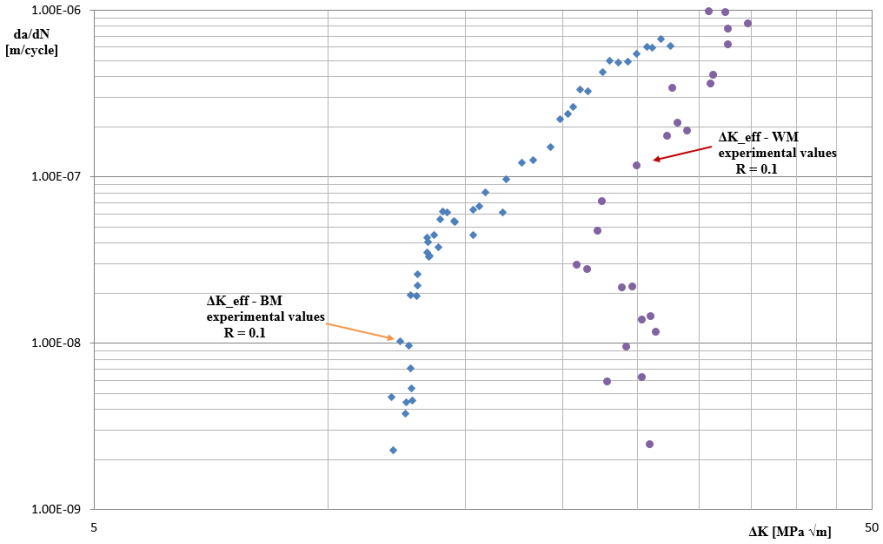

a)

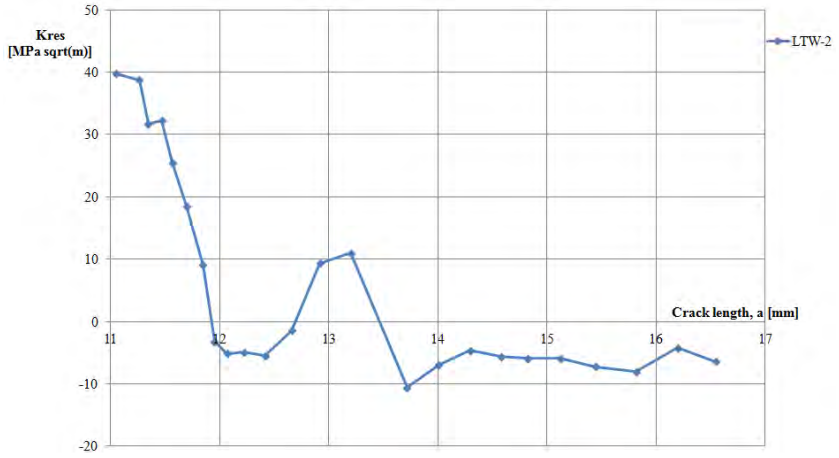

b)

Fig. 2.30. The residual stress effect on the fatigue crack propagation: a) fatigue crack growth rate curves (R = 0.1, BM – base material and WM – weld material); b) The residual stress intensity factor during fatigue crack growth.

2.2.2.3. Fatigue cracking mechanism

Analyzing the fracture surfaces of the samples from the base metal it has been determined the fracture mechanism that led to fatigue crack propagation. The surface analysis was done on an optical microscope Nikon EPIPHOT 200 with magnification of 10x, and scanning electron microscope ZEISS-ULTRA 55. Ever since the fatigue crack initiation phase, the fracture surface shows multiple microcracks and detachments oriented along the direction of crack propagation, fig. 2.31.

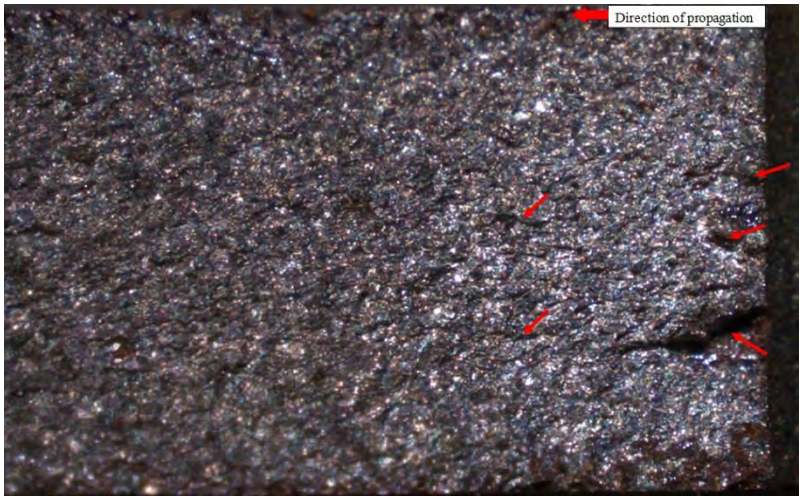

Fig. 2.31. The fracture surface of CT specimen at 10x magnification. Microcracks indicated by arrows.

The fracture surface appearance shown in Figure 2.32 was observed in all samples tested from the base metal and HAZ and it was established that the detachments on the direction of crack propagation represent intergranular and respectively intragranular separations. In the case of fatigue crack propagation in the weld metal is preserved the initiation of microcracks and the fracture appearance is more fragile. Cleavage fracture is observed in the welded metal, given by an overloading effect due to positive residual stresses, fig. 2.33.

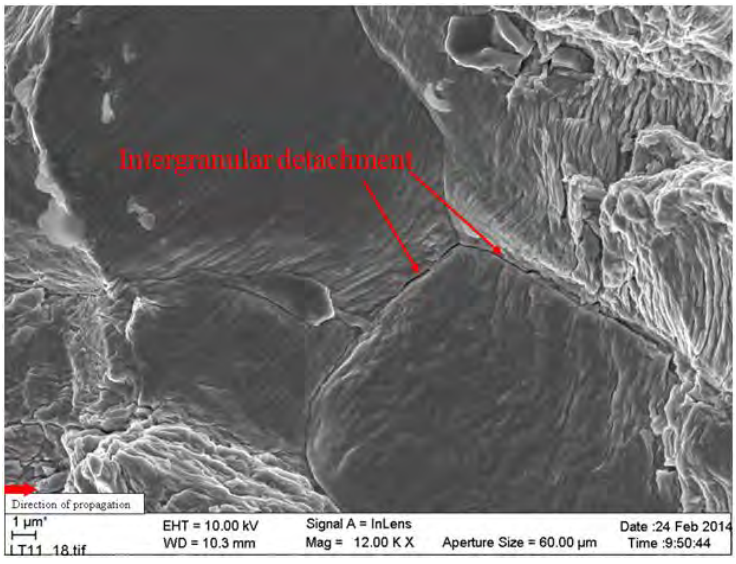

Fig. 2.32. The fracture surface of CT specimen at 12000x magnification for crack propagation in base metal.

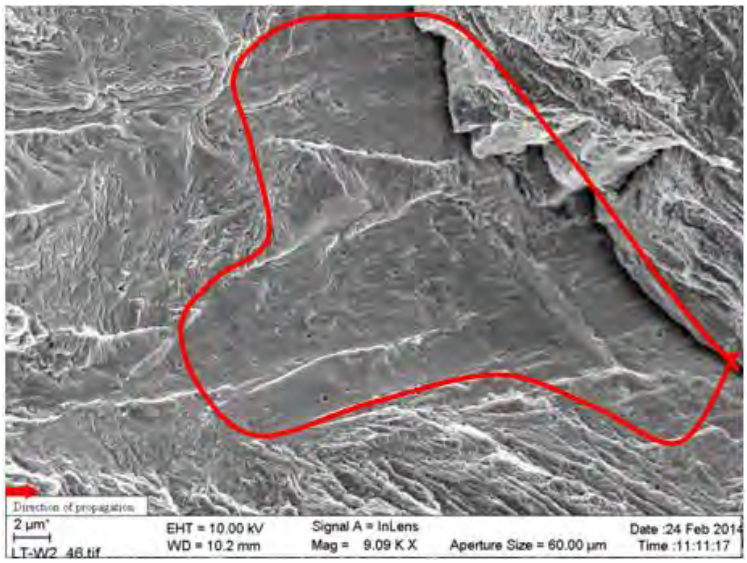

Fig. 2.33. The fracture surface of CT specimen at 9000x magnification for crack propagation in weld.

The results of fatigue crack propagation in base material longitudinal direction have shown that the crack starts to propagate at a lower threshold value than for the crack propagation in transverse direction. The threshold domain is narrower for the case of fatigue crack propagation in the transverse direction. Once the crack reaches the stable propagation domain, the fatigue crack growth rate in transverse direction has a slight decrease compared to that in the longitudinal direction. The stress ratio effect is in the same trend with that reported by Makhlouf and Jones [103], which has showed that, similar to the behavior of other low-strength steel, the fatigue crack growth rates in the stable domain are relatively insensitive to load ratio. Instead, the threshold values are substantially decreased with increasing R-ratio. Kusko et al. [104] have shown a dependence of da/dN on the R ratio at lower da/dN, followed by a convergence to a single curve at higher fatigue crack growth rates.

Figure 2.34 presents the threshold stress intensity factor range, ΔK_{th}, as a function of the corresponding hardness of the base material, HAZ and weld metal for the two stress ratios. In the case of stress ratio $R = 0.5$ the increase of ΔK_{th} with hardness is almost proportional even in the case of weld metal where the residual stress has a decreased effect. Instead, in the case of ΔK_{th} corresponding to weld metal and $R = 0.1$, besides the microstructure an additional effect is given by the residual stress.

The results showed a higher resistance to propagation in the case of fatigue crack propagation in HAZ compared to fatigue crack propagation in longitudinal direction of base

material. It is also observed that in the weld material there exists a combined effect of residual stress field with the material microstructure on fatigue crack propagation behavior. In this respect at low values of ΔK_{app} the positive residual stresses have a major effect on fatigue crack propagation. Thus, the residual stresses keep the crack open causing a rapid propagation of fatigue crack in the threshold domain. This effect combined with the behavior of the welded material, given by the microstructure, cause cleavage fracture during crack propagation. In contrast, in the transition and respectively stable domain of the fatigue crack propagation curve, the residual stress field becomes predominantly negative causing crack closure effects.

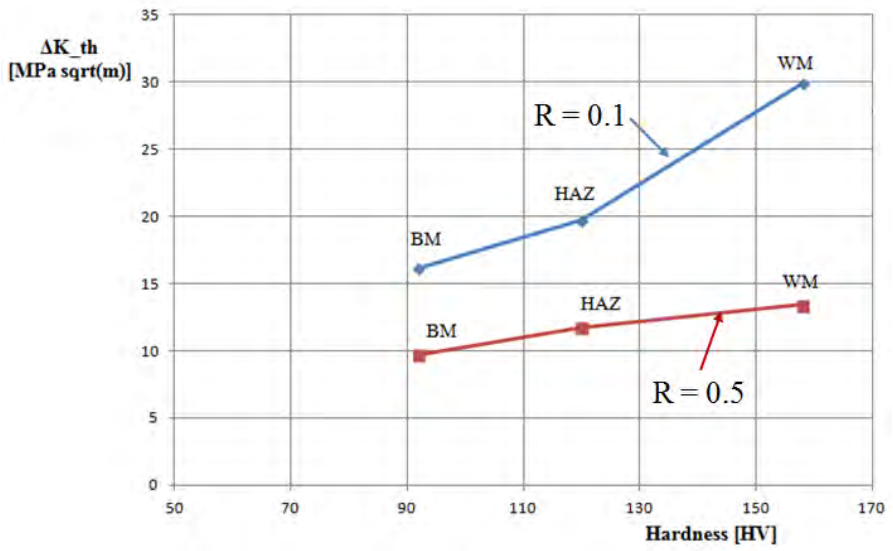

Fig. 2.34. The variation of threshold stress intensity factor range with the material hardness (BM – base material, HAZ – Heat Affected Zone, WM – Weld Metal)

The analysis of fracture surfaces allowed the establishment of a fracture mechanism during fatigue crack propagation. Thus, during cyclic loading, due to different size, orientation from the loading direction and different volume fraction of pearlite, the ferrite grains are deformed differently towards each other. This causes a shear stress at the boundary between grains, which leads to intergranular detachments. These intergranular detachments can extend also in the ferrite grains developing microcracks. The earlier microcracks cause a weakening of the cross-section load capacity and an overload of the grains that fail by plastic yielding forming a new front of the crack propagation. In the same sense, Motoyashiki et al. [108] have shown that grains or phase boundaries with a high degree of mechanical mismatch develop cracks very easily by high local stresses and strains at boundaries. The intergranular cracks appear

rather early in the fatigue life. They also showed that the intergranular dislocations in martensite/ferrite phase and a ferrite/ferrite grain boundary can continue with propagation in the ferrite grains. The crack initiation in ferrite grains appeared as a result of the action of the slip systems with high Schmid factor value.

Korda et al. [109] analyzed the fatigue crack growth rate in hot rolled low carbon ferritic-pearlitic steel plates with two volume fractions of pearlite, 25.1% and respectively 20.3%, showing that the crack propagated in ferrite grains and followed the interface between ferrite grain and pearlite particle when encountered pearlite particle.

This is an experimental study to analyze the fatigue crack growth rate in the faceplate of a laser welded web core sandwich panel. The fatigue crack growth rate tests carried out in the base metal, HAZ and weld metal showed a significant effect of the stress ratio on fatigue crack growth rate in the threshold domain which decreases as the stress intensity factor range increase to the stable domain of the crack propagation. Furthermore, the tests indicated that the fatigue crack growth rate is greater for the rolling direction of the plate, than in the transverse direction. Also, the fatigue crack growth rate in HAZ is less than in the base metal. In welded metal a high influence of the residual stress state on fatigue crack growth rate was observed.

The residual stress effect was approached both experimentally in order to highlight the magnitude, distribution and type of residual stresses (positive or negative) in the samples taken from welded joints, but also analytically with direct purpose of highlighting the effect of residual stress on the fatigue crack growth rate. For the analytical evaluation of the residual stress intensity factor, K_{res}, the inverse method based on crack closure has been used, which allows the direct extraction of the K_{res} from the crack growth rate data through the effective stress intensity factor range, ΔK_{eff}.

The highlights presented in this study have both general character on the fatigue crack propagation characteristics in the faceplate material (the propagation constants from Paris' equation and respectively the threshold stress intensity factor range) and individual character concerning the residual stress state effect on the fatigue crack growth rate in the weld metal.

The appearance of the fracture surfaces revealed the fatigue fracture mechanism during crack propagation. The fatigue fracture is preceded by the occurrence of microcracks, which are mostly intergranular detachments.

2.3. The influence of crack tip shielding on fatigue crack propagation

One of the current approaches of fatigue damage predictions is based on the damage tolerance concept. This concept starts from the premise that each component has a potential defect and the fatigue life is based on the number of cycles required for an initial crack to grow to the critical value. Using an appropriate fatigue crack growth equation, the initial fatigue crack is propagated through iterative calculations which consider the loading spectrum, material properties and component geometry. One of the elements that confer the degree of accuracy of fatigue crack growth predictions is represented by the crack closure phenomenon. According to the review made by M. N. James, [110], on the crack closure, the first study that has highlighted such a phenomenon was presented by Christensen in 1963, [111]. Performing fatigue crack growth tests on centre-cracked specimens of 2024-T3 aluminum alloy it was observed an increase in fatigue life occurred in the presence of trapped oxide particles between the fracture surfaces.

However, of reference are the Elber's studies from 1970 and 1971, [112 - 113]. Based on residual stress distribution and resultant forces analysis in centre-cracked plate specimen under zero-to-tension loading, Elber showed that the crack is fully open only for a part of the loading cycle. This being attributed to the field of plastic deformations in the wake of crack tip. Due to direct implications in fatigue crack growth retardation, the crack closure phenomenon has been extensively analysed both experimentally and numerically.

In 1988, R.O. Ritchie, [114], brings into discussion the idea that fatigue crack growth retardation can be achieved by reducing the applied load or by toughening the material. He presents two classes of toughening mechanisms: intrinsic, by increasing the inherent microstructural resistance to crack advance and extrinsic, where the toughness arises from mechanisms of *crack tip shielding*. This term was first introduced and covers four categories: crack deflection and meandering, zone shielding (transformation toughening, microcrack toughening, crack wake plasticity, crack field void formation, residual stress fields, crack tip dislocation shielding), contact shielding (wedging, bridging, sliding, wedging + bridging), combined zone and contact shielding (plasticity-induced crack closure, phase transformation-induced closure). In the same manner Pippan and Hohenwarter, [115], describes the role of intrinsic and respectively extrinsic mechanisms in fatigue crack propagation, where the intrinsic mechanisms are responsible for the formation of new fracture surfaces at the crack tip by cyclic deformation. In a different study, Mutoh et al., [116], show that in steels with ferrite-pearlite microstructure (networked or distributed pearlite), besides the crack closure phenomenon there are also other mechanisms of crack-tip stress-shielding phenomena,

respectively branching and interlocking. They define an effective crack tip stress intensity factor range, $\Delta K_{eff,tip}$, that manages to better correlation of fatigue crack propagation data in a single curve, compared to the well-known ΔK_{eff}, [117]. In Reference [118] it is described a model of fatigue crack propagation based on dislocation emission at the crack tip and respectively the dislocations in the plastic zone and plastic wake. The fatigue crack growth rate into a plastic zone can be reduced through a dislocation crack tip shielding mechanism. However, this mechanism can stop the advancing of the crack when the crack tip is fully shielded but does not guarantee that do not form another tip that lead to an extension of the crack in another direction.

Given the above, one can say that fatigue crack propagation is guided by the crack tip shielding mechanisms that acts actively by forming new crack tips and respectively passive crack tip shielding mechanisms. The passive crack tip shielding mechanisms cannot create crack tips if the applied loading does not exceed a certain value. From this point of view plasticity-induced closure, as extrinsic mechanism of combined zone and contact shielding, can be considered passive. If the applied loading does not exceed P_{op}, the crack tip remains protected by the plastic field and the crack does not extend. In the following sections it is presented an analysis of fatigue crack growth into a plastic deformation zone given by an overloading cycle. In the case of constant amplitude loading the introduction of an overloading cycle leads to increasing of the crack opening load corresponding to that cycle. If the crack opening force associated to the overloading cycle, $P_{op,OL}$ is greater than the maximum force of the constant amplitude loading, then the crack tip is shielded, fig. 2.35.

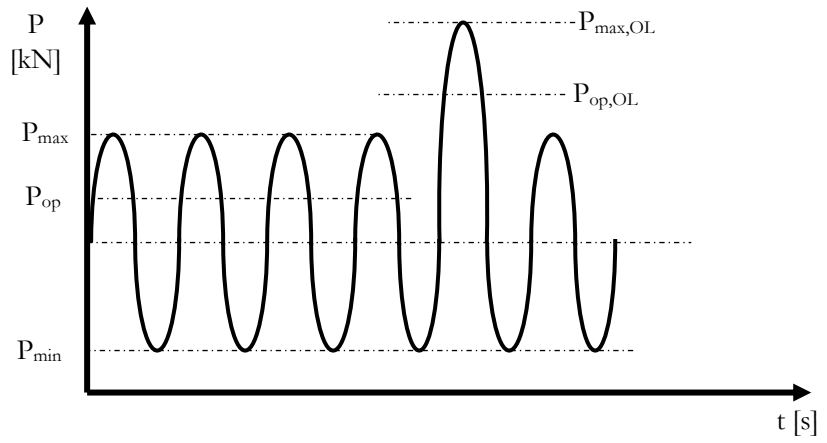

Fig. 2.35. The constant amplitude loading with an overloading cycle, [120]

However, it is known that the fatigue crack propagates within the plastic zone created by the overloading which indicates that once the material is strengthening there are active crack tip shielding mechanisms that helps the crack to growth through the retardation period.
For this analysis, fatigue crack growth rate tests were carried out on a structural steel. The chemical composition and mechanical properties of the material are given in Tables 2.6 and 2.7. The fatigue crack growth rate tests were conducted on CT samples, according to ASTM E 647, [119]. Also, tests have been performed corresponding to plane strain and respectively plane stress state.

Table 2.6. The chemical composition of steel, [%].

C	Si	Mn	P	S	Cr	Ni	W	Al	Cu	N
0.15	0.22	1.46	0.04	0.02	0.05	0.03	0.03	0.04	0.02	0.01

Table 2.7. The mechanical properties of tested material.

Material	**Young's modulus [MPa]**	**Yield strength [MPa]**	**Ultimate strength [MPa]**	**Elongation [%]**
Low-alloy steel	205000	255	368	30

Two CT samples were tested for plane strain conditions with dimensions shown in Figure 2.36 and a thickness of 10 mm. One sample was tested at constant amplitude loading with stress ratio 0.1 and maximum load of 8 kN.

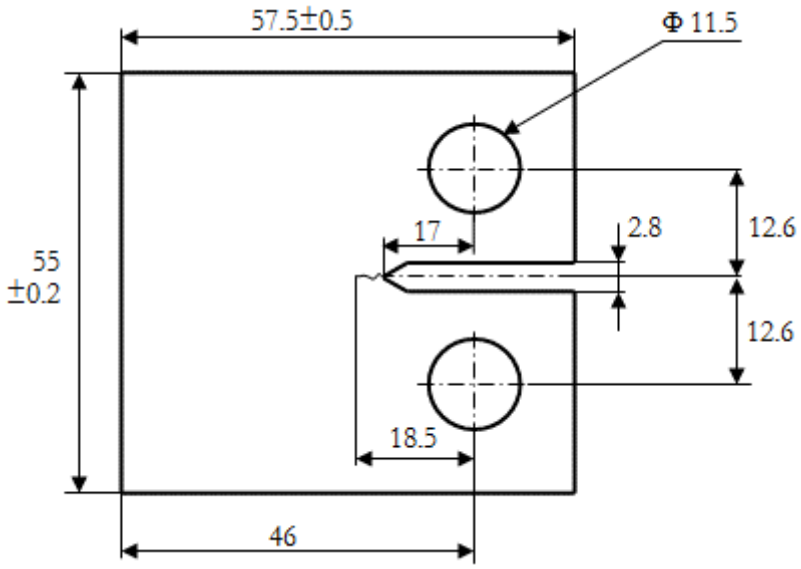

Fig. 2.36. The dimensions of CT samples used in fatigue crack growth rate tests, (units: mm)

On the second sample, after fatigue pre-cracking an overloading cycle was introduced with maximum load of about 20 kN and then continued testing at constant amplitude loading with maximum load of 8 kN and stress ratio 0.1.

For plane stress state, two CT samples were used with the same dimensions as in Figure 2.36 but thickness of 2.4 mm. In all cases the sample dimensions respect the conditions required by ASTM E 647. After fatigue pre-cracking both samples were tested at constant amplitude loading with maximum load of 2 kN and stress ratio 0.1. Also, both samples were overloaded with 26 % respectively 82 % higher than the constant amplitude loading.

During the entire fatigue crack propagation tests the applied force and respectively the crack opening displacement (COD) corresponding to each loading cycle have been recorded. Also, the compliance technique was used to determine the crack length.

All samples were examined by scanning electron microscopy (SEM) aiming to crack evolution before and after the overloading cycle. For plane strain state, the variation of fatigue crack growth rate function of the stress intensity factor range was determined for constant amplitude loading with stress ratio 0.1, fig. 2.37.

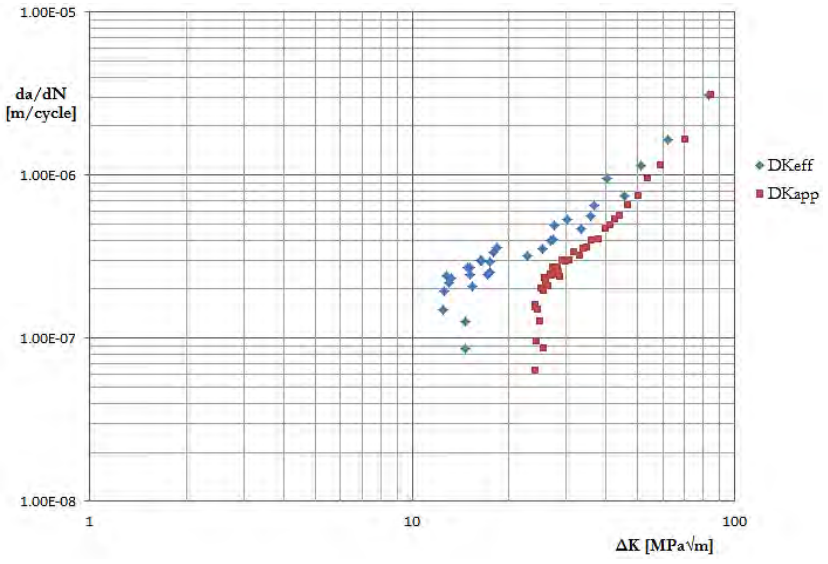

Fig. 2.37. The fatigue crack growth rate function of stress intensity factor range for R = 0.1

Also, based on the curves in Figure 2.37, the propagation constants corresponding to considered loading have been determined. The values are given in Table 2.8.

Table 2.8. The fatigue crack growth rate constants for constant amplitude loading with R = 0.1

Specimen type	Thickness [mm]	R-ratio	Paris constants		$\Delta K_{th,app}$ [MPa√m]	$\Delta K_{th,eff}$ [MPa√m]
			C [m/cycle MPa√m]	n		
CT	10	0.1	$4 \cdot 10^{-11}$	2.51	22.5	10.5

In case of the second sample, after the overloading cycle the testing was continued with constant amplitude loading for a total number of 409768 cycles. Throughout the test the compliance technique could not detect an extension of the crack in the plastic deformation zone created by the overload, fig. 2.38. However, the microscopic analysis revealed that the crack propagated in the plastic deformation zone, fig. 2.39. Moreover, the character of fatigue crack growth in the plastic zone is totally changed in comparison with the propagation character before applying the overload. This indicates a change of the crack tip shielding mechanisms that govern the fatigue crack propagation. From a combined zone and contact shielding mechanisms was switched to a dislocation crack tip shielding mechanism.

Accepting the crack closure function defined by Elber in the relations (2.34) and (2.35), it was made an estimation of the crack opening force corresponding to overloading cycle with maximum force of 20 kN and minimum force of 0.8 kN.

$$U = \frac{\Delta P_{eff}}{\Delta P_{app}} \tag{2.34}$$

$$\text{and } U = 0.5 + 0.4 \cdot R \tag{2.35}$$

For the overloading cycle results:

$$0.5 + 0.4 \cdot R_{OL} = \frac{P_{max,OL} - P_{op,OL}}{P_{max,OL} - P_{min,OL}} \tag{2.36}$$

where R_{OL} is the stress ratio of the overloading cycle.

Solving the equation (2.36) results an estimation value for the crack opening force corresponding to overloading cycle of $P_{op,OL} \approx 10.092$ kN.

The value of $P_{op,OL}$ is higher than the maximum force of the constant amplitude loading and this could be the reason for why the crack compliance technique could not detect the extension of the crack within plastic deformation zone.

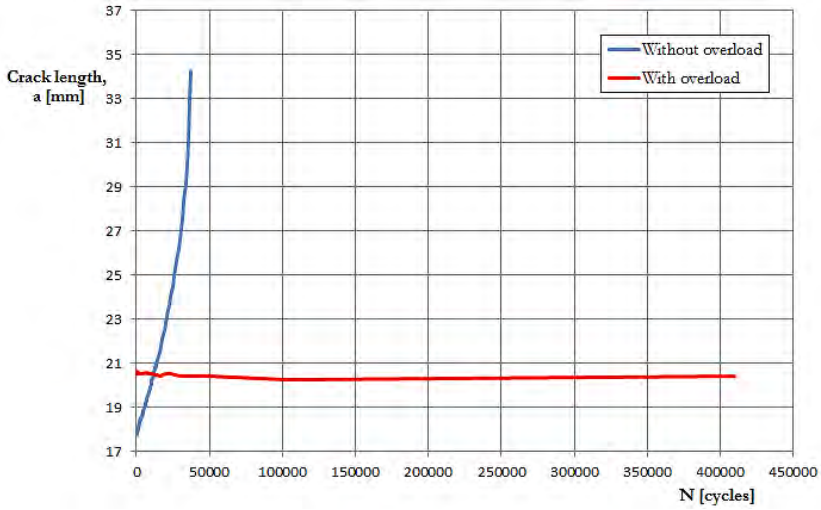

Fig. 2.38. The variation of crack length function of number of cycles

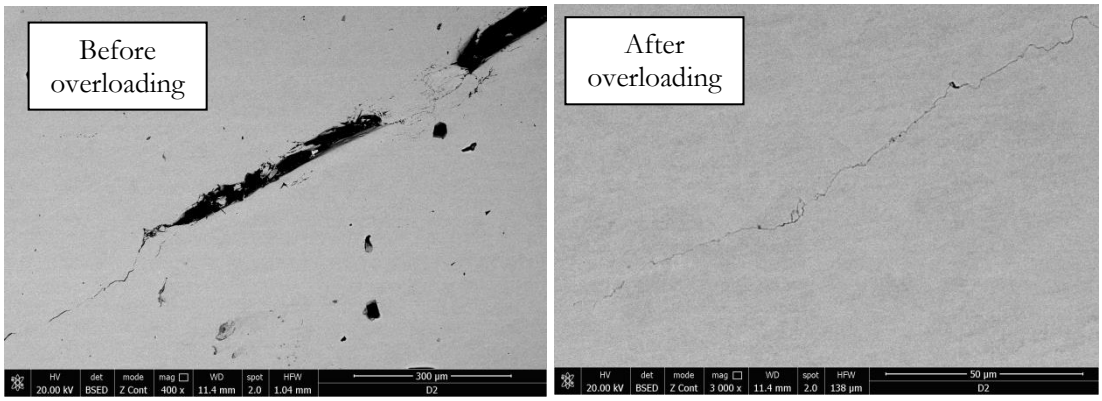

Fig. 2.39. The fatigue crack path before and after overloading

Also, for plane stress state an apparent effect of the overloading has been highlighted on the character of fatigue crack propagation. In Figure 2.40 there are given the variations of fatigue crack growth rate function of the crack length for the two samples overloaded with 26%·$P_{max,CA}$ respectively 82%·$P_{max,CA}$, ($P_{max,CA}$ is the maximum force of the constant amplitude loading). Based on the recordings of loading force and respectively COD, (fig. 2.41), has been determined the crack opening load corresponding to the overloading cycles. The values are given in Table 2.9.

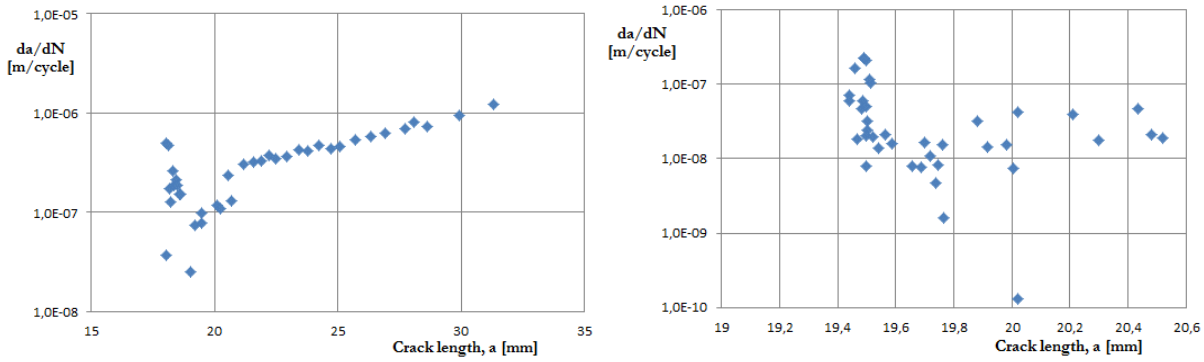

a) b)

Fig. 2.40. The variation of fatigue crack growth rate function of crack length for: a) 26%$P_{max,CA}$ overloading; b) 82%$P_{max,CA}$ overloading

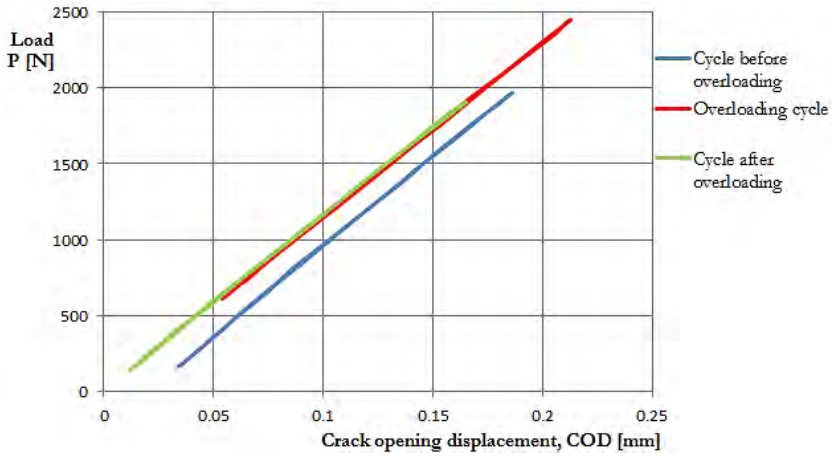

a)

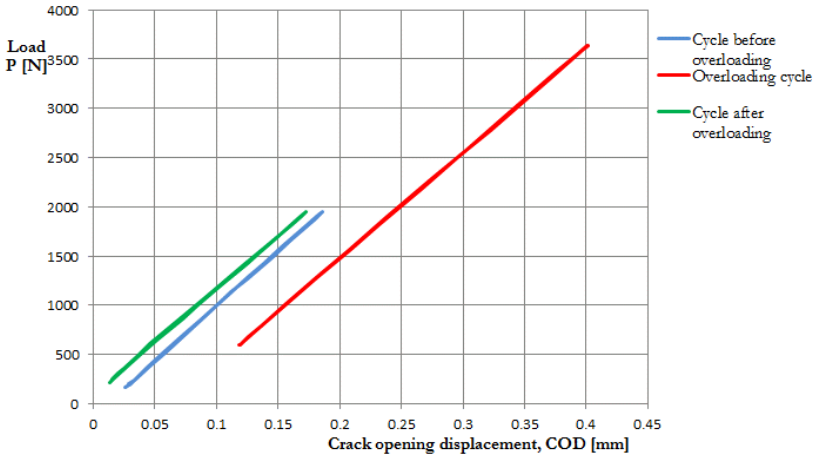

b)

Fig. 2.41. The variation curves of load vs. COD for: a) 26%$P_{max,CA}$ overloading; b) 82%$P_{max,CA}$ overloading

Table 2.9. The crack opening load corresponding to overloading cycles.

Specimen type	Thickness [mm]	Overloading	Overloading crack opening load, $P_{op,OL}$ [N]
CT_overload26%	2.42	$26\%P_{max,CA}$	1950
CT_overload82%	2.43	$82\%P_{max,CA}$	2400

In the first case of overloading, the value of $P_{op,OL}$ is less than the maximum force of constant amplitude loading. This made possible tracking by compliance technique the fatigue crack propagation in the plastic zone and respectively was able to determine the fatigue crack growth rate on the retardation zone given by the overloading cycle, fig. 2.40.a. Instead, in the second case of overloading the value of $P_{op,OL}$ is greater than the maximum force of constant amplitude loading and therefore the compliance technique could not detect the crack extension in the plastic zone, fig. 2.40.b. Meanwhile, in both cases the fatigue crack continued to propagate in the plastic zone but with a propagation character totally changed from the propagation mode in front of the overloading, fig. 2.42-2.43.

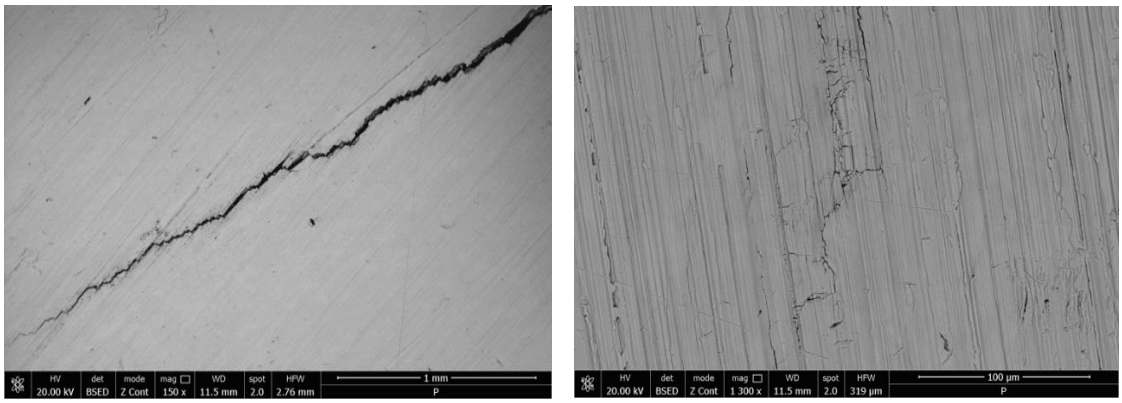

a) b)

Fig. 2.42. The fatigue crack propagation in sample overloaded with $26\%P_{max,CA}$: a) before overloading; b) after overloading, [120]

The fatigue crack propagation in plastic zone was guided by a dislocation crack tip shielding mechanism characterized by branching and interlocking of the crack tip.

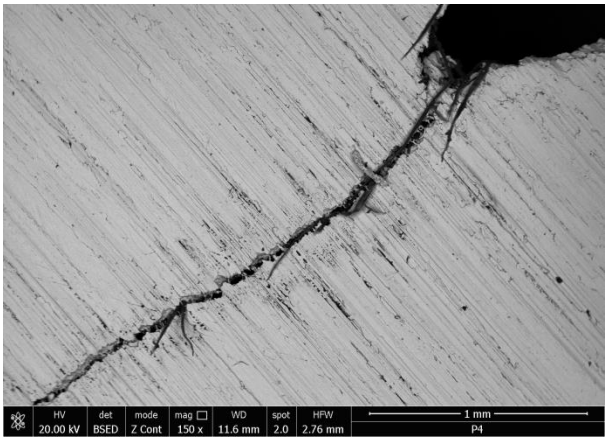

a)

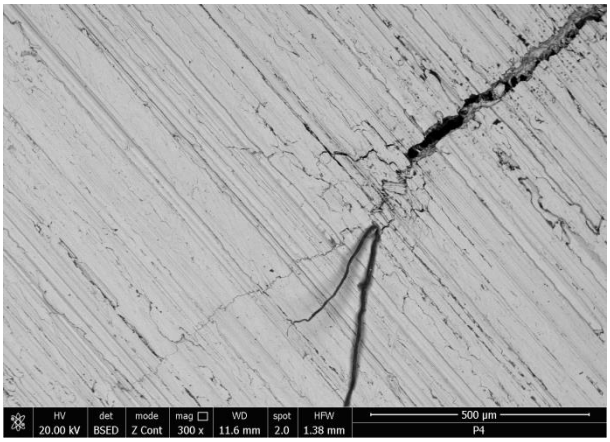

b)

Fig. 2.43. The fatigue crack propagation in sample overloaded with 82%$P_{max,CA}$: a) before overloading; b) after overloading, [120]

This study presents an experimental analysis of fatigue crack propagation in elastic-plastic material. Is pursued in particular the character of crack propagation in terms of crack tip shielding mechanisms occurring or that may occur under certain conditions of crack growth. It is obvious that a change in material behaviour (introducing a plastic zone) it falls upon the crack propagation by changing the crack tip shielding mechanisms. The results also indicate that in the plastic zone the dominant mechanism is dislocation crack tip shielding. In plane strain condition this mechanism is characterized by interlocking effects of the crack. For plane stress the dislocation crack tip shielding mechanism is manifested by branching and interlocks giving more tortuous character of the crack path. In relation to plasticity induced crack closure this mechanism can be considered as an active process that could help the crack extension even if the crack tip is shielded.

Returning to description of Elber about the loading effect on fatigue crack growth and which say that the crack is fully open only for a part of the loading cycle characterized by ΔK_{eff}, then what might happen on the portion between the minimum and opening load? Could this variation to trigger crack tip shielding mechanisms, considering that the crack is surrounded by a plastic deformation field?

The results of this study indicate that the variation $P_{op} - P_{min}$ could determine crack tip shielding mechanisms if P_{op} is high enough. This can be met in the area with severe plastic deformations such as those introduced by overloading.

2.4. Fatigue of overhead power line conductors

The overhead power lines, characterized by large bearings lengths, high flexibility and continuous wind exposure are susceptible to oscillations caused by the interactions between wind and high voltage conductors.

Wind vibrations can cause fatigue failure of wire conductors. Such failures generally occur within couplings (e.g. suspension clamps) that restrict the conductor vibration, [121]. The fatigue damage mechanisms of conductors in these areas are similar to fretting fatigue phenomenon. Fretting is the oscillatory sliding motion of small "slip" amplitude between two contacting surfaces and it is promoted by high-frequency and low-amplitude vibratory motion. Because this phenomenon resulted in fatigue life reduction of components exposed, the term of fretting was associated with fatigue, resulting the generally accepted term of *fretting fatigue* [122].

In the clamping area of conductor (e.g. suspension clamp) the contact stresses can be divided in two categories: static and cyclic. The static stress is given by a summation of a constant axial stress (span weight), a bending stress (change in curvature over the clamp), a local clamping pressure and keeper pressure, [123]. The external tension of conductor determines an internal torque that tends to tighten or relax its wires depending on the variations of external tension (e.g. temperature change causing expansion or contraction of the conductor). The torque is also transmitted in the support of conductor. Thus, the relative movement of the wires in the suspension clamp superimposed with the clamping force activates the damage mechanisms of wires by fretting fatigue. In addition, the reverse bending of conductor caused by wind induces alternating bending stresses near clamps.

As was mentioned, the overhead lines are exposed to wind-induced vibrations, and these are manifested in two ways, [123]:

- *Aeolian vibration* (vortex shedding) – caused by wind blowing over individual conductors, which induces high frequency vibration (between 10 and 40 Hz) due to the creation of vortices downstream of the conductor, promoting alternating bending stresses.
- *Sub-conductor oscillation* (wake-induced vibrations) – caused by wind-induced instabilities downstream of the conductor.

Since the suspension clamp is the critical area of the fatigue damage of the overhead line conductors, the evaluation of the stress state in this area is absolutely necessary. However, the determination of fatigue inducing stresses at the contact between individual wires and respectively between the external wires and the clamp surface cannot be done by direct measurement and even numerical evaluations are not easy to achieve due to the internal complexity of the mechanics of conductor. Therefore, a semi-empirical formula is used that correlates the vertical displacement amplitudes of the conductor with stresses in the aluminum wires of the conductor outer layer. This is known as Poffenberger-Swart formula and it is derived from Euler-Bernoulli beam theory considering that the conductor works as a fixed cantilever beam under tension with a vertical displacement at the free edge, [124, 125]. The equation is given as:

$$\sigma_a = K \cdot Y_b \tag{2.37}$$

where σ_a is the dynamic bending stress amplitude; Y_b is the conductors's vertical displacement amplitude, fig. 2.44.

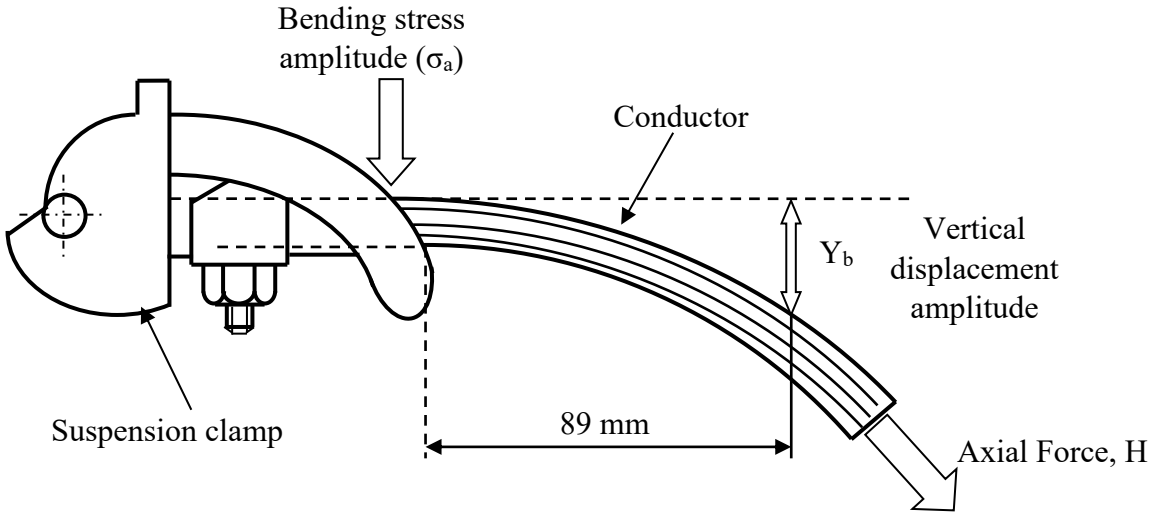

Fig. 2.44. Suspension clamp – conductor assembly and the measuring point of vertical displacement amplitude Y_b

At the IEEE recommendation [126], being universally accepted, the vertical displacement amplitude, Y_b, is measured at 89 mm to the last contact point of the conductor with the suspension clamp, fig. 2.44.

$$K = \frac{E_a \cdot d \cdot p^2}{4\left(e^{-px} - 1 + px\right)} \text{ [N/mm}^3\text{]} \tag{2.38}$$

where E_a is the Young's modulus (MPa) of aluminium, d is the diameter (mm) of an aluminium wire in the outer layer, x is the distance on the cable between the last point of contact between conductor and clamp and the vertical displacement measuring point.

$$p = \sqrt{\frac{H}{EI}} \tag{2.39}$$

where H is the axial tension of conductor, [N], EI is the flexural stiffness (Nmm^2) of the conductor:

$$EI_{\min} = n_a E_a \frac{\pi d_a^4}{64} + n_s E_s \frac{\pi d_s^4}{64} \tag{2.40}$$

where n_a, E_a and d_a are the number, the individual diameter and Young's modulus of the aluminium wires, while n_s, E_s, and d_s are the respective values for the steel wires.

In these circumstances the durability and respectively fatigue strength of the conductor can be analysed and evaluated based on both the bending stress amplitude as well as the amplitude of vertical displacement of the conductor, function of the number of loading cycles.

For practical reasons but also for the precision of determining the amplitude of vertical displacement of the conductor, most of the studies for analysis and evaluation of fatigue life of conductors are based on fatigue curves in Y_b – N coordinates, [123, 127, 128, 129 and 130]. Further, using equation (2.37) can also switch to σ_a – N coordinates.

In general, these curves are developed similarly to Wohler fatigue curves. Conductors are tested for a prescribed tensile pre-load and respectively prescribed value of vertical displacement amplitude of the conductor, until it is detected the first wire failure or 10 % of the total number of aluminium wires of the conductors broken [131]. The displacement amplitude of the conductor is controlled by measuring peak to peak displacement, using laser sensors or accelerometers positioned at 89 mm to the last point of contact between the conductor and clamp.

Fatigue tests on 122-AL1/20-ST1A ACSR conductor with 26 aluminium wires arranged in two layers (16 wires in exterior layer and 10 in the interior layer) and respectively 7 steel

wires, have been performed in the Strength of Materials Laboratory from Mechanics and Strength of Materials Department, [132].

The fatigue tests were done for constant values of the displacement amplitude, Y_b, on samples of conductor mounted on a testing machine that at the one end is provided with a tensioning system and at the other end there is a sensor for axial force measurement. The conductor is passed through suspension clamps and respectively fixed on the testing equipment, fig. 2.45.

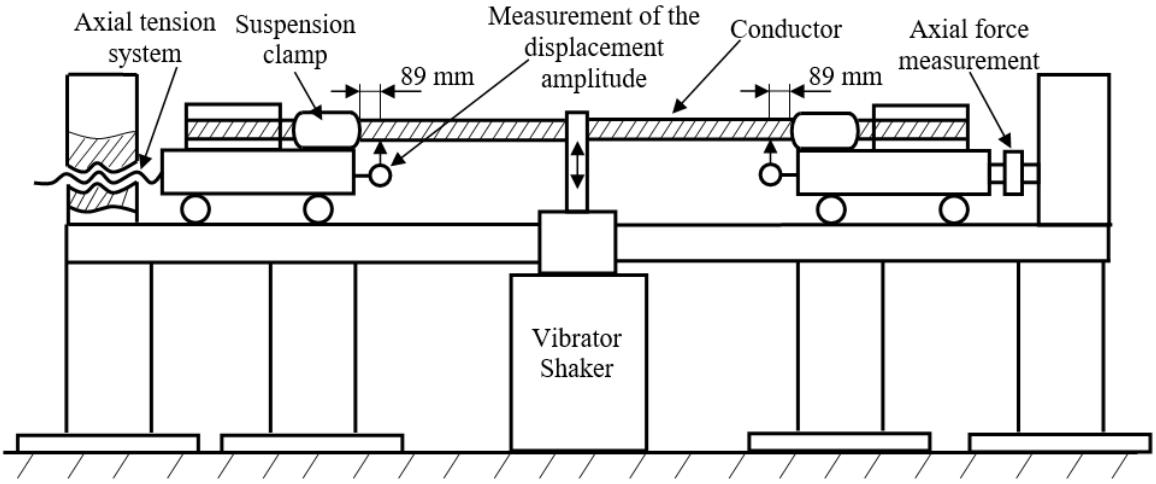

Fig. 2.45. The configuration of fretting fatigue tests of overhead conductors, [132]

A vibrator (shaker – fig. 2.45) is placed on the active span of the sample that induce the vibratory motion to the conductor. The position of shaker is set to obtain the established displacement amplitude, Y_b, in the section of 89 mm to the last contact point between the conductor and clamp. The test procedure starts by applying a pre-load of 10% to 20% of RTS (Rated Tensile Strength) to the conductor. After the load application, the screws of the suspension clamp are tight with a tightening torque which depends on the suspension clamp type and respectively on the axial force from the conductor. Further it is installed the measuring system of the displacement amplitude and the actual test can starts.

During the fatigue tests, the conductor was preloaded with an axial force of 7 kN. The active length of the conductor was 12 m and by positioning the vibrator at different distances from one end of the conductor there was obtained different displacement amplitudes in the section of 89 mm, fig. 2.46. The displacement amplitude of the conductor in the section of 89 mm was recorded with an accelerometer mounted on the conductor, fig. 2.47.

Fig. 2.46. The configuration of the fatigue test of 122-AL1/20-ST1A ACSR conductor

Fig. 2.47. The accelerometer mounted on the conductor for the displacement amplitude recording

The fatigue tests were stopped when the first three aluminum wires broke and respectively the number of cycles at that moment was recorded. Also, the experimental results were represented in semi-logarithmic σ_a – N coordinates, resulting in the fatigue curve of the tested conductor, fig. 2.48.

The analysis of the contact areas between the conductor and the support clamp indicated the presence of some prints as a result of delamination generated by fretting wear, fig. 2.49. Also, the stress concentration effect generated by delamination made fatigue cracks to initiate in

these areas characterized by particle detachments (Al oxides, Al_2O_3), fig. 2.50. The fracture analysis of aluminum wires revealed a V-type fracture topology.

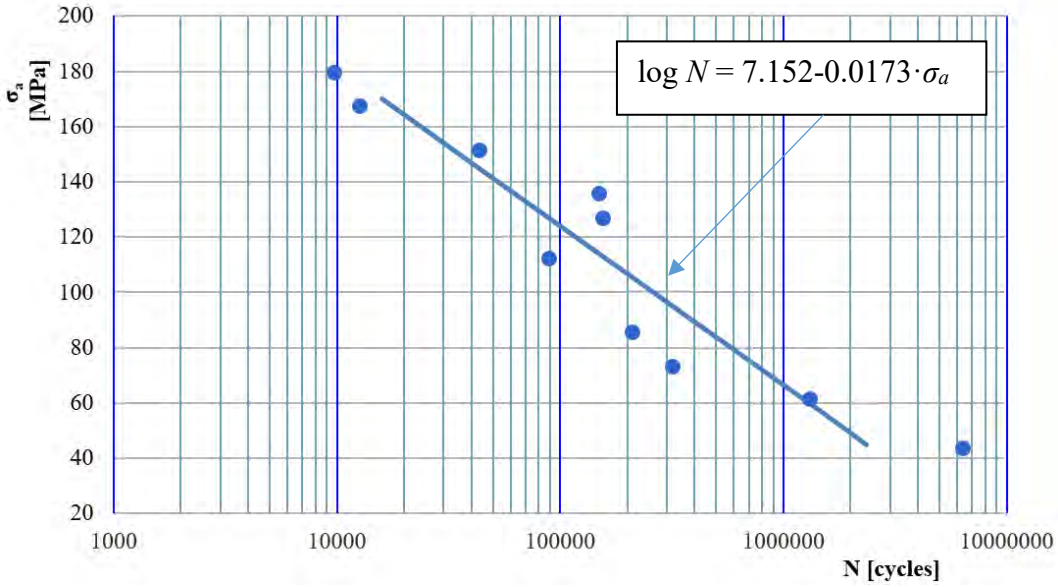

Fig. 2.48. The fatigue curve of 122-AL1/20-ST1A ACSR conductor, [132]

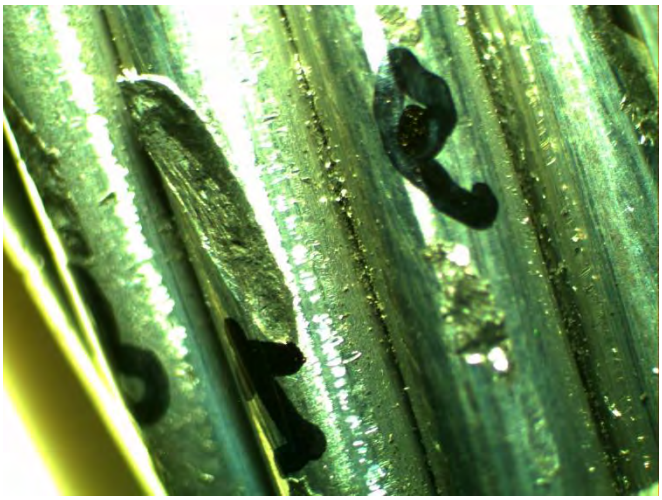

Fig. 2.49. Damage on the aluminum wire surface in contact with the support clamp (particles detachment by delamination)

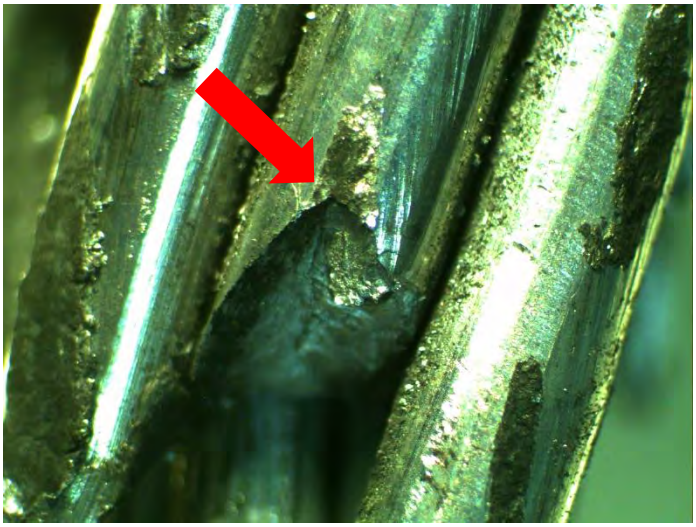

Fig. 2.50. The failure section of a wire with crack initiation in the fretting area

Based on the fatigue curve, predictions can be made on the lifetime of 122-AL1/20-ST1A ACSR conductor subjected to variable amplitude loadings, [132].

2.5. The analysis of a damaged component from the connection system of the wagons

Railways wagons are some of the most important means for passengers and cargo transporting. The couplings bind the railway wagons together to form an entity named the train. In the longitudinal movement of the trains, the couplings have an important role in connecting adjacent wagons and the locomotive, while allowing the transmission of the locomotive traction force on the axial direction. Besides the above condition the couplings must allow relative movements between wagons both in the vertical direction, produced by each wagon suspensions and horizontally determined by the raceway. In addition, in some cases these must allow a rotation movement around of its own axis. Another requirement imposed to the couplings lie in its ability to cushion the shocks received by the wagons. Operational safety of the wagon couplings depends primarily on their ability to resist at the tensile and compression dynamic forces generated by the propulsion or braking of the train. The increase in tonnage and velocity simultaneously with changing the forces that acts on the couplings lead to a reduction of durability of wagon couplings due to the failure of some components [133 – 140]. On the other hand, the high density of the micro-defects in the materials structure of the coupling systems components and poor quality of the surfaces, especially in critical areas, are also causes of fatigue damage of the coupling systems [137]. This research presents a failure analysis of a wagon coupling from a passenger train with nine wagons and hauled by a diesel electric locomotive. The coupling failure was caused by the

fracture of a link plate due to the initiation and propagation of a fatigue crack. The presented study consists of an analysis of the fracture surface and the mechanical properties of the link material, followed by an analysis of the wagon coupling loadings during the movement and a FEM - BEM analysis of the failed component. However, the study was hampered by the neglecting of the fracture surface, which leads to its
oxidation.

In most passenger trains from the CFR Park (Rumanian Railways National Company) are used couplings with screw and draw hook, Fig. 2.51.

The coupling system with screw and draw hook consists of two links mounted on the traction hook, two threaded nuts, a screw and shackle. All parts of the coupling are made of quality carbon steel in enhanced condition (normalized). Also, these components are subjected to heat treatment of hardening and tempered to obtain the mechanical characteristics specified in standard prescription UIC 826 OR, [141], Table 2.10.

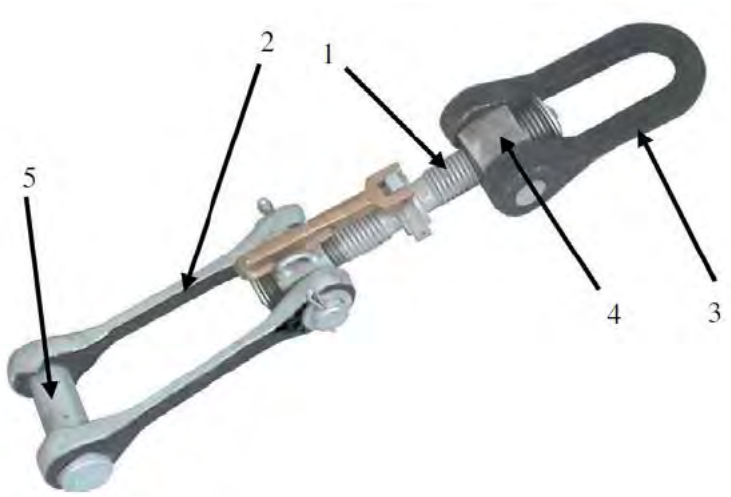

Fig. 2.51. The wagon coupling system with screw and draw hook, [152]

The components of the wagon coupling system are grouped into homogeneous lots composed of pieces from the same production charge, to which has been applied the same heat treatment. Also, the couplings are grouped in lots of 200 pieces. All couplings from a lot are composed of components made from the same batch of the material.

Table 2.10. The components of the coupling system according to UIC 825 OR standard

The components	**Material**	**The heat treatment**	**The product standard**	**Yield Strength [MPa]**	**Ultimate tensile Strength [MPa]**	**Elongation A [%]**
The screw 1 – fig. 2.51	41Cr4	Hardened and tempered	SR EN 10083-1	560	800/950	14
	42CrMo4			650	900/1100	12
The coupling shoe lining, 2 – fig. 2.51	41Cr4	Hardened and tempered	SR EN 10083-1	560	800/950	14
The hitch, 3 – fig. 2.51	42CrMo4	Hardened and tempered	SR EN 10083-1	650	900/1100	12
The threated nuts, 4 – fig. 2.51	42CrMo4	Hardened and tempered	SR EN 10083-1	650	900/1100	12
	41Cr4	Hardened and tempered	SR EN 10083-1	560	800/950	14
Bolt, 5 – fig. 2.51	41Cr4	Hardened and tempered	SR EN 10083-1	560	800/950	14
	42CrMo4	Hardened and tempered		650	900/1100	12

During traveling from Timisoara to Baia Mare, IR 1743 passenger train was stopped due to the failure of a coupling, Fig. 2.52. In this case, the failure not caused material damages, due to the dynamic breaking system of the wagons, but resulted in delayed trains on that route for an extended period.

The conclusion of the Railway Traffic Safety specialists was that the coupling failure was caused by the fracture of a link. The fracture was determined by the initiation and propagation of a fatigue crack, Fig. 2.53.

From the first observations was established that the coupling was broken after about 5 years. Moreover, the coupling was mounted on a wagon that in the period of 5 years has run about 1,354,150 km. Unfortunately, there are no studies or documentations that highlights the fatigue limit of this type of couplings. However, comparing the number of kilometres covered by the wagon with the analysis performed by Cole and Sun, [137], on the fatigue limit of couplings from the heavy haul trains was considered that the analysed coupling failed before the operational use limit.

Fig. 2.52. The failure of a wagon coupling from a passenger train

Fig. 2.53. The fracture surface of the connection shoe lining, due to the initiation and propagation of a fatigue crack

2.5.1. The mechanical properties of the link material

For the evaluation of the mechanical properties, material samples were taken from the remaining link and other three couplings from the same lot with that was failed.

The experimental test results on the sampled material were compared with the mechanical properties of the material specified in the UIC 826 standard prescription, for the execution of the failed component (Table 2.10).

In Table 2.11 are given the results of chemical analysis performed on the sampled material, compared with the standard prescriptions.

Table 2.11. The chemical composition of the sampled material

Material	C [%]	Mn [%]	Cr [%]	S [%]	P [%]	Others [%]
The coupling shoe lining material	0.286	0.596	0.118	0.0162	0.0701	Cu – 0.103 Fe – 98.31
41Cr4 SR EN 10083-1/95	0.38 – 0.45	0.6 – 0.9	0.9 – 1.2	max. 0.035	max. 0.035	Si – max. 0.4

Tensile tests were performed on the sampled material, according to SR EN 10002–1, [142] and the results are given in Table 2.12.

Considering that the coupling is subjected to dynamic loads during the train movement, it is necessary to determine the fracture impact energy of the material from which the broken component is made. In order, resilience tests have been performed on V-notch samples with cross-sectional dimensions of 10 x 10 mm, based on which was determined the Charpy impact energy at the temperature of 24 °C. The tests have been carried out according to SR EN ISO 148–1, [143], Table 2.13.

After evaluation of the mechanical behaviour of the sampled material a first observation could be made on the failure analysis of the coupling component. There is a difference between chemical composition and mechanical properties of the tested material and the materials prescribed in UIC standards for the execution of couplings connection. The chemical composition indicate a Low Carbon Steel – AISI 1025 and probably due to the heat

treatment and/or that the component is made by forging, the mechanical properties are higher than the usual AISI 1025 steel, cold drawn high temperature, [144, 145].

Table 2.12. The mechanical properties of the material

Material	Yield Strength [MPa]	Ultimate Tensile Strength [MPa]	Elongation [%]
The coupling shoe lining material	539.12	895.5	9.6
41Cr4 SR EN 10083-1/95	560	800/950	14

Table 2.13. The Charpy impact energy of the material, according to SR EN ISO 148-1

Material	Charpy Impact Energy, CV [J]
	T = 24 °C
The coupling shoe lining material	61

2.5.2. The analysis of the fracture surface

The analysis of the fracture surface was difficult due to its oxidation and loss of some information about the fatigue crack propagation. However, the fracture surface was carefully cleaned and examined with a Hirox optical microscope. After the initial examination, some striations were observed indicating the area from which the fatigue crack was initiated, Fig. 2.54.a and b. Based on microscope examination it was observed that the fatigue crack initiation was caused by the existence of a structural defect in material, very close to the lateral edge of the section, Fig. 2.55. The initial defect that formed the crack is on the type of a void resulted from casting of material. Normally this would be detected on ultrasound control. The defect size was found by measuring the diameter in the plane of fracture surface, Fig. 2.55, (d = 0.73 mm), and the computed area A_d = 0.422 mm^2. The defect size is given by the square root of the area in the plane of fracture section.

– Total area of the section: $A_t = 14 \times 40 = 560$ mm^2;

– The surface fracture by fatigue: $A_c = 560 - [(22 + 18) \times 14]/2 = 280$ mm^2;

– The critical crack size: $a_c = \sqrt{A_c} = 16.733$ mm.

Analysing the fracture surface at 200 times magnification, it was possible highlighting in detail the striations, thus establishing the distance between them in different areas of the fatigue fracture, Fig. 2.56.

Based on micrographic analysis, the fracture surface was divided into three regions, Fig. 2.57, for each region was estimated a size limit and an average distance between striations, such as:

– *Region I* – the limit of the crack size was about 7.976 mm and the average distance was $2 \cdot 10^{-3}$ mm;

– *Region II* – the limit of the crack size was about 13.468 mm and the average distance was $6 \cdot 10^{-3}$ mm;

– *Region III* – the limit of the crack size was about 16.733 mm and the average distance was $5 \cdot 10^{-2}$ mm;

At the same time, based on this analysis was done an estimation of the fatigue crack propagation curve, Fig. 2.58.

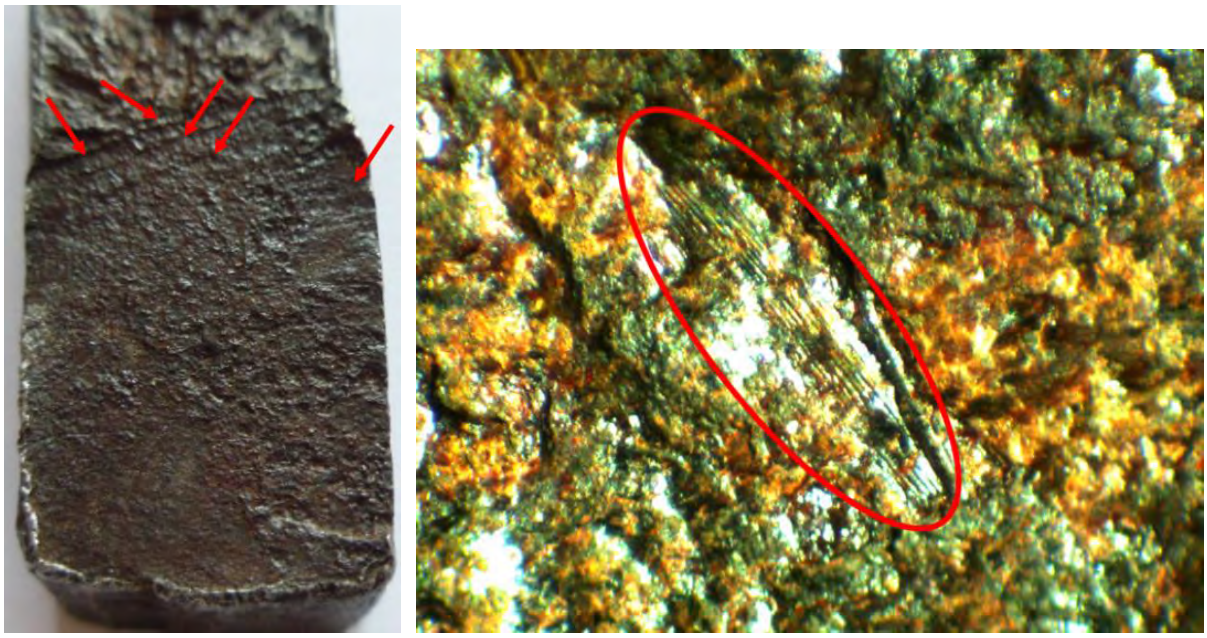

a) b)

Fig. 2.54. The fracture surface of the damaged component: (a) the striations which indicates the area damaged by fatigue crack propagation; (b) striations on the failed surface – 5x magnifications

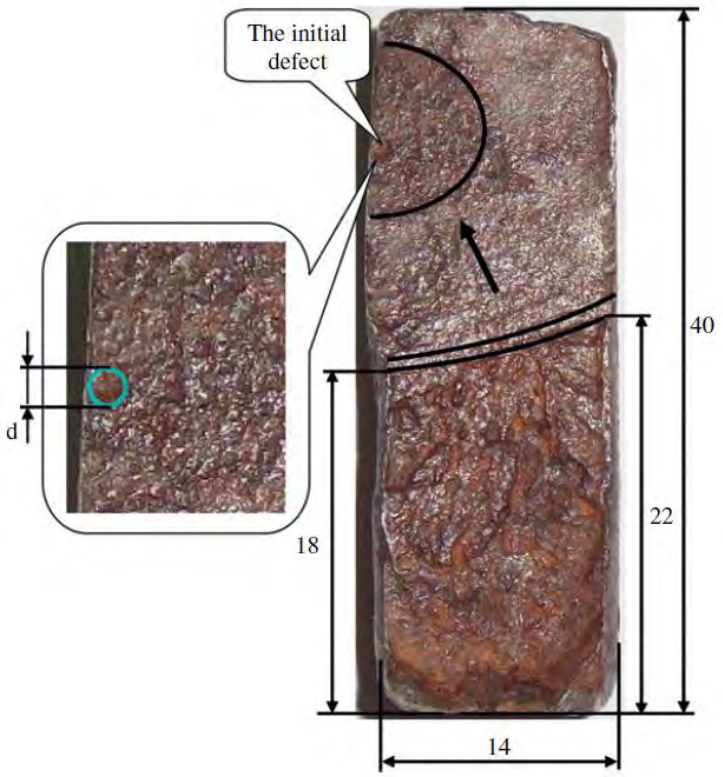

Fig. 2.55. The initial defect location and the size of fracture section (d – the defect diameter in the plane of fracture section).

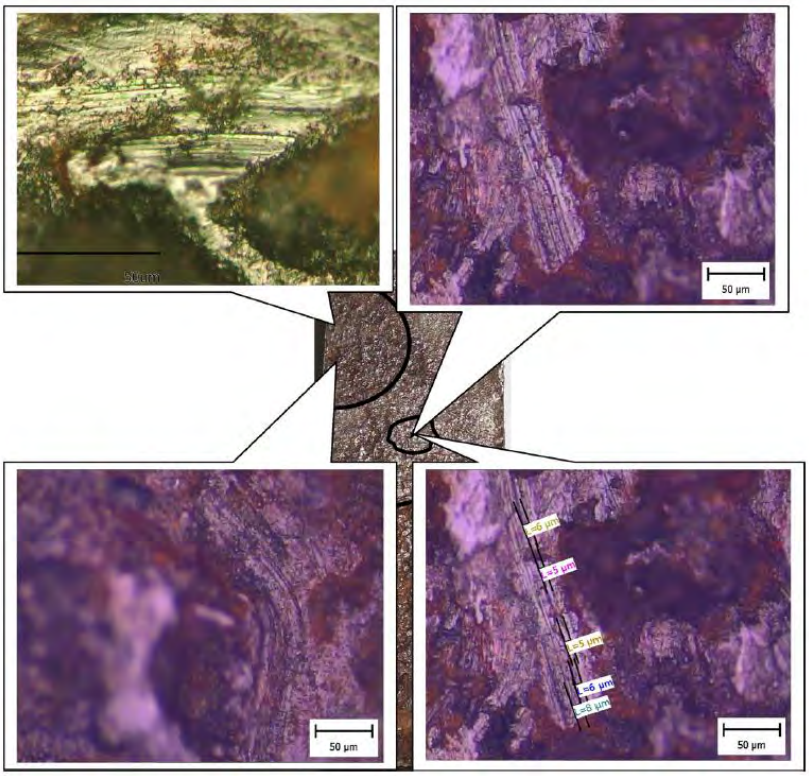

Fig. 2.56. Micrographic analysis of the fracture surface.

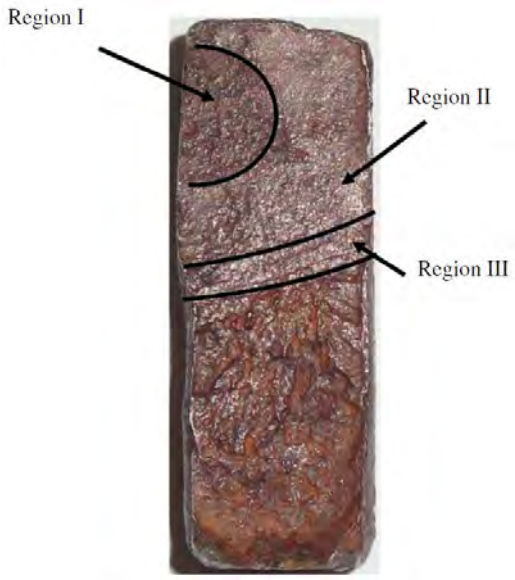

Fig. 2.57. Dividing the surface fracture by fatigue in three regions.

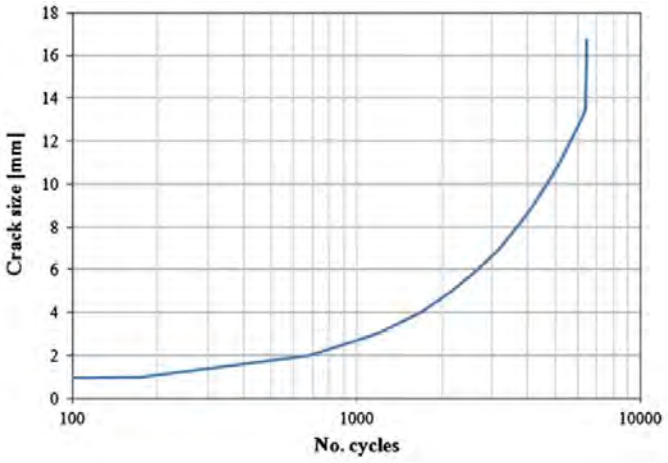

Fig. 2.58. The fatigue crack propagation curve.

2.5.3. The modelling of the wagons coupling system and the longitudinal train dynamics

To determine de loading level of the coupling on the move was made a longitudinal modelling of the train after a model proposed by Colin, [137, 146].

The longitudinal behaviour of trains is a function of train control inputs from the locomotive, train brake inputs, track topography, track curvature, rolling stock and bogie characteristics, and wagon connection characteristics. Also, this behaviour of a train can be described by a system of differential equations. For the purposes of setting up the equations, modelling, and simulation, it is usually assumed that there is no lateral or vertical movement of the wagons.

For the analysed case, the longitudinal dynamic behaviour of the train was made tacking into account the technical characteristics of the wagons and the locomotive Table 2.14, and respectively the movement diagram of the train on the route that the coupling failure occurred, Fig. 2.60. In the movement diagram is represented the locomotive velocity variation over time.

For the analysis performed was considered that a loading cycle is equivalent to an acceleration of the locomotive, when the velocity increases from 0 to 60 km/h. Thus, on the diagram were counted about 200 of such accelerations.

Therefore, the equations are:

$$\begin{cases} m_1 a_1 + C_1(v_1 - v_2) + K_1^-(x_1 - x_2) = F_{t/db} - F_{r1} - F_{g1} \\ m_2 a_2 + C_1(v_2 - v_1) + C_2(v_2 - v_3) + K_1^-(x_2 - x_1) + K_2^-(x_2 - x_3) = -F_{r2} - F_{g2} \\ .... \\ m_{10} a_{10} + C_9(v_{10} - v_9) + K_9^-(x_{10} - x_9) = -F_{r9} - F_{g9} \end{cases} \quad (2.41)$$

where $F_{t/db}$ is the traction and dynamic braking force of the locomotive; F_r is the amount of resistant forces, [146]; F_g is the gravitational force caused by the runway slope; k is the proportionality factor of the coupling system; m_i – (i = 1, 2. . .10) is the wagon weight; a_i – (I = 1, 2. . .10) is the wagon acceleration; v_i – (i = 1, 2. . .10) is the wagon velocity; C_i – (i = 1, 2. . .10) is the Damping constant.

In Fig. 2.59 is outlined the train with those nine wagons, being indicated the position of each wagon by a reference point at time t = 0 s.

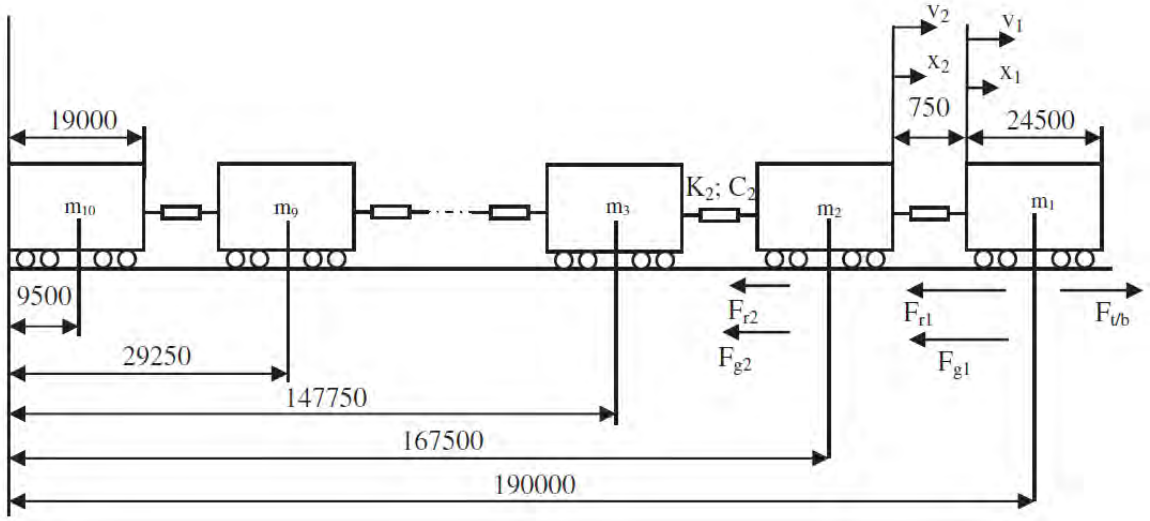

Fig. 2.59. Schematization of the train with nine wagons (units: mm).

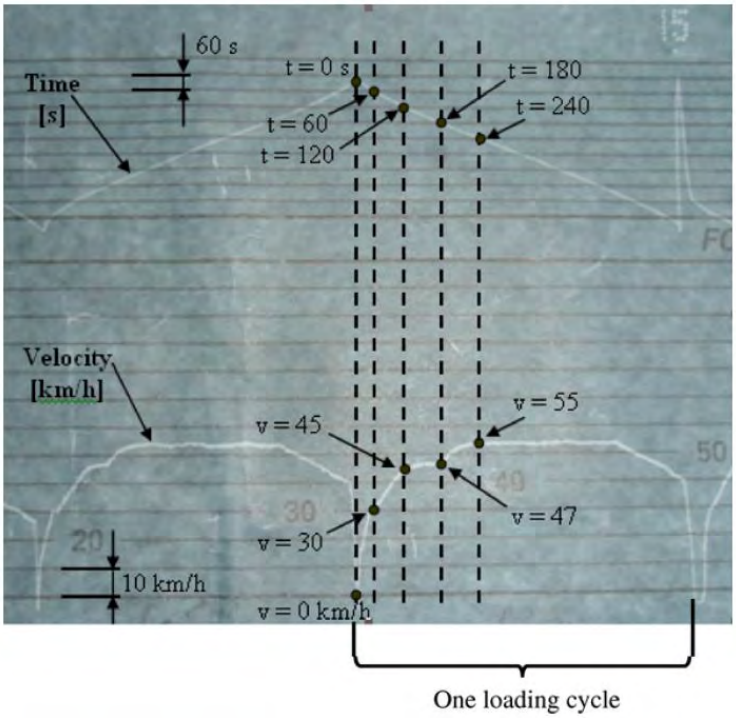

Fig. 2.60. The movement diagram of the train: at time t = 0 s, the locomotive speed is 0 km/h, after 60 s the speed increases to 30 km/h, at t = 120 s the locomotive speed is 45 km/h and so on.

Table 2.14. Technical characteristics of the train vehicles

Technical characteristics	**The locomotive**	**Wagon**
Type of vehicle	LDE 3000 HP	Corail – AVA-200
The weight of vehicle	120 t	41 t
The weight per axle	20.5 t	16 t
The length of vehicles	24500 mm	19000 mm
The maximum starting force	350 kN	-
The maximum continuous traction force	238 kN	-
The maximum velocity	140 km/h	140 km/h

To solve the movement equations (2.41) of the train, the proportionality constant of the coupling system, *k*, need to be determined. The wagon coupling system with screw and hitch can take loading only at the traction phase, while at compression, resulted from the braking or decelerations, the loading is taken by the dampers mounted on the wagons.

The wagon couplings can be described by a resort type model, Fig. 2.61, in which the loading force of the coupling is a function of the displacement, Δx, between two adjacent wagons:

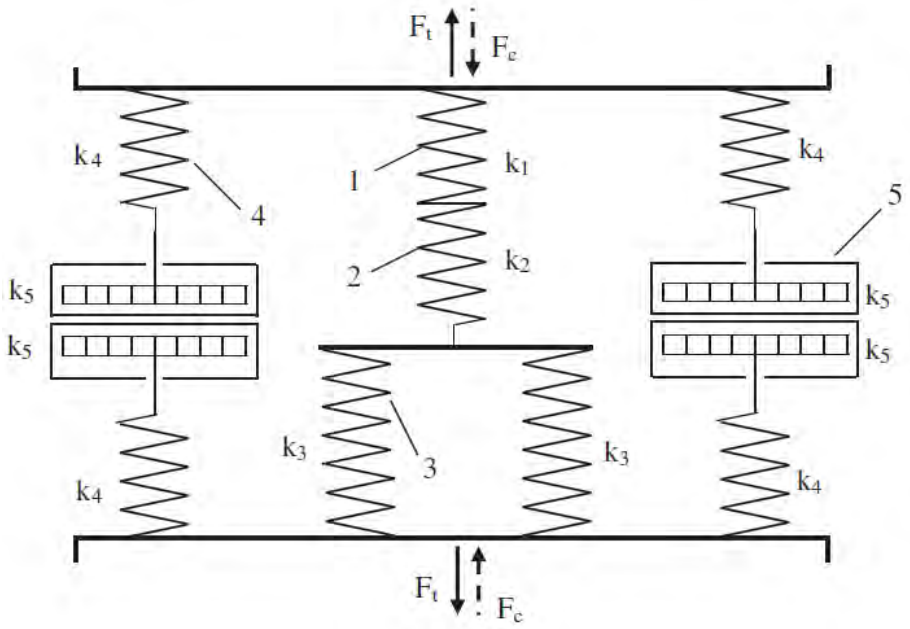

Fig. 2.61. Rheological model of the wagon coupling connection: 1 – the shackle; 2 – the screw; 3 – the link; 4 – elastic element; 5 – the dampers.

$$f(\Delta x) = k \cdot \Delta x \tag{2.42}$$

where *k* is the proportionality factor for a perfect resort.

In some cases, *k* can have a nonlinear dependence of Δx. Some other authors consider in the expression of coupling forces the damping influence, [137]:

$$f(\Delta v) = C \cdot \Delta v \tag{2.43}$$

For traction:

$$\Delta = \delta_{e1} + \delta_{e2} + \delta_{e3} \tag{2.44}$$

$\delta_{e1} = k_1 F$ - The deformation of the hitch

$\delta_{e2} = k_2 F$ - The deformation of the screw

$\delta_{e3} = k_3 \frac{F}{2}$ - The deformation of the coupling shoe lining

$$kF = k_1 F + k_2 F + k_3 \frac{F}{2}$$

$$k = k_1 + k_2 + \frac{k_3}{2} \tag{2.45}$$

For determining the proportionality constant of the coupling, *k*, tensile tests were performed on a coupling from the same lot as that the link was failure. The tensile tests were performed on a testing machine of 1000 kN, model VEB – Werkstoffpruf maschinen, Leipzig. Due to

excessive length of the coupling, there have been performed tensile tests on the link, Fig. 2.62 and separately on the screw–nuts–shackle assembly, Fig. 2.63.

On each test performed a traction force was applied up to 100 kN recording the corresponding elongations of the components, Fig. 2.64.

The proportionality constant of the coupling was determined by the following relations:

$$k_1 + k_2 = \frac{\Delta F}{\Delta u} = 116250 \text{ N/mm} \tag{2.46}$$

$$k_3 = \frac{\Delta F}{\Delta u} = 62500 \text{ N/mm} \tag{2.47}$$

$$k = k_1 + k_2 + \frac{k_3}{2} = 147500 \text{ N/mm} \tag{2.48}$$

Δu – the elongation of the components.

After all parameters needed to solve the equations were set up, the coupling forces for two cases were determined, when the locomotive accelerates from 0 to 60 km/h, Figs. 2.65 and 2.66.

Fig. 2.62. The tensile test on a link of the coupling.

Fig. 2.63. The tensile tests on the screw – nuts – shackle assembly.

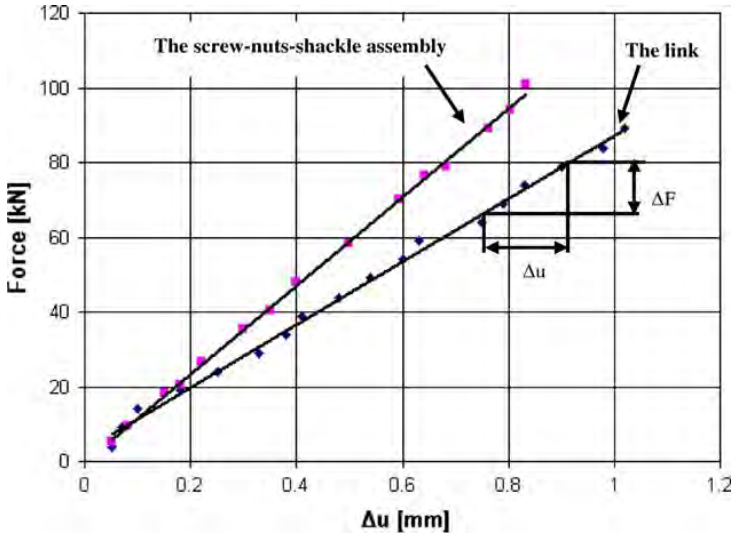

Fig. 2.64. The force–deformation curves of tested components.

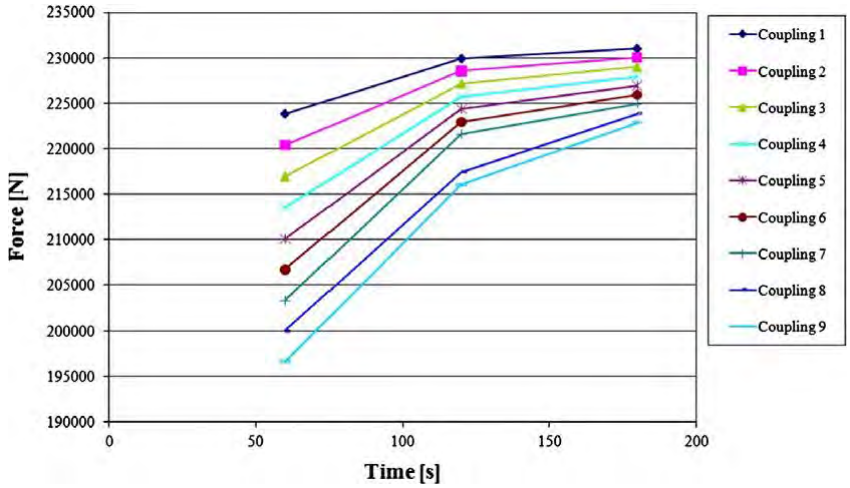

Fig. 2.65. Case I – the coupling forces corresponding to acceleration from 0 to 60 km/h in 180 s.

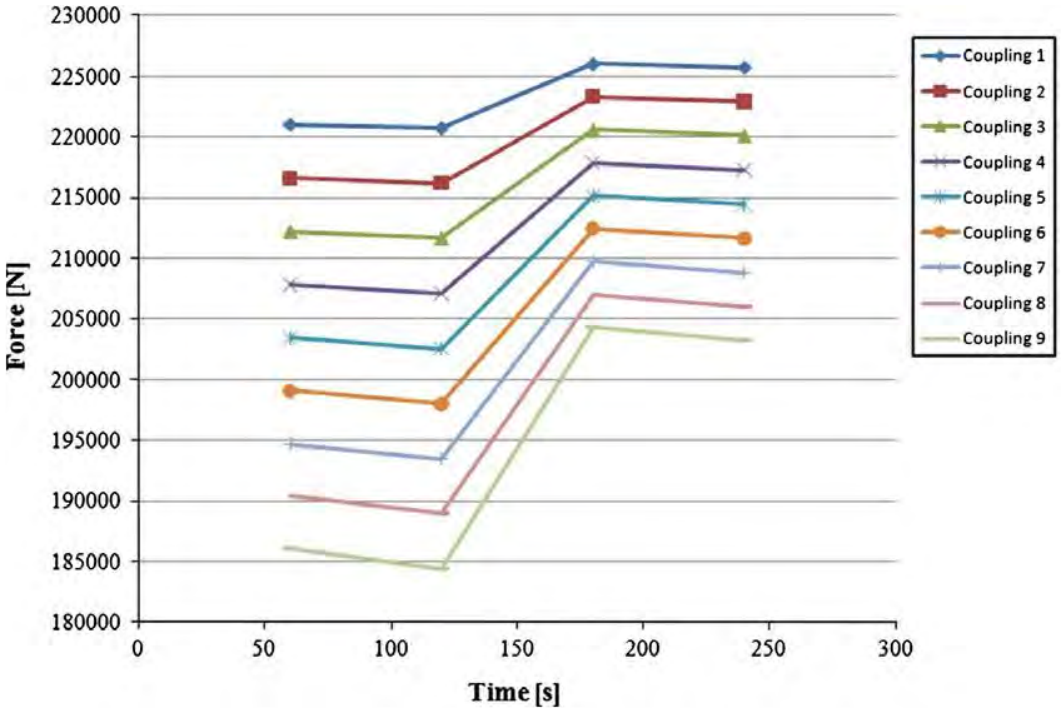

Fig. 2.66. Case II – the coupling forces corresponding to acceleration from 0 to 60 km/h in 240 s.

2.5.4. The numerical analysis of the damaged component

According to UIC 826 OR standard prescription the coupling must withstand to traction force of 350 kN without permanent deformations and a force of 850 kN without cracks or fracture. Considering this, a FEM analysis was performed to determine the stress and strain state of the damaged component for the cases were the coupling would be loaded with 350,000 N force but also with maximum values of the calculated forces for the first five couplings in the train. For numerical analysis, a geometrical model of the coupling was made, that was imported into ANSYS Workbench software version 11, [147]. The model was meshed in tetrahedral finite elements type Solid. Regarding the boundary conditions, was applied a cylindrical support on the bolt which does not allow axial and radial displacement, instead allow the rotation

of the assembly. On the contact surface between shackle and hook was applied a pressure corresponding to the calculated forces, Fig. 2.67.

In Figs. 2.68 – 2.70 are given the normal stress and respectively strain distributions on cross section of the damaged component.

The FEM analysis results show that both the stress and strain states are in the acceptable limits of strength in stiffness of the coupling link material, for the force of 350,000 N. At the

same time, the area with maximum concentration of the normal stress is the lateral edge of the cross section of the link, where the crack initiated, Fig. 2.70.

Also, in Fig. 21 are the maximum values of the normal stress on the cross section of the damaged component, corresponding to the maximum values of the calculated forces in the *case I* for the first five couplings in the train. Based on the coupling forces, determined analytically in *case I*, a BEM analysis was performed, using Franc 3D software version 3.2, [148]. For this analysis was considered a semi-elliptical initial crack with size of 0.65 mm, in the place where the fatigue crack initiated. For different values of the coupling forces, the initial crack size was extended over several steps until reaching the unstable state, Figs. 2.72 and 2.73.

For each extension step were determined the crack surface, the crack front length and respectively the stress intensity factors on the crack front (K_I, K_{II} and K_{III}), [149].

In Fig. 2.74 is represented the equivalent stress intensity factor depending of the crack size, for the force of 350,000 N and respectively 222,859 N. The second value considered represents the maximum calculated force, in *Case I*, for the coupling 9 of the train.

$$K_{eq} = \sqrt{K_I^2 + K_{II}^2 + \frac{K_{III}^2}{1-\nu}} \tag{2.49}$$

where $\nu = 0.3$ is the Poisson's ratio.

It should be noted that in all the performed simulations the force applied on the link is half of the loading force of the coupling.

Also, using the fatigue crack growth module in Franc 3D, was estimated the propagation curve of the crack function of the number of cycles, for the maximum value of the coupling forces. Based on the forces in *Case I*, loading spectra with R = 0 and the maximum forces corresponding to the first five couplings of the train has been defined. The propagation constants were set from the Refs. [150] and [151], ($C = 1.515 \cdot 10^{-14}$ and $n = 3.7$).

The propagation curves determined analytical were compared with that estimated from the analysis of the fracture section.

In Fig. 2.75 are shown the curves of fatigue crack propagation determined analytically for the first five couplings from the train and that estimated on the fracture section. It can be observed that the final stage of the crack propagation, before breaking, is quite close to the crack propagation curve determined for the third coupling from the train. Thus, it can be said that the

loading level of the damaged link before breaking, was similar to the loading level of the coupling 3.

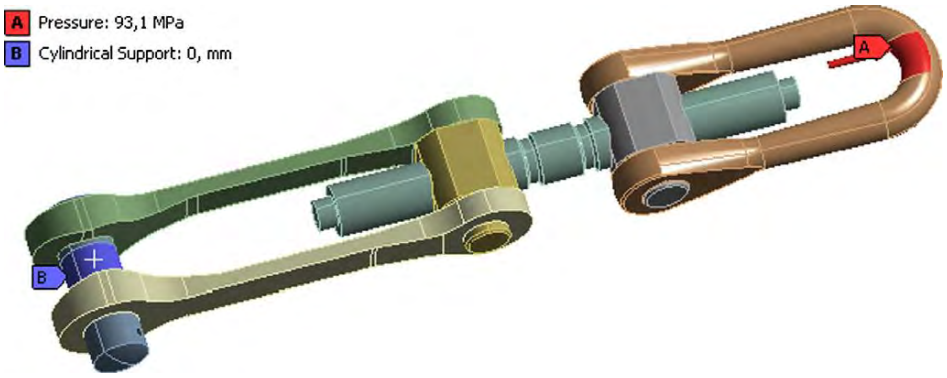

Fig. 2.67. The boundary conditions of the coupling.

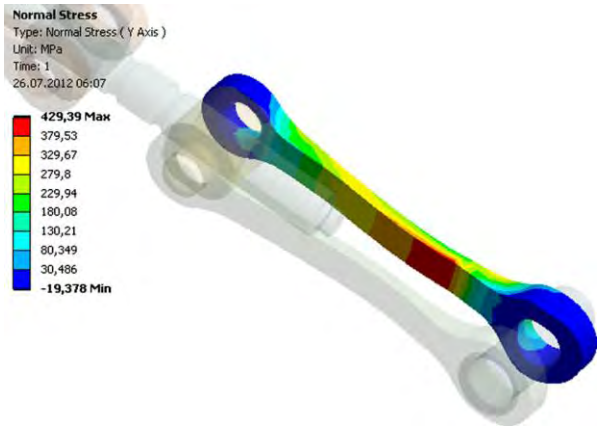

Fig. 2.68. The normal stress distribution in the damaged component for the force of 350,000 N.

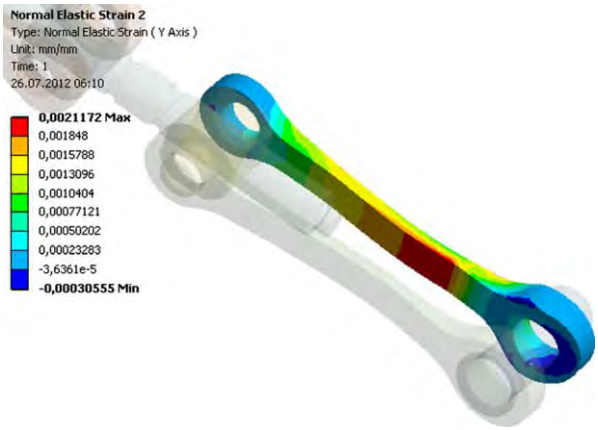

Fig. 2.69. The normal stress distribution in the damaged component for the force of 350,000 N.

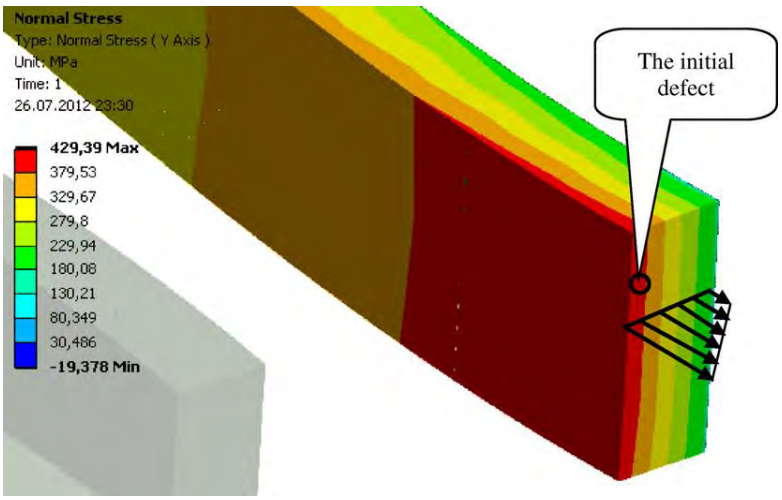

Fig. 2.70. The normal stress distribution on cross section of the damaged component for the force of 350,000 N.

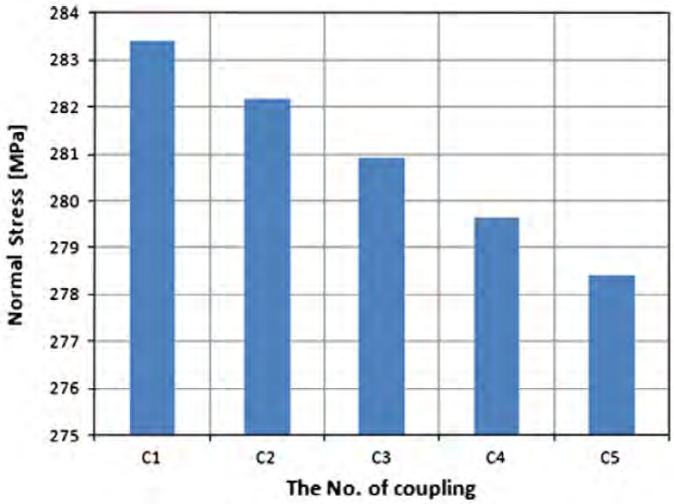

Fig. 2.71. The maximum values of the normal stress on the cross section of the damaged component, for the first five couplings in the train.

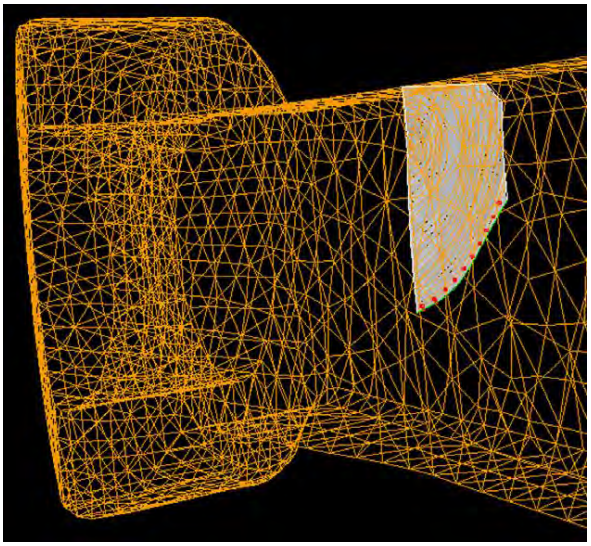

Fig. 2.72. The initial crack extension.

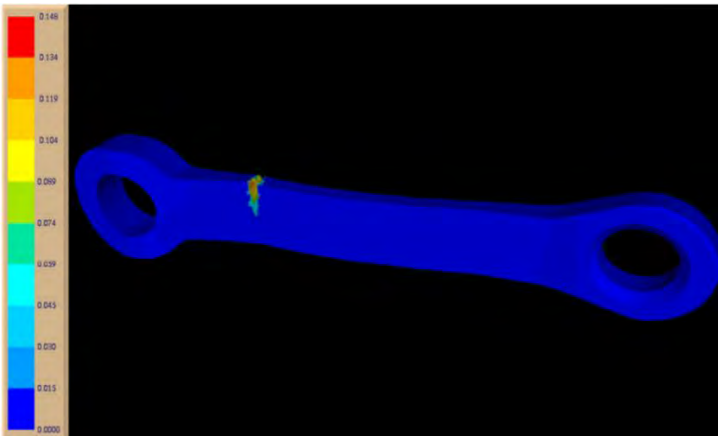

Fig. 2.73. The crack opening displacement corresponding to the unstable crack extension.

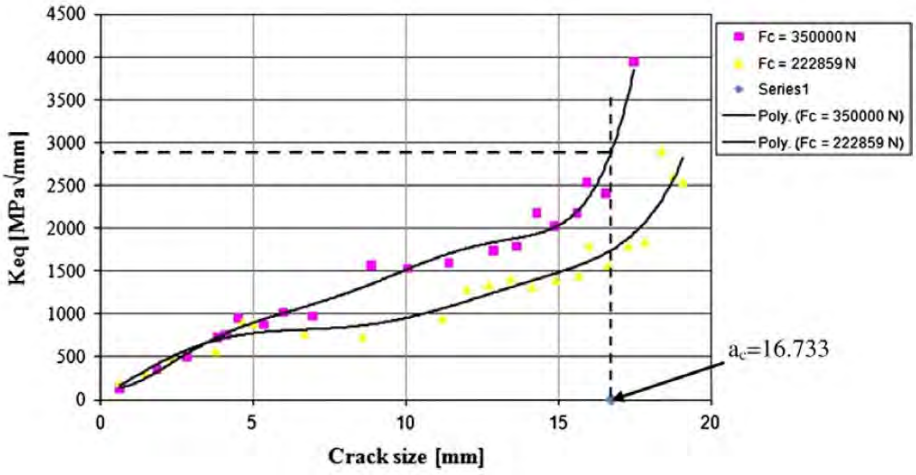

Fig. 2.74. The variation of the equivalent stress intensity factor function of crack size for two loading forces of the coupling.

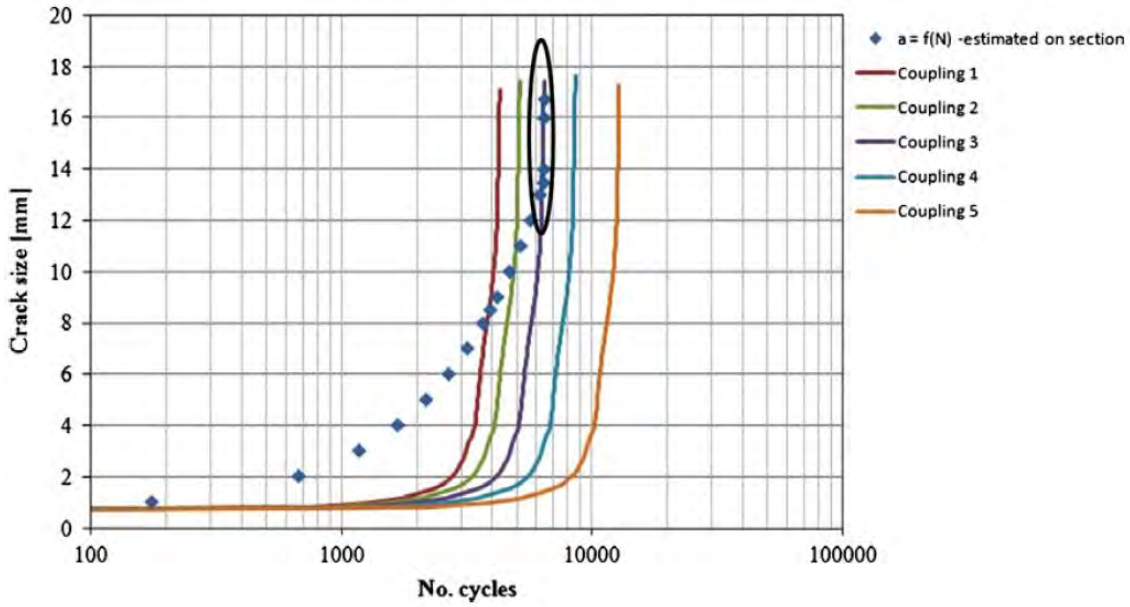

Fig. 2.75. The crack propagation curves corresponding to the first five couplings from the train and that estimated on the fracture section.

The failure of the link was done by the presence of a structural defect that caused the initiation of a fatigue crack. The material of the analysed link is different from that is specified in UIC 826 standard prescription.

The loading force of the damaged coupling was estimated at about 229 kN and the propagation curve estimated on the fracture section is closed to that calculated for the coupling No. 3.

Based on the estimation of the total number of cycles for crack propagation (about 6474 cycles), the number of cycles during one travel (about 200 cycles or accelerations) and the number of the travels per day (1/day), a crack propagation period of about 1 month was calculated. It was concluded that the wagons connection couplings have not been verified in the last month before breaking. Probably, if had been made a visual inspection, the fracture of the link would have been avoided.

The higher degree of loading of the coupling systems, associated with additional shocks and the possible structural defects shows the need for an inspection program of these systems and an improvement of the testing methodology of the couplings.

3. Scientific, professional and academic plans

3.1. Scientific plan

The material fracture has as its incipient phase the failure of atomic bonds that trigger irreversible displacements of atoms in the crystalline network. Therefore, as the research approaches the atomic scale of the materials, the fracture process and respectively fatigue damage is more controlled. On the other hand, moving from a macrostructural scale to the mesoscopic scale and beyond the atomic scale, fig. 3.1, is very difficult. With the transition from one scale to another, the analysis theories must be modified and even developed new theories. The difficulty of conducting mechanical behaviour analysis of materials at reduced scales greatly increases and requires knowledge about the nature of the material at that scale. Experimental evidences also requires advanced technologies.

However, the economic and social impact created by some accidental failures makes all the barriers mentioned (and many other unreported) overcome. Thus, the current research tendency of the mechanical behaviour of materials consists in the evolution of the macrostructural analysis to reduced scales.

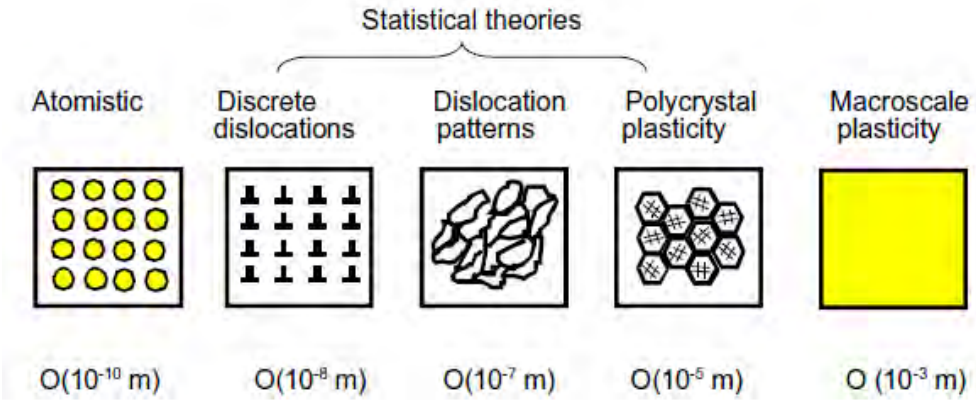

Fig. 3.1. Material analysis scales

3.1.1. Fatigue damage prediction considering microstructural topology

Fatigue failure is a major damage mechanism of structural components and is a global issue due to the aging of structures, new materials, increasing loads and the optimisation design of components. Fatigue damage has both economic and societal impact throughout the world. Inspection programs carried out on railway systems by EU countries, have demonstrated that a significant number of defects are present in the current rail network.

These defects serve as the initiators of fatigue cracks[1, 2]. In the automotive industry, optimizing the weight of mechanical components to improve fuel efficiency and environmental impact is a priority. This however leaves materials in a higher stress state meaning the fatigue performance becomes more crucial[3]. Fatigue is also an issue in the aerospace industry where an original design philosophy is used. It assumes the existence of material defects from an early stage and then assesses the life of a component assuming maximum loading. The lifetime of such a component is determined by the period of initiation and propagation of a fatigue crack from the assumed defect. In terms of energy production, there are demands to reduce the EU reliance on fossil fuels and countries are investing in nuclear energy or extending the life of existing nuclear plants. In these plants, reactor pressure vessels as well as the auxiliary installations are subject to thermo-mechanical fatigue, which can lead to failure, putting lives at risk. By having a detailed understanding of the fatigue damage process, it will be possible to accurately predict remaining life of such components providing a safer more reliable asset. There are many other industries where the prediction and monitoring of fatigue damage is of real interest: shipbuilding, oil and gas, thermal and hydrodynamics power industry.

Fatigue damage occurs in three stages: crack initiation, growth propagation and finally fracture of the component. The first two stages, which cover most of the fatigue life, are dominated by the interaction with the microstructural features of the material[4,5]. Schijve[6] divided the fatigue phenomenon into four periods, micro crack nucleation, micro crack growth, macro crack growth and final failure. Hochhalter et al.[7] developed a comprehensive study of micro crack nucleation within grain boundaries and found that grain orientation has a significant effect on the nucleation metrics. Hoshide and Socie[8] studied the nucleation and propagation of fatigue cracks in biaxial stress loading based on a model that takes into account two cracking modes, shear crack growth and single crack propagation. The shear crack growth mode was evaluated based on the resolved shear stress on the slip plane, while

[1] C.D.G.P. Dias Valente, https://fenix.tecnico.ulisboa.pt/downloadFile/395146408726/resumo.pdf ;
[2] INNOTRACK, http://ec.europa.eu/research/transport/projects/items/innotrack_en.htm ;
[3] A. Morel et al., *Teaching durability in automotive applications using a reliability approach*, International Journal on Interactive Design and Manufacturing, Springer Verlag, 4(4), pp. 281-287, 2010;
[4] P. Hansson, S. Melin, C. Persson, *Computationally efficient modelling of short fatigue crack growth using dislocation formulations*, Engineering Fracture Mechanics, 75 (2008) 3189-3205;
[5] M. Kübbeler, I. Roth, U. Krupp, C.P. Fritzen, H.J. Christ, *Simulation of stage I-crack growth using a hybrid boundary element technique*, Engineering Fracture Mechanics, 78 (2011) 462-468;
[6] Jaap Schijve, *The significance of fatigue crack initiation for predictions of the fatigue limit of specimens and structures*, International Journal of Fatigue, 61: 39-45, 2014;
[7] J.D. Hochhalter, D.J. Littlewood, R.J. Christ Jr., M.G. Veilleux, J.E. Bozek, A.R. Ingraffea, A.M. Maniatty, *A geometrical approach to modeling microstructurally small fatigue crack formation: II. Physically based modeling of microstructure-dependent slip localization and actuation of the crack nucleation mechanism in AA 7075-T651*, Modelling and Simulation in Materials Science and Engineering, 2010;
[8] T. Hoshide, D.F. Socie, *Crack nucleation and growth modeling in biaxial fatigue*, Engineering Fracture Mechanics, 29(3): 287-299, 1988;

the single crack propagation mode was treated by fracture mechanics parameters. Sangid[9] described the physical mechanisms of fatigue crack initiation based on the persistent slip bands which are formed at grain level and cause an accumulation of plastic deformation. The slip always occurs on a particular set of crystallographic planes and directions when the shear stress acting in the slip direction on the slip plane reaches a critical value. This is also known as Schmid's law[10,11].

In most cases, the prediction models for fatigue crack initiation are based on physical damage mechanisms and have been developed and applied on simplified computational models incorporating several grains with well-defined crystallographic characteristics (called Representative Volume Elements – RVE) which are then subjected to simple loads.

A current problem for accurate prediction of fatigue damage of structural components is the implementation of physical damage mechanisms based models for a real loading case characterized by a multiaxial stress/strain state. **There is gap between the macrostructural applied load and the mesoscopic model that contains the microstructural characteristics of the material. On the other hand, development of mesoscopic model with microstructural features is also difficult.**

The multiaxial stress/strain state is present both in the case of uniaxial and multiaxial loadings. Prediction of fatigue damage at mesoscale level especially for high cycle fatigue (HCF) and very high cycle fatigue (VHCF) involves multiple effects and complex processes described very well by Castelluccio et al[12].

In view of these considerations, I propose as a first research direction to develop a methodology for fatigue damage prediction at mesoscopic level. This methodology involves numerical analysis on mesoscopic models with microstructural characteristics of the material. Submodeling technique will be used to evaluate the stress and strain state at mesoscopic level. Submodeling techniques are introduced in the stress analysis due to the limitation of the full model to capture the correct stress concentrations at critical locations[13]. The submodeling technique is based on the St. Venant's principle, "if an actual distribution of forces is replaced by an equivalent system, the distribution of stress and strain is altered only near the regions of boundary condition application". Hence, the boundary locations for the submodels are chosen at a safer distance from the area of interest where displacements are

[9] M.D. Sangid, *The physics of fatigue crack initiation*, International Journal of Fatigue, 57: 58-72, 2013.
[10] E. Schmid, W. Boas, *Plasticity of crystals with special reference to metals*, F.A. Hughes &Co. Limited, London, 1950;
[11] A. Cernescu, *The role of microstructure on fatigue crack propagation*, Chapter 7 in "*Recent trends in fatigue design*" book, edited by R. Branco, Nova Publisher New York, 2014.
[12] G.M. Castelluccio, W.D. Musinski, D.L. McDowell, *Computational micromechanics of fatigue of microstructures in the HCF-VHCF regimes*, International Journal of Fatigue, 93: 387-396, 2016;
[13] R. Nayak, *Submodeling techniques in stress analysis*, white paper, HCL Technologies, 2011;

converged. The challenge in applying this technique consists in the development of mesoscale size submodels. This will be completed through successive submodeling, until the mesoscopic level is reached, fig. 3.2.

Another challenge in implementing the methodology is the modelling of the morphology of the mesoscopic model. At this scale, the material is in the form of clusters of grains of different geometry, size and orientation relative to the loading axis. The generation of a polycrystal model include the stages: the generation of the polycrystal morphology, described by sets of points, lines, surfaces and volumes, and respectively the free meshing of the morphology. In this respect, Voronoi tessellation models proved to be very effective in polycrystalline modelling. Voronoi tessellation is a collection of entities that fills the space with no overlaps and no gaps. These entities are polyhedra and are formally defined as zones of influence of a particular set of points, corresponding to their centres. From a physical point of view, the generation of Voronoi tessellations corresponds to a process of solidification or recrystallization where all grains nucleate at the same time and grow isotropically at the same rate[14].

In addition, the mechanical properties of the material grains function of their orientation must be known. This is another challenge because it involves testing of single crystal specimens with different orientations, which is not simple.

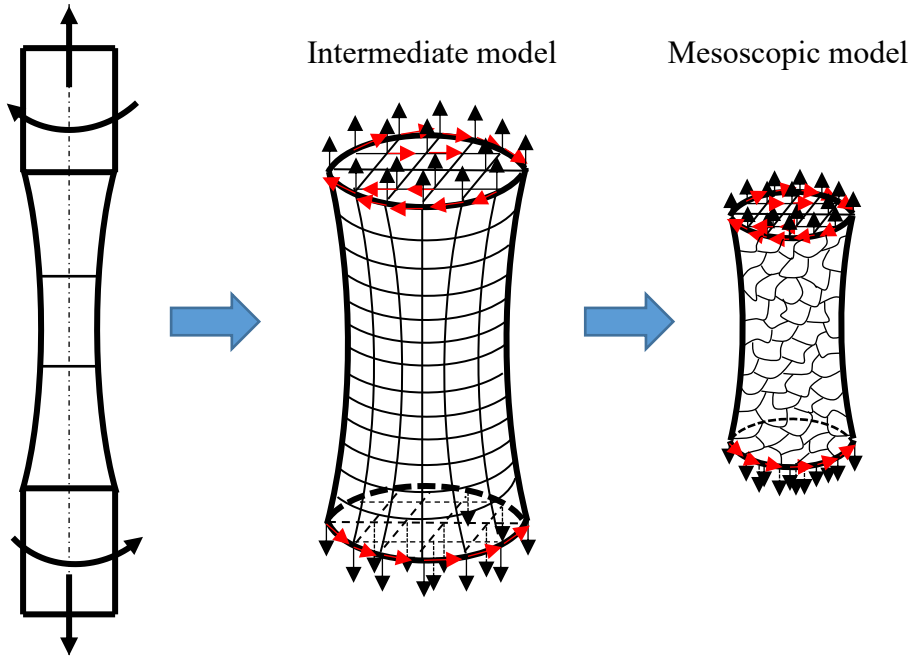

Fig. 3.2. Submodeling technique from macroscopic to mesoscopic scale

[14] R. Quey, P.R. Dawson, F. Barbe, *Large-scale 3D random polycrystals for the finite element method: generation*, meshing and remeshing, Comut. Methods Appl. Mech. Engrg., 200: 1729-1745, 2011;

3.1.2. Couple stress theory in microstructure-dependent analysis

Classical continuum mechanics is an approximation based on the assumption that matter is continuously distributed throughout the body. This theory provides a reasonable basis for analysing the behaviour of materials at the macroscale level, where the microstructure can be neglected. However, the mechanical behaviour in small scales is different from the behaviour at macroscale[15]. Therefore, an accurate analysis of stress and strain state at mesoscale level require a consistent size-dependent continuum mechanics theory, which accounts for the microstructure of materials. Such a theory introduce a couple-stresses and was originally postulated by Voigt[16]. However, Cosserat brothers were the first to develop a mathematical model to analyse materials with couple-stresses[17].

This is a local theory that introduces a characteristic length parameter and consider a material microrotation independent of the continuum mechanical rotation.

In couple stress theory, micropolar continua are characterized by a stress tensor which is not necessarily symmetric. The plane stress tensor is characterized by four stress components and two couple stresses, fig. 3.3. In 3D stress state, the tensor is composed of nine stress components and respectively nine couple stresses.

The local format of linear and angular momentum in the material domain D, when the body forces and body couples are omitted is:

$$div(\boldsymbol{\sigma})^t = 0 \quad ; \quad \boldsymbol{\sigma}_{ij,i} = 0 \tag{3.1}$$

$$div(\boldsymbol{\mu})^t + \boldsymbol{e}:\boldsymbol{\sigma} = 0 \quad ; \quad \boldsymbol{\mu}_{ij,i} + \boldsymbol{e}_{jkl}\boldsymbol{\sigma}_{kl} = 0 \tag{3.2}$$

From the second equilibrium equation, the stress tensor is symmetric if the couple stresses form a self-equilibrating state:

$$\boldsymbol{\sigma} = \boldsymbol{\sigma}^t \leftrightarrow \boldsymbol{e}:\boldsymbol{\sigma} = 0 \text{ if } div(\boldsymbol{\mu})^t = 0 \tag{3.3}$$

The notation $\boldsymbol{e}$ denotes the third order permutation tensor. The traction and couple stress boundary conditions are:

$$\boldsymbol{N}\cdot\boldsymbol{\sigma} = \boldsymbol{t}^{\sigma} \text{ on } \partial D^{\sigma} \text{ and } N_i\sigma_{ij} = t_j^{\sigma} \tag{3.4}$$

$$\boldsymbol{N}\cdot\boldsymbol{\mu}^t = \boldsymbol{t}^{\mu} \text{ on } \partial D^{\mu} \text{ and } N_i\mu_{iz} = t_z^{\mu} \tag{3.5}$$

where $\partial D = \partial D^{\sigma} \cup \partial D^{\mu}$.

The representation of the non-symmetric state of stress in the Mohr plane leads to a circle in two-dimensions (three circles in the three-dimensional case) whose centre is no longer

[15] Ali R. Hadjesfandiari, Gary F. Dargush, *Couple stress theory for solids*, International Journal of Solids and Structures, 48: 2496-2510, 2011;
[16] W. Voigt, Theoretische studien fiber die elastizitatsverhiltnisse der kristalle (Theoretical studies on the elasticity relationships of crystals), Abh. Gesch. Wissenschaften, 34, 1887;
[17] E. Cosserat, F. Cosserat, Theorie des corps deformables, A. Hermann et Fils, Paris, 1909;

located on the σ – axis. Defining the normal stress component $\sigma = \boldsymbol{N} \cdot \boldsymbol{\sigma} \cdot \boldsymbol{N}$, and the shear stress components $\tau = \boldsymbol{N} \cdot \boldsymbol{\sigma} \cdot \boldsymbol{T}$ for an arbitrary surface element with the normal $\boldsymbol{N}$ and the tangent vector $\boldsymbol{T} \perp \boldsymbol{N}$, the extended Cauchy argument in figure 3.4 leads, in two dimensions, to the transformation relations of stress and couple stress:

$$\sigma = \sigma_{xx} cos^2\alpha + \sigma_{yy} sin^2\alpha + \left(\tau_{xy} + \tau_{yx}\right) \sin\alpha \cdot \cos\alpha \tag{3.6}$$

$$\tau = \tau_{xy} cos^2\,\alpha - \tau_{yx} sin^2\,\alpha + \left(\sigma_{yy} - \sigma_{xx}\right) \sin\alpha \cdot \cos\alpha \tag{3.7}$$

$$\mu = \mu_{xz} \cos\alpha + \mu_{yz} \sin\alpha \tag{3.8}$$

Figure 3.5 illustrates the geometric representation in the Mohr stress space of a non-symmetric stress state.

Decomposing the non-symmetric state of stress into symmetric and skew-symmetric components, it is readily seen that the shift of the centre of Mohr's circle along the shear ordinate is a measure of the loss of symmetry.

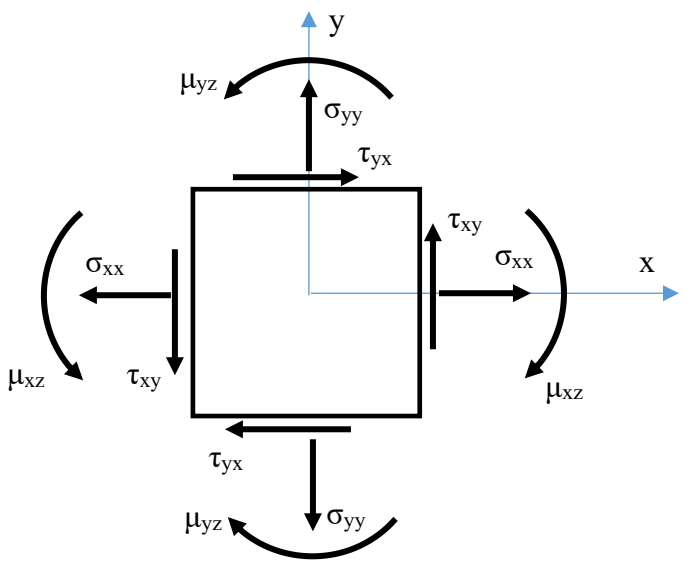

Fig. 3.3. The stress tensor in couple stress theory (μ_{ij} – couple stresses).

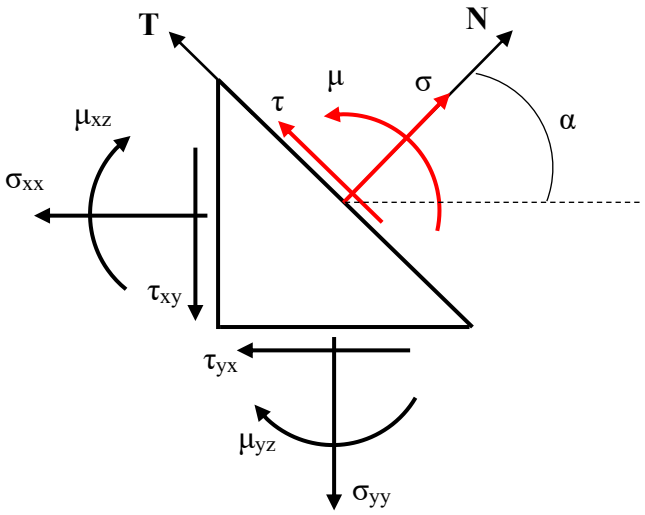

Fig. 3.4. Non-symmetric stress and couple stress state in Cosserat continua

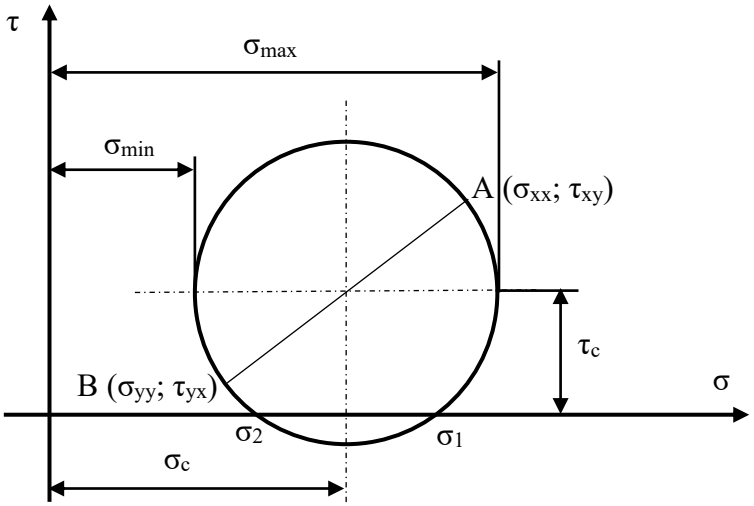

Fig. 3.5. Mohr's circle of a non-symmetric state of stress

A topical issue that I propose to address is the implementation of the couple stress theory in finite element method. This can be done by developing finite elements with additional features as length-scale parameter and additional microrotations.

Another topical issue is the identification of the couple stresses, for which there is no clear approach because their estimation depends on the local nature of the material, which is characterized by a length scale parameter. However, performing tests on large grains specimens (e.g. in the order of millimetres) can highlight the local deformation state of the material that allows the length scale parameter to be evaluated.

3.2. Professional plan

The level of professional training I have gained so far allows me to aspire with great confidence to a position of internationally recognized researcher in the field of mechanical behaviour of materials. The four postdoctoral research programs started in 2010, (2010 – 2013 – Politehnica University Timisoara, Romania, 2013 – 2014 – Aalto University, Finland, 2017 – 2018 – Vrije Universiteit Brussel, Belgium, 2018 – present – Marie Curie Individual Fellowship at Cardiff University, United Kingdom) contributed on the one hand to shape my professional profile. On the other hand, they have given me the opportunity to experience some of the best performing education systems.

On a professional plan, I propose two clear objectives that will be achieved by completing three actions.

The objectives consist of increasing the international recognition as an established researcher, and respectively raising the professional level of the collective in which I work.

To accomplish these goals, a first action is to prepare an application for the ERC Consolidator grant. This program is supported by the European Research Council to strengthen researchers' independence by establishing a research team and continuing to develop a successful career. The program also supports applications where already-created independent research teams want to strengthen them.

A second action on the professional plan is to attract early career researchers to carry out research funded by Marie Sklodowska-Curie Actions. As a beneficiary of such a fellowship, I believe I have the knowledge to prepare a successful application and further coordinate until it is completed. Attracting young researchers is beneficial to the collective in which I work and, on the other hand, to the university by increasing international prestige.

Finally yet importantly, intergroup collaborations that ensure the transfer of knowledge, strengthen relationships, thus creating successful research teams is another occupational concern.

3.3. Academic plan

For a successful career, the academic activity must be conducted in parallel with research. My belief is that science is the key to progress but needs to be transmitted through education. The research carried out so far has led to the accumulation of a significant knowledge that will be transposed into a series of professional courses available to the academic environment.

Thus, the experience of composite materials research helps me in developing a course on the mechanical behaviour of composite materials. Locally, I notice a lack of courses on this subject although the graduate engineers are increasingly confronted with the use of composite materials in designing technical products.

Also, one of the constant concerns in my research activity is the use of numerical methods in the assessment of the stress and strain state in components and structures. Also, the numerical methods represent a tool in engineering work. Currently, there are several numerical methods that can be successfully applied in solving certain engineering problems. There is also a tendency to use free license numeric computing platforms that require defining the analysed problem under a coding language based on the calculation algorithm of the used numerical method. In this context, I consider that a course presenting the basic algorithm of the numerical methods often used in the mechanical engineering can help students and engineers in their work.

Another component of the academic work on which I will focus is the supervising and mentoring activity. In this direction, I have acquired experience in coordinating undergraduate and master projects and I have been co-supervisor for some PhD students. My goal is to attract international students in conducting doctoral studies in my department. Attracting funds for research from national and international grant competitions will make it possible to reach the target and supporting doctoral students' funding.

Appendix 1. Additional relationships for ***Research on cylindrical cell honeycomb core structure***

- Compression in the longitudinal direction (1):

$$a = \frac{\pi \cdot r^3}{4} + R \cdot \left[0.5r \cdot \left(-4 + 3 \cdot \sqrt{1 - \frac{r^2}{R^2}}\right) R + 2 \cdot \left(-1 + \sqrt{1 - \frac{r^2}{R^2}}\right) \cdot R^2 + \left(r^2 + 2rR + \right.\right.$$

$$\left.\left. + \frac{3R^2}{2}\right) \cdot asin\left(\frac{r}{R}\right)\right] \quad \text{(A1.1)}$$

$$b = r^2 + \left(-1 + \sqrt{1 - \frac{r^2}{R^2}}\right) \cdot R^2 + R(r + R) \cdot asin\left(\frac{r}{R}\right) \quad \text{(A1.2)}$$

$$c = -0.392699r^3 + 0.25R \cdot (-3.14159r^2 + 0.8584rR + R^2) \quad \text{(A1.3)}$$

$$d = -0.5r^2 + rR \cdot \left[0.5 - 0.5 \cdot asin\left(\frac{r}{R}\right)\right] \quad \text{(A1.4)}$$

$$e = \frac{\pi r}{2} + R \cdot asin\left(\frac{r}{R}\right) \quad \text{(A1.5)}$$

$$g = -\frac{-b \cdot d + c \cdot e}{-b^2 + a \cdot e} \; ; \; h = -\frac{b \cdot c - a \cdot d}{b^2 - a \cdot e} \quad \text{(A1.6)}$$

$$i = -0.333hr^2 + 0.261799r^3 - \frac{g\pi r^3}{12} -$$

$$-0.333hrR \cdot \left[-1 + asin\left(\frac{r}{R}\right)\right] + \frac{grR \cdot \left[r + 4R - 2R \cdot \sqrt{1 - \frac{r^2}{R^2}} - 2(r + R) \cdot asin\left(\frac{r}{R}\right)\right]}{6} +$$

$$+0.1666R \cdot \left[-2r^2 + (r^2 + 0.5R^2) \cdot asin\left(\frac{r}{R}\right) + 0.25R^2 \cdot sin\left(3.1415 - 2 \cdot asin\left(\frac{r}{R}\right)\right)\right] \quad \text{(A1.7)}$$

$$j = -\frac{hr^2 \cdot (-2 + \pi)}{6} + 0.333r^3 - \frac{gr^3}{6} -$$

$$-0.333hR \cdot \left[\left(-1 + \sqrt{1 - \frac{r^2}{R^2}}\right) \cdot R + (2r + R) \cdot asin\left(\frac{r}{R}\right)\right] +$$

$$+0.0833rR \cdot \left[-3r - 4R + 2R \cdot \sqrt{1 - \frac{r^2}{R^2}} + 2 \cdot (2r + R) \cdot asin\left(\frac{r}{R}\right)\right] -$$

$$-\frac{gR}{6} \cdot \left[rR \cdot \left(-6 + 5 \cdot \sqrt{1 - \frac{r^2}{R^2}}\right) + 4R^2 \cdot \left(-1 + \sqrt{1 - \frac{r^2}{R^2}}\right) + (4r^2 + 6rR + 3R^2) \cdot asin\left(\frac{r}{R}\right)\right] \quad \text{(A1.8)}$$

- Compression in the in-plane transverse direction (2) of the cell:

$$a = \frac{r}{4} \cdot [(-8 + 3\pi) \cdot r^2 - 4rR \cdot (-2 + \pi) + 2\pi R^2] +$$

$$+ \frac{1}{2} \cdot \left[R^2 \cdot \sqrt{1 - \frac{r^2}{R^2}} \cdot (r - 4R) + 3R^3 \cdot asin\left(\frac{r}{R}\right) \right] \quad \text{(A1.9)}$$

$$b = \frac{r}{2} \cdot [r \cdot (-2 - \pi) - \pi R] - \frac{\pi R^2}{2} + R^2 \cdot \sqrt{1 - \frac{r^2}{R^2}} + R^2 \cdot asin\left(\frac{r}{R}\right) \quad \text{(A1.10)}$$

$$c = R \cdot (0.25r^2 - 0.5rR + 0.25R^2) - 0.0353982r^3 + 0.785398rR^2 \quad \text{(A1.11)}$$

$$d = r \cdot (-0.285398r - 0.785398R) + 0.5R \cdot (r - R) \quad \text{(A1.12)}$$

$$e = \frac{\pi r}{2} + R \cdot \left(\frac{\pi}{2} - asin\left(\frac{r}{R}\right)\right) \quad \text{(A1.13)}$$

$$g = -\frac{-b \cdot d + c \cdot e}{-b^2 + a \cdot e} \; ; \; h = -\frac{b \cdot c - a \cdot d}{b^2 - a \cdot e} \quad \text{(A1.14)}$$

$$i = 13hR \cdot (r - R) - 6.5gR \cdot (r - R)^2 + 1.625r \cdot (1.42478r^2 + 4.5663rR +$$

$$6.2831R^2) + 6.5gr \cdot [-(-3 + \pi) \cdot r^2 + \pi R^2] + 1.625R^2 \cdot \left[-2r \cdot \sqrt{1 - \frac{r^2}{R^2}} + \pi R - 2R \cdot \right.$$

$$\left. asin\left(\frac{r}{R}\right) \right] \quad \text{(A1.15)}$$

- Shear in the longitudinal direction (1) of the cell:

$$a = -\frac{3r^3}{2} - r^2 R + \frac{R^2}{2} \cdot \left[r \cdot \sqrt{1 - \frac{r^2}{R^2}} + R \cdot asin\left(\frac{r}{R}\right) \right] \quad \text{(A1.16)}$$

$$b = \frac{(3\pi - 8) \cdot r^3}{4} + \frac{R^2}{2} \cdot \left[r \cdot \sqrt{1 - \frac{r^2}{R^2}} + R \cdot asin\left(\frac{r}{R}\right) \right] \quad \text{(A1.17)}$$

$$i = \frac{ar^3}{2b} + \frac{\pi r^3}{2} - \frac{aR}{2b} \cdot \left[-2r^2 + rR \cdot \sqrt{1 - \frac{r^2}{R^2}} + R^2 \cdot asin\left(\frac{r}{R}\right) \right] + \frac{R}{2} \cdot \left[-4r^2 + rR\sqrt{1 - \frac{r^2}{R^2}} + \right.$$

$$\left. (2r^2 + R^2) \cdot asin\left(\frac{r}{R}\right) \right] \quad \text{(A1.18)}$$

$$j = 1.6r^3 + \frac{0.8aR^3}{b} \cdot \left(-2 + \frac{3\pi}{4}\right) + \frac{0.8arR}{2b} \cdot (3r + 2R) + \frac{0.8rR}{2} \left[-3r - 4R + 2R \cdot \sqrt{1 - \frac{r^2}{R^2}} + \right.$$

$$\left. 2(2r + R) \cdot asin\left(\frac{r}{R}\right) \right] \quad \text{(A1.19)}$$

- Shear in the in-plane transverse direction (2) of the cell:

$$i = 0.07142r \cdot [r^2 \cdot (-8 + 3\pi) + 4rR \cdot (-2 + \pi) + 2\pi R^2] + 0.14285R^2 \cdot \left[-r \cdot \sqrt{1 - \frac{r^2}{R^2}} + R \cdot asin\left(\frac{r}{R}\right)\right] \quad \text{(A1.20)}$$

Appendix 2. *The crack closure effect by Newman model*

Based on the crack closure concept, the different curves of da/dN versus ΔK_{app} measured at different R ratios can be replaced by a single curve of da/dN versus ΔK_{eff}, fig. A2.1.

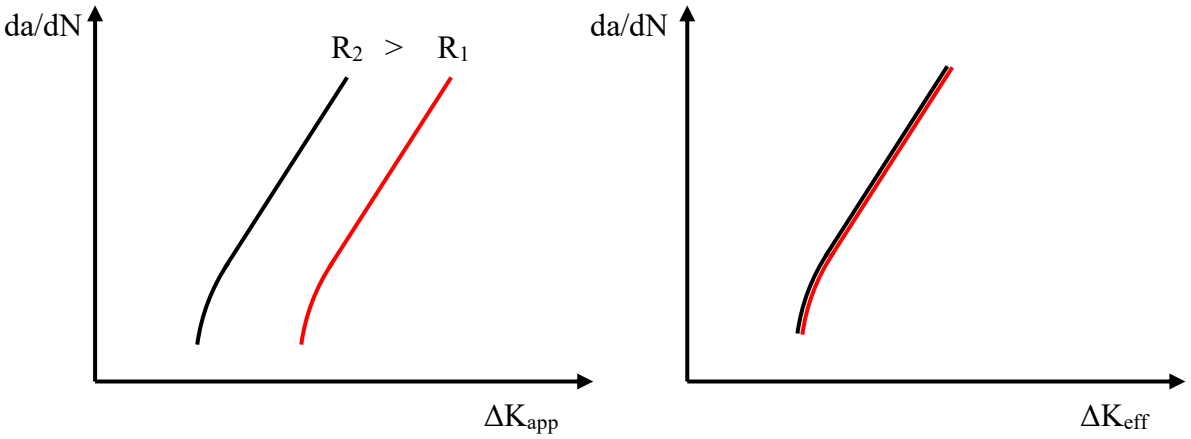

Fig. A2.1. The crack closure concept

Applying the same concept for the case of a welded material where is not taken into account the effect of microstructure and residual stresses, the curves of da/dN versus ΔK_{eff} corresponding to base material and respectively weld metal, measured at the same stress ratio converges into a single curve of da/dN versus ΔK_{eff}, fig. A2.2.

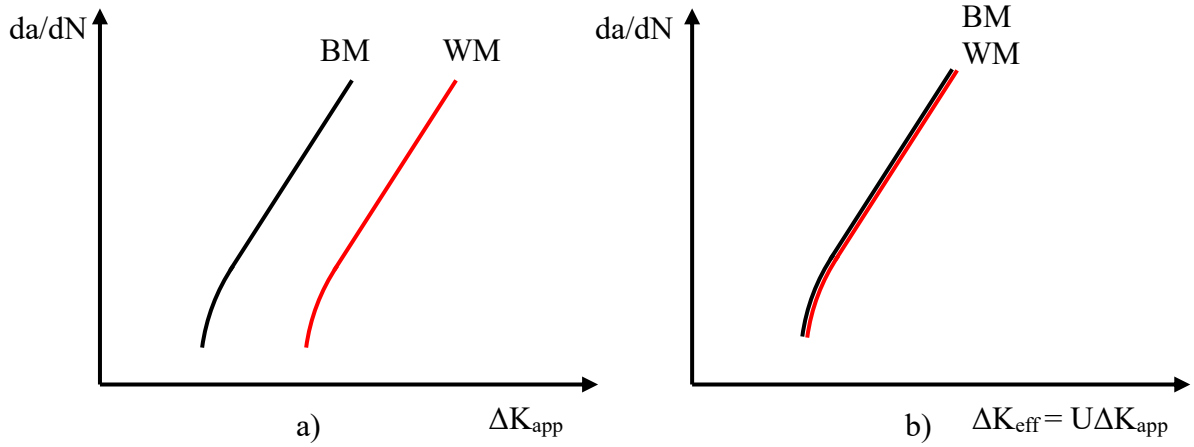

Fig. A2.2. The crack closure concept for welded material at the same stress ratio

In the presence of residual stresses the convergence from Fig. A2.2.b can be modified according to their distribution ahead of the crack tip. Following Newman crack closure model, it is considered that ΔK_{eff} can be calculated as:

$$\Delta K_{eff} = U\Delta K_{app} \quad \text{(A2.1)}$$

$$U = \frac{1-f}{1-R} \quad \text{(A2.2)}$$

$$f = \frac{S_0}{S_{max}} = A_0 + A_1 R + A_2 R^2 + A_3 R^3 \quad \text{for R} \geq 0 \quad \text{(A2.3)}$$

$$A_0 = (0.825 - 0.34\alpha + 0.05\alpha^2)[cos(\pi S_{max}/2\sigma_0)]^{1/\alpha} \quad \text{(A2.4)}$$

$$A_1 = (0.415 - 0.071\alpha)\frac{S_{max}}{\sigma_0} \quad \text{(A2.5)}$$

$$A_2 = 1 - A_0 - A_1 - A_3 \quad \text{(A2.6)}$$

$$A_3 = 2A_0 + A_1 - 1 \quad \text{(A2.7)}$$

For plane stress conditions $\alpha = 1$, while for plane strain conditions $\alpha = 3$. The flow stress σ_0 is taken to be the average between the uniaxial yield stress and uniaxial tensile strength of the material.

In this study the constants $A_0 - A_3$ were determined by calibration of equations (A2.1), (A2.2) and (A2.3) such that the curve of da/dN versus ΔK_{eff} determined by closure model for the base material to match with the curve da/dN versus ΔK_{eff} determined experimentally for base material and stress ratio $R = 0.1$, fig. A2.3. The fitting parameters used were $\alpha = 2$ and $S_{max}/\sigma_0 = 0.3$. Thus the constants were found as $A_0 = 0.32565$, $A_1 = 0.0819$, $A_2 = 0.8592$ and $A_3 = -0.26679$.

In this regard, the constants $A_0 - A_3$ are not affected by the residual stresses and can be used for fatigue crack growth data in the weld metal.

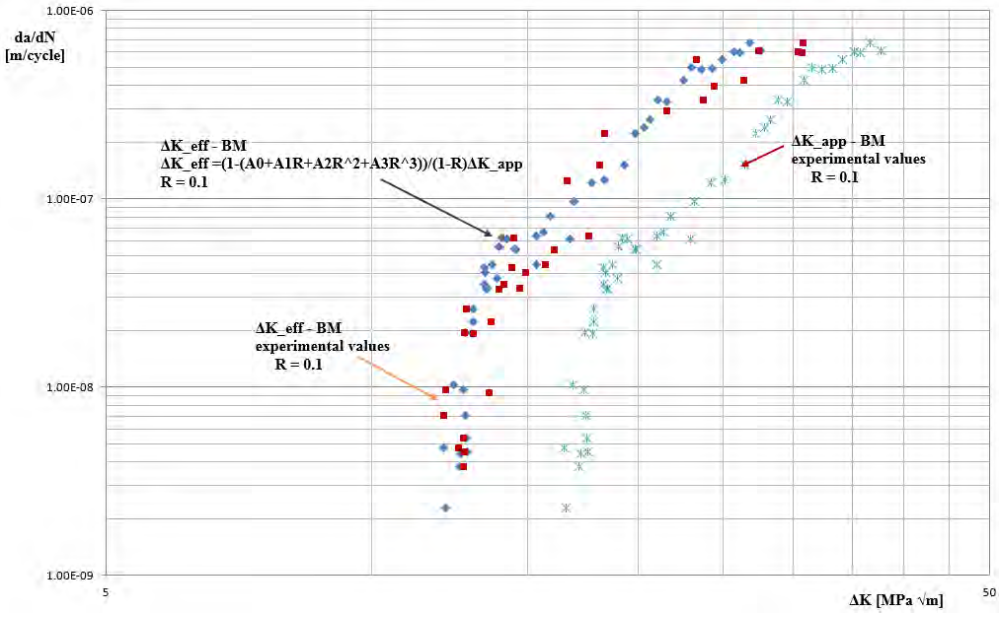

Fig. A2.3. Calibration of Newman closure function

Appendix 3. *Relevant publications*

1. Anghel Cernescu, Ion Dumitru, Lorand Kun, *Multiaxial fatigue damage prediction in a proportional loading cycle*, The Romanian Journal of Technical Sciences – Applied Mechanics, vol. 65(1), pp. 68-83, 2020;

2. Anghel Cernescu, N. Faur, C.M. Bortun, M. Hluscu, *A methodology for fracture strength evaluation of complete denture*, Engineering Failure Analysis, 18(5): 1253-1261, 2011;

3. Anghel Cernescu, N. Faur, C.M. Bortun, C. Nes, *Fatigue crack growth rate in acrylic resins under variable amplitude loading*, Theoretical and Applied Fracture Mechanics, 56(1): 58-61, 2011;

4. Anghel Cernescu, J. Romanoff, *Bending deflection of sandwich beams considering local effect of concentrated force*, Composite Structures, 134: 169-175, 2015;

5. Anghel Cernescu, J. Romanoff, H. Remes, N. Faur, J. Jelovica, *Equivalent mechanical properties for cylindrical cell honeycomb core structure*, Composite Structures, 108(1): 866-875, 2014;

6. Anghel Cernescu, I. Dumitru, N. Faur, N. Branzei, R. Bogdan, *The analysis of a damaged component from the connection system of the wagons*, Engineering Failure Analysis, 29: 93-107, 2013;

7. Anghel Cernescu, H. Remes, P. Lehto, J. Romanoff, *Fatigue crack growth rate in laser-welded web core sandwich panels – fatigue crack propagation in welded base metal*, 11th International Fatigue Congress, PTS 1 and 2, Advanced Materials Research, 891-892: 1212-1216, 2014;

8. Anghel Cernescu, *The influence of crack tip shielding on fatigue crack propagation*, Frattura Ed Integrita Strutturale, 41: 307-313, 2017;

9. Anghel Cernescu, *The role of microstructure on fatigue crack propagation*, Book chapter in *Recent Trends in Fatigue Design*, Nova Science Publishers, 2015;

10. Anghel Cernescu, Ion Dumitru, *Oboseala conductoarelor liniilor electrice aeriene (Fatigue of overhead power line conductors)*, Romanian Academy Publisher, ISBN 978-973-27-2783-6, 293 pages, 2017;

References

[1] A.F. Bettencourt, C.B. Neves, M.S. de Almeida, L.M. Pinheiro, S.A. e Oliveira, L.P. Lopes, M.F. Castro, *Biodegradation of acrylic based resins: A review*, Dental Materials, 26: e171-e180, 2010;

[2] X-K. Zhu, J.A. Joyce, *Review of fracture toughness (G, K, J, CTOD, CTOA) testing and standardization*, Engineering Fracture Mechanics, 85: 1-46, 2012;

[3] ASTM D5045, *Standard test methods for plane-strain fracture toughness and strain energy release rate of plastic materials*, ASTM International, USA;

[4] R.G. Hill, J.F. Bates, T.T. Lewis, N. Rees, *Fracture toughness of acrylic denture base*, Biomaterials, Butterworth & Co Publishers, vol. 4, 1983;

[5] C. Dumitru, Anghel Cernescu, I. Eremici, C.M. Bortun, D. Achiriloaiei, *Fatigue behavior of two acrylic denture base resins*, Materiale Plastice, 55(4): 567-570, 2018;

[6] O. Gurbuz, F. Unalan, I. Dikbas, *Comparative study of the fatigue strength of five acrylic resins*, Journal of the Mechanical Behavior of Biomedical Materials, 3: 636-639, 2010;

[7] F. Takeshige, Y. Kawakami, M. Hayashi, S. Ebisu, *Fatigue behavior of resin composites in aqueous environments*, Dental Materials, 23: 893-899, 2007;

[8] ASTM D7791-17, *Standard test method for uniaxial fatigue properties of plastics*, ASTM International, USA;

[9] Anghel Cernescu, N. Faur, C. Bortun, C. Nes, *Fatigue crack growth rate in acrylic resins under variable amplitude loading*, Theoretical and Applied Fracture Mechanics, 56: 58-61, 2011;

[10] F. Ding, M. Feng, Y. Jiang, *Modelling of fatigue crack growth from a notch*, Int. J. Plasticity, 23: 1167-1188, 2007;

[11] H. Zhang, A. Fatemi, *Short fatigue crack growth from a blunt notch in plate specimens*, Int. J. of Fract., 170(1): 1-11, 2011;

[12] K. Tanaka, Y. Nakai, *Propagation and non-propagation of short fatigue cracks at a sharp notch*, Fatigue Eng. Mater. Struct., 6: 315-327, 1983;

[13] AS Hargreaves, *The prevalence of fractured dentures. A survey*, Br. Dent. J., 126: 451-5, 1969;

[14] E. Horton, *Experimental investigation of internal strains in polymerised methyl methacrylate as revealed by polarized light*, Br. Dent. Jr., 86: 176-180, 1949;

[15] E. Matthews, E.A. Wain, *Stresses in denture bases*, Br. Dent. J., 100: 167-171, 1956;

[16] A. Cernescu, N. Faur, C. Bortun, M. Hluscu, *A methodology for fracture strength evaluation of complete denture*, Engineering Failure Analysis, 18: 1253-1261, 2011;
[17] A. Cernescu, C. Bortun, N. Faur, *Reverse Engineering and FEM analysis for mechanical strength evaluation of complete dentures: a case study*, book chapter in Reverse Engineering – Recent Advances and Applications, IntechOpen, DOI: 10.5772/32486, 2012;
[18] E. Giner, N. Sukumar, J.E. Tarancon, F.J. Fuenmayor, *An Abaqus implementation of the extended finite element method*, Eng. Frac. Mech., 76: 347-368, 2009;
[19] N.A. Apetre, *Sandwich panels with functionally graded core*, Dissertation presented to the Graduate School of the University of Florida, USA, 2005;
[20] H.G. Allen, *Analysis and design of structural sandwich panels*, Osford: Pergamon Press; 1969;
[21] Anghel Cernescu, Jani Rpmanoff, *Bending deflection of sandwich beams considering local effect of concentrated force*, Composite Structures, 134: 169-175, 2015;
[22] S. Timoshenko, J.N. Goodier, *Theory of Elasticity*, McGraw-Hill Book Company, p.85, 1951;
[23] J.N. Reddy, J. Kim, *A nonlinear couple stress-based third-order theory of functionally graded plates*, Composite Structures, 94: 1128-1143, 2012;
[24] J.N. Reddy, *Mechanics of Laminated Composite Plates and Shells – Theory and Analysis*, CRC Press, Second Edition, 2004;
[25] SigmaScan Pro v5, *Image Analysis Software*, Systat Software Inc.;
[26] V. Shulmeister, *Modeling of the mechanical properties of low-density foams*, ISBN 90-423-0025-6, 1997;
[27] W. Witkiewicz, A. Zielinski, *Properties of the polyurethane (PU) light foams*, Advances in Materials Science, vol. 6, no. 2(10): 35-51, 2006;
[28] S. Mazumdar, D. Karthikeyan, D. Pichler, M. Benevento, R. Frassine, *State of the composites industry report for 2017*, Composites Manufacturing, 2017;
http://compositesmanufacturingmagazine.com/2017/01/composites-industry-report-2017/8/
[29] S. Houston, *Advantages and disadvantages of composite materials on airplanes*, 2017, https://www.thebalance.com/composite-materials-aircraft-structure-282777;
[30] *Wind turbine blades: Big and getting bigger*, CompositesWorld, https://www.compositesworld.com/articles/wind-turbine-blades-big-and-getting-bigger;
[31] R. Younes, A. Hallal, F. Fardoun, F. H. Chehade, *Comparative review study on elastic properties modeling for unidirectional composite materials*, Chapter 17 in *Composites and their properties*, InTech Open Science Publisher, 2012;

[32] W. Voigt, *Uber die Beziehung zwischen den beiden Elastizitatskonstanten Isotroper Korper*, Wied. Ann, 38: 573-587, 1889;

[33] A. Reuss, *Berechnung der Fliessgrense von Mischkristallen auf grund der Plastizitatsbedingung fur Einkristalle*, Zeitschrift Angewandte Mathematik und Mechanik, 9: 49-58, 1929;

[34] J.C. Halpin, J.L. Kardos, *The Halpin-Tsai equations: a review*, Polymer Engineering and Science, 16(5): 344-352, 1976;

[35] C.C. Chamis, *Mechanics of composite materials: past, present and future*, NASA Technical Memorandum 100793, 21st Annual Meeting of the Society for Engineering Science, Virginia, October 15-17, 1984;

[36] B. Paul, *Prediction of elastic constants of multiphase materials*, Transactions of the Metallurgical Society of AIME, pp. 36-41, 1960;

[37] W. Rosen, N.F. Dow, Z. Hashin, *Mechanical properties of fibrous composites*, NASA, Contract no. NASw 470, 1964;

[38] R.M. Jones, *Mechanics of composite materials*, Second edition, Taylor & Francis Publisher, 1999;

[39] A. Kelly, G.J. Davies, *The principles of the fibre reinforcement of metals*, Metallurgical Reviews, vol. 10(37): 1-77, 1965;

[40] G.N. Karam, *Effect of fiber volume on tensile properties of real unidirectional fibre-reinforced composites*, Composites, 22(2): 84-88, 1991;

[41] C. Lee, W. Hwang, *Modified rule of mixtures for prediction of tensile strength of unidirectional fiber-reinforced composites*, Journal of Materials Science Letters, 17: 1601-1603, 1998;

[42] Z. Hashin, D. Bagchi, B.W. Rosen, *Non-linear behavior of fiber composite laminates*, Materials Sciences Corporation, NASA, 1974;

[43] R.M. Jones, H.S. Morgan, *Analysis of non-linear stress-strain behavior of fiber-reinforced composite materials*, AIAA Journal, 15(12):1669-1676, 1977;

[44] M.N. Nahas, *Analysis of non-linear stress-strain response of laminated fibre-reinforced composites*, Fibre Science and Technology, 20: 297-313, 1984;

[45] A. Sabik, *Direct shear stress vs strain relation for fiber reinforced composites*, Composite Part B, 139: 24-30, 2018;

[46] P. Ladeveze, E. Le Dantec, *Damage modelling of the elementary ply for laminated composites*, Composites Science and Technology, 43: 257-267, 1992;

[47] R.T. Gerrit, S. Kokubo, T. Yokozeki, *Identification of damage parameters for intralaminar damage modeling in laminated composites considering transverse stress effects*, Open Journal of Composite Materials, 7: 185-196, 2017;

[48] F. Malgioglio, D. Carella-Payan, B. Magneville, L. Farkas, *Material parameter identification challenge and procedure for intra-laminar damage prediction in unidirectional CFRP*, 6th ECCOMAS Thematic Conference on the Mechanical Response of Composites, Composites, 2017;

[49] Anghel Cernescu, J. Romanoff, H. Remes, N. Faur, J. Jelovica, *Equivalent mechanical properties for cylindrical cell honeycomb core structure*, Composite Structures, vol. 108, pp. 866-875, 2014;

[50] Zhang J, Ashby MF. *The out-of-plane properties of honeycombs*. Int J Mech Sci, 34:475–89, 1992.

[51] Zhang J, Ashby MF. *Buckling of honeycombs under in-plane biaxial stress*. Int J Mech Sci, 34:491–509, 1992.

[52] Xue ZY, Hutchinson JW. *Constitutive model for quasi-static deformation of metallic sandwich cores*. Int J Numer Methods Eng, 61(13): 2205–38, 2004;.

[53] Chung J, Waas AM. *Compressive response and failure of circular cell polycarbonate honeycombs under in-plane uniaxial stresses*. J Eng Mater Tech, 121(4): 494, 1999;.

[54] Chung J, Waas AM. *The in-plane elastic properties of circular and elliptical cell honeycombs*. Acta Mech, 144(1–2): 29–42, 2000;.

[55] Chung J, Waas AM. *Compressive response of circular cell polycarbonate honeycombs under in-plane biaxial static and dynamic loading. Part I: Experiments*. Int J Impact Eng, 27: 729–54, 2002.

[56] Chung J, Waas AM. *Compressive response of circular cell polycarbonate honeycombs under in-plane biaxial static and dynamic loading. Part II: Simulations*. Int J Impact Eng, 27(10): 1015–47, 2002;.

[57] Chung J, Waas AM. *Elastic imperfection sensitivity of hexagonally packed circular cell honeycombs*. Proc Roy Soc Lond – A: Mater, 458(2028): 2851–68, 2002;

[58] Lin TC, Chen TJ, Huang JS. *In-plane elastic constants and strengths of circular cell honeycombs*. Compos Sci Technol, 72: 1380–6, 2012;

[59] Lin TC, Chen TJ, Huang JS. *In-plane mechanical properties of elliptical cell honeycombs*. Compos Struct, 104: 14–20, 2013;

[60] Pingle SM, Fleck NA, Deshpande VS, Wadley HNG. *Collapse mechanism maps for the hollow pyramidal core of a sandwich panel under transverse shear*. Int J Solids Struct, 48: 3417–30, 2011;

[61] Lee S, Barthelat F, Hutchinson JW, Espinosa HD. *Dynamic failure of metallic pyramidal truss core materials – experiments and modeling*. Int J Plast, 22: 2118–45, 2006;

[62] Wicks N, Hutchinson JW. *Optimal truss plates*. Int J Solids Struct, 38(30–31): 5165–83, 2001;

[63] Wicks N, Hutchinson JW. *Performance of sandwich plates with truss cores*. Mech Mater, 36(8): 739–51, 2004;

[64] Deshpande VS, Fleck NA. *High strain rate compressive behavior of aluminium alloy foams*. Int J Impact Eng, 24: 277–98, 2000;

[65] Deshpande VS, Fleck NA. *Collapse of truss core sandwich beams in 3-point bending*. Int J Solids Struct, 38(36–37): 6275–305, 2001;

[66] Sypeck DJ, Wadley HNG. *Cellular metal truss core sandwich structures*. Adv Eng Mater, 4(10): 759–64, 2002;

[67] Wadley HNG, Fleck NA, Evans AG. *Fabrication and structural performance of periodic cellular metal sandwich structures*. Compos Sci Technol, 63: 2331–43, 2003;

[68] Rabczuk T, Kim JY, Samaniego E, Belytschko T. *Homogenization of sandwich structures*. Int J Numer Methods Eng, 61(7): 1009–27, 2004;

[69] Rathbun HJ, Wei Z, He MY, Zok FW, Evans AG, Sypeck DJ, et al. *Measurement and simulation of the performance of a lightweight metallic sandwich structure with a tetrahedral truss core*. J Appl Mech – Trans ASME, 71(3): 368–74, 2004;

[70] Zok FW, Waltner SA, Wei Z, Rathbun HJ, McMeeking RM, Evans AG. *A protocol for characterizing the structural performance of metallic sandwich panels: application to pyramidal truss cores*. Int J Solids Struct, 41(22–23): 6249–71, 2004;

[71] Libove C, Hubka RE. *Elastic constants for corrugated-core sandwich plates*. NACA Technical Note (TN) 2289; 1951.

[72] Montague P, Norris C. *Spot-welded corrugated core sandwich steel panels subject to lateral load*. In: Proceedings of the international conference on steel and aluminium structures, vol. I (steel structures), p. 564–74, 1987;

[73] Tan KH, Montague P, Norris C. *Steel sandwich panels: finite element closed solution and experimental comparison on a 6 m x 2.1 m panel*. Struct Eng, 16(9): 167–76, 1989;

[74] Fung TC, Tan KH, Lok TS. *Analysis of C-core sandwich plate decking*. In: Proceedings of the third international offshore and polar engineering conference, p. 244–9, 1993;

[75] Fung TC, Tan KH, Lok TS. *Elastic constants for Z-core sandwich panels*. J Struct Eng, 120(10): 3046–55, 1994;

[76] Romanoff J, Varsta P. *Bending response of web-core sandwich beams*. Compos Struct 73: 478–87, 2006;

[77] Romanoff J, Varsta P, Klanac *A. Stress analysis of homogenized web-core sandwich beams*. Compos Struct, 79: 411-422, 2007;

[78] Romanoff J, Varsta P. *Bending response of web-core sandwich plates*. Compos Struct 81: 292–302, 2007;

[79] Qiu K. *Analysis and optimal design of lightweight sandwich structures and materials*. PhD thesis, Ecole Doctorale Sciences pour l'Ingenieur et Microtechniques, Universite de Technologie de Belfort-Montbeliard; 2008.

[80] D. Frank, H. Remes, J. Romanoff, *Fatigue assessment of laser stake-welded T-joints*, International Journal of Fatigue, 33-2: 102-114, 2011;

[81] D. Frank, H. Remes, J. Romanoff, *J-integral-based approach to fatigue assessment of laser-stake-welded T-joints*, International Journal of Fatigue, 47: 340-350, 2013;

[82] D. Frank, J. Romanoff, H. Remes, *Fatigue strength assessment of laser stake-welded web-core steel sandwich panels*, Fatigue & Fracture of Engineering Materials & Structures, vol. 36, issue 8, p. 724-737, 2013;

[83] Jiang, X.X., Li, J.M., Cao, R., Zhu, L., Chen, J.H., Wu, Y.X. and Li, Z.G., *Microstructures and properties of sandwich plane laser-welded joint of hull steel*, Materials Science and Engineering A, Vol. 595, 2014, pp. 43-53.

[84] P. Kujala, T. Kukkanen, K. Kotisalo, *Fatigue of all metal sandwich panels – Application for cruise ship longitudinal bulkhead and decks*, M-237, ISBN 951-22-4404-7, Helsinki University of Technology, 1999;

[85] J. Kozak, *Fatigue life of steel laser-welded panels*, Polish Maritime Research, Special Issue, 2006/S1;

[86] T.S. Balasubramanian, V. Balasubramanian, M.A. Muthku Manickam, *Fatigue crack growth behavior of gas tungsten arc, electron beam and laser beam welded Ti-6Al-4V alloy*, Materials and Design, 32: 4509-4520, 2011;

[87] L.W. Tsay, C.S. Chung, C. Chen, *Fatigue crack propagation of D6AC laser welds*, International Journal of Fatigue, 19(1): 25-31, 1997;

[88] L.W. Tsay, C.Y. Tsay, *The effect of microstructures on the fatigue crack growth in Ti-6Al-4V laser welds*, International Journal of Fatigue, 19(10): 713-729, 1997;

[89] R.L. Champoux, J.H. Underwood, J.A. Kapp, *Analytical and experimental methods for residual stress effects in fatigue*, American Society for Testing and Materials, 1988;
[90] J.F. Throop, H.S. Reemsnyder, *Residual stress effects in fatigue*, American Society for Testing and Materials – STP 776, 1982;
[91] D.A. Lados, D. Apelian, *The effect of residual stress on the fatigue crack growth behavior of Al-Si-Mg cast alloys – Mechanisms and corrective mathematical models*, Metallurgical and Materials Transactions A, vol. 37A, 2006;
[92] C.D. Donne, G. Biallas, T. Ghidini and G. Raimbeaux, *Effect of Weld Imperfections and residual stresses on the fatigue crack propagation in friction stir welded joints*, Second International Conference on Friction Stir Welding, 26/28 June 2000, Gothenburg, Sweden;
[93] G. Biallas, *Effect of welding residual stresses on fatigue crack growth thresholds*, International Journal of Fatigue, 50: 10-17, 2013;
[94] C.D. Donne, E. Lima, J. Wegener, T. Buslaps, *Investigations on residual stresses in friction stir welds*, 3rd International Symposium on Friction Stir Welding, Kobe, Japan, 27-28 September 2001;
[95] G. Pouget, A.P. Reynolds, *Residual stress and microstructure effects on fatigue crack growth in AA2050 friction stir welds*, International Journal of Fatigue, 30: 463-472, 2008;
[96] STAS 4203-74, *Metalography. Sampling and preparation of metallographic samples*;
[97] SR EN ISO 6892-1, *Metallic materials – Tensile testing – Part 1: Method of test at room temperature*, 2010;
[98] ASTM E647, *Standard test method for measurement of fatigue crack growth rates*;
[99] H.J. Schindler, W. Cheng and I. Finnie, *Experimental determination of stress intensity factors due to residual stresses*, Experimental Mechanics, vol. 37, no. 3, 1997;
[100] M.B. Prime, *Residual stress measurement by successive extension of a slot: the crack compliance method*, Applied Mechanics, vol. 52, no. 2: 75-96; 1999;
[101] W. Cheng, I. Finnie, *Measurement of residual hoop stresses in cylinders using the compliance method*, ASME J. Eng. Mat. Tech., 108: 87-92, 1986;
[102] H.J. Schindler, *Experimental determination of crack closure by the cut compliance technique*, Advances in fatigue crack closure measurement and analysis, ASTM STP 1343, R.C. McClung and J.C. Newman, Jr., American Society for Testing and Materials, 1998;
[103] K. Makhlouf and J.W. Jones, *Near-threshold fatigue crack growth behavior of a ferritic stainless steel at elevated temperatures*, International Journal of Fatigue, vol. 14(2): 97-104, 1992;

[104] C.S. Kusko, J.N. Dupont and A.R. Marder, *Influence of stress ratio on fatigue crack propagation behavior of stainless steel welds*, Welding Journal, 2004;

[105] Y.E. Ma, P. Staron, T. Fischer, P.E. Irving, *Size effects on residual stress and fatigue crack growth in friction stir welded 2195-T8 aluminium – Part II: Modelling*, International Journal of Fatigue, 33: 1426-1434, 2011;

[106] J.C. Newman, *A crack opening stress equation for fatigue crack growth*, International Journal of Fracture, 24: R131-R135, 1984;

[107] M. Beghini, L. Bertini and E. Vitale, *Influence of different residual stress distributions on fatigue crack growth*, ECF 8 Fracture Behavior and Design of Materials and Structures, Italy, 1990;

[108] Y. Motoyashiki, A. Bruckner-Foit, A. Sugeta, *Microstructural influence on small fatigue cracks in a ferrite-martensite steel*, Engineering Fracture Mechanics, 75: 768-778, 2008;

[109] A.A. Korda, Y. Miyashita, Y. Mutoh, T. Sadasue, *Fatigue crack growth behavior in ferritic-pearlitic stels with networked and distributed pearlite structures*, International Journal of Fatigue, 29: 1140-1148, 2007.

[110] M.N., James, *Some unresolved issues with fatigue crack closure – measurement, mechanism and interpretation problems*, http://www.gruppofrattura.it/ocs/index.php/ICF/ICF9/paper/viewFile/4331/1491;

[111] R.H., Christensen, *Fatigue crack growth affected by metal fragments wedged between opening-closing crack surfaces*, Appl. Mater. Res., 2(1963) 207-210;

[112] W., Elber, *Fatigue crack closure under cyclic tension*, Engng. Fract. Mech., 2(1970) 37-45;

[113] W., Elber, *The significance of fatigue crack closure*, Damage Tolerance in Aircraft Structures ASTM STP 486 (1971) 230-242;

[114] R.O. Ritchie, *Mechanisms of fatigue crack propagation in metals, ceramics and composites: role of crack tip shielding*, Materials Science and Engineering, A103: 15-28, 1988;

[115] R. Pippan, A. Hohenwarter, Fatigue crack closure: a review of the physical phenomena, FFEMS, 00: 1-25, 2017, doi: 10.1111/ffe.12578;

[116] Y. Mutoh, A.A. Korda, Y. Miyashita, T. Sadasue, *Stress shielding and fatigue crack growth resistance in ferritic-pearlitic steel*, Materials Science and Engineering A, 468-470: 114-119, 2007, doi: 10.1016/j.msea.2006.07.171;

[117] Anghel Cernescu, *The role of microstructure on fatigue crack propagation*, Book chapter in "Recent Trends in Fatigue Design", Nova Science Publisher, 2015;
[118] J. Weertman, *Dislocation crack tip shielding and the Paris exponent*, Materials Science and Engineering A, 468-470: 59-63, 2007, doi: 10.1016/j.msea.2006.08.128;
[119] ASTM E 647, *Standard test method for measurement of fatigue crack growth rates*, ASTM, 100 Barr Harbor Drive, West Conshohocken, PA 19428-2959, USA;
[120] Anghel Cernescu, *The influence of crack tip shielding on fatigue crack propagation*, Frattura ed Integrita Strutturale, 41:307-313, 2017;
[121] A.A. Fadel, J.L.A. Ferreira, J.A. Araujo, L.B. Murca, A.M.D. Henriques, *Impact of mean tensile stress on aluminum steel reinforced conductors fatigue life*, Proceedings of COBEM 2011, 21st Brazilian Congress of Mechanical Engineering, October 24-28, 2011, Natal, RN, Brazil;
[122] D. Nowell, *Recent developments in the understanding of fretting fatigue*, ECF15;
[123] C.R.F. Azevedo, A.M.D. Henriques, A.R. Pulino Filho, J.L.A. Ferreira, J.A. Araujo, *Fretting fatigue in overhead conductors: Rig design and failure of a Grosbeak aluminum cable steel reinforced conductor*, Engineering Failure Analysis, 16: 136 – 151, 2009;
[124] J.C. Poffenberger, R.L. Swart, *Differential displacement and dynamic conductor strain*, IEEE Trans., 84: 281 – 289, 1965;
[125] S. Guerard, *Power line conductors, a contribution to the analysis of their dynamic behavior*, Doctoral Thesis, Faculty of Applied Sciences, University of Liege, 2011;
[126] IEEE Commitee Report, Standardization of conductor vibration measurements. IEEE Transactions on Power Apparatus and Systems, PAS – 85(1): 10 – 20, 1976;
[127] F. Levesque, *Analyse de la fatigue par petits debattements (fretting fatigue) de fils d'un conducteur electrique*, These presentee a la Faculte des etudes superieures de l'Universite Laval, Quebec, Canada, 2009;
[128] A.A. Fadel, J.L.A. Ferreira, J.A. Araujo, L.B. Murca, A.M.D. Henriques, *Impact of high mean tensile stress on aluminium steel reinforced conductors fatigue life*, Proceedings of COBEM 2011, 21st Brazilian Congress of Mechanical Engineering, October 24-28 2011, Natal, RN, Brazil;
[129] C. Dalpe, *Interaction mecanique entre conducteur electrique aerien et pince de suspension: etude sur la fatigue, la rigidite et la fip*, Memoire presente a la Faculte des etudes superieures de l'Universite Laval, Canada, 1999;

[130] R.B. Kalombo, J.A. Araujo, J.L.A. Ferreira, C.R.M. da Silva, R. Alencar, A.R. Capra, *Assesment of the fatigue failure of an All Aluminium Alloy Cable (AAAC) for a 230 kV transmission line in the Center-West of Brazil*, Engineering Failure Analysis, In Press, 2015;

[131] IEC 62568, *Method for fatigue testing of conductors for overhead lines*, 2010;

[132] Anghel Cernescu, Ion Dumitru, *Oboseala conductoarelor liniilor electrice aeriene (Fatigue of overhead power line conductors)*, Romanian Academy Publisher, ISBN 978-973-27-2783-6, 2017;

[133] Dailydka S, Lingaitis LP, Myamlin S, Prichodko V. *Modeling the interaction between railway wheel and rail*. Transport, 23(3):236–9, 2008;

[134] Bazaras Z, Sapragonas J, Vasauskas V. *Evaluation of the strength anisotropy for railway wheels*, J Vibroeng, 10(3):316–24, 2008;

[135] Boelen R, Cowin A, Donnelly R. *Ore-car coupler performance – requirements for the new century*, Proceedings on Railway Engineering, Darwin: 26.1–26.7; 2004;

[136] Boelen R, Curcio P, Cowin A, Donnelly R. *Ore-car coupler performance at BHP-Biliton iron ore*, Eng Fail Anal, 11(2):221–34, 2004;

[137] Cole C, Sun Y. *Simulated comparisons of wagon coupler systems in heavy haul trains*. Proc. IMechE, vol. 220, Part F: J. Rail and Rapid Transit;

[138] Infante V, Duarte P, Branco C. *Failure analysis of railway coupling joint*. Eng Fail Anal, 14:1175–84, 2007;

[139] Mousavi ZN, Dehghani S, Pouranvari K. *Failure analysis of automatic coupler SA-3 in railway carriages*, Eng Fail Anal, 14:903–12, 2007;

[140] Daunys M, Putnaite D, Bazaras Z. *Determination of lifetime for railway carriages automatic coupler SA-3*, Mechanika, 2(52), 2005;

[141] prEN 14033-1, *Railway applications. Track. Technical requirements for railbound construction and maintenance machines. Part I. Running of railbound machines* – UIC 826 OR – Screw couplings; 2003;

[142] SR EN 10002-1, *Metallic materials. Tensile testing. Part 1: Method of test at ambient temperature*; 2002;

[143] SR EN ISO 148-1, *Metallic materials – Charpy pendulum impact test – Part 1: Test method*, 2011;

[144] Infante V, Branco C, Brito A, Morgado T. *A failure analysis study of cast steel railway couplings used for coal transportation*. Eng Fail Anal, 10:475–89, 2003;

[145] Daunys M, Putnaite D, Bazaras Z. *Principles for modeling technological processes investigation into strength and durability of automatic coupler SA-3 in railway carriages*. Transport, 24(2):83–92, 2009;

[146] Cole C. *Longitudinal train dynamics*, Handbook of Railway Vehicle Dynamics, 239–77 [chapter 9], 2006;

[147] ANSYS Workbench version 11.

[148] Franc3D - <http://www.cfg.cornell.edu/software/franc3d_osm.htm>.

[149] Kocak M, Webster S, Janosch J, et al. *FITNET FFS – procedure – fracture, fatigue, creep, corrosion,* vol. I, 2008;

[150] NASGRO v. 4.0 – Manual - <http://www.swri.org/4org/d18/mateng/matint/nasgro/>.

[151] Stephens RI et al. *Constant and variable amplitude fatigue behavior of eight steels*. J Test Eval, 7(2):68–81, 1979.

[152] Anghel Cernescu, I. Dumitru, N. Faur, N. Branzei, R. Bogdan, *The analysis of a damaged component from the connection system of the wagons*, Engineering Failure Analysis, 29: 93-107, 2013;